

Chapter II. Designing a dimetallic hydrolytic enzyme

Introduction

While considerable progress in enhancing the catalytic properties of natural enzymes through protein redesign methods has occurred, there are few examples of successful *de novo* designed metalloenzymes (Chapter 1).¹⁻⁴ My objective is to incorporate a catalytically active mononuclear metal site into a *de novo* designed construct and, at the same time, engineer a separate and distinct structural site for stabilization (HgS₃).^{5,6} The designed metalloprotein described in this chapter represents both the first example of a *de novo* designed mononuclear metalloenzyme and of a *de novo* metalloprotein containing two different metals in two different coordination environments with distinct functions. Carbonic anhydrase (CA) was targeted for the active site because it displays high catalytic activity. Conveniently, CA's three-fold symmetric His metal-binding site fits well into the designed coiled coil scaffolds and its numerous studies, described in part in Chapter 1, provide a wealth of literature to which my results may be compared. Previous reports exist on the design of Zn(His)₃O sites into various *de novo* protein folds⁷⁻⁹ and into stable natural protein structures,^{10,11} however, neither structural elucidation of these centers nor catalytic activity were reported. Therefore, the catalytically active ZnN₃O-type site described in this chapter represents the first structurally characterized synthetic and active CA site within a "protein framework". Since this work was initially published in early 2012¹², Der *et al.* reported the design of a *de novo* ZnHis₃ site at the interface of two copies of the Rab4-binding domain of Rabenosyn, which effectively catalyzes the hydrolysis of *p*-nitrophenyl acetate (*p*NPA) and *p*-nitrophenyl phosphate (*p*NPP).¹³

As described in Chapter 1, the Pecoraro group has reported numerous studies investigating binding of metal ions such as Hg(II), Cd(II), As(III), Bi(III) and Pb(II) to three-stranded coiled coil (3SCC) scaffolds based on the **TRI** family of peptides, Ac-

G(LKALEEK)₄G-NH₂, which contain thiol substitutions for Leu residues in the interior, and have observed that addition of metal ions to these destabilized constructs confers significant stability.^{5,6,14-16} The peptides used in this study (refer to Table 2-1 for full sequences) each contain an additional His for Leu substitution in the interior of the 3SCC, which is expected to destabilize the peptide aggregate markedly. **TRIL9CL23H** contains both a His substitution in the 23rd position towards the C-terminus and a thiol substitution for preparation of a structural site in the 9th position, near the N-terminus (**TRIL23H** has only a Leu to His substitution at the 23rd position). In this chapter, I will address the design, preparation, and thorough characterization of a *de novo* coiled coil, which can not only discriminate metal complexation at different sites, but also confer structural stability from one site and support significant hydrolytic activity from the other.

Table 2-1. CoilSer (CS) and TRI peptide family sequences used in these studies.

Peptide	a	b	c	d	e	f	g
TRIL2W	Ac-G	W KALEEK	LKALEEK	LKALEEK	LKALEEK	G-NH ₂	
TRIL9C	Ac-G	LKALEEK	C KALEEK	LKALEEK	LKALEEK	G-NH ₂	
TRIL23H	Ac-G	LKALEEK	LKALEEK	LKALEEK	H KALEEK	G-NH ₂	
TRIL2WL23H	Ac-G	W KALEEK	LKALEEK	LKALEEK	H KALEEK	G-NH ₂	
TRIL9CL23H	Ac-G	LKALEEK	C KALEEK	LKALEEK	H KALEEK	G-NH ₂	
CSL12C	Ac-E	W EALEKK	LAACESK	LQALEKK	LEALEHG	-NH ₂	
CSL16C	Ac-E	W EALEKK	LAALESK	CQALEKK	LEALEHG	-NH ₂	
CSL9PenL23H	Ac-E	W EALEKK	Pen AALESK	LQALEKK	H EALEHG	-NH ₂	

N- and C-termini are capped by Ac and NH₂ groups (acetylated and amidated), respectively.

Materials and Methods

The nomenclature used to describe the metal complexes prepared in these studies is as follows. When Hg(II) is bound to the three Cys residues, this peptide will be referred to as [Hg(II)_s](**TRIL9CL23H**)₃⁻, where ‘s’ represents binding to the sulfur site. When Zn(II) is bound to the His site, there are three coordinated nitrogen atoms from protein ligands and one exogenous water or hydroxide, depending on pH. Zn_N will be used to indicate that the Zn(II) is bound at the His site and specify within parentheses the protonation state of the coordinated solvent. Under pH conditions where the solvent may

occur both as the H_2O and OH^- forms, OH_2/OH^- will be used. $[\text{Hg}(\text{II})]_s[\text{Zn}(\text{II})(\text{OH}_2)]_n(\text{TRIL9CL23H})_3^{n+}$ will then refer to a trigonally coordinated $\text{Hg}(\text{II})$ at the Cys site, and a pseudotetrahedral $\text{Zn}(\text{II})$ with three coordinated imidazoles and one water molecule.

Peptide Synthesis and Purification. Peptides were synthesized on an Applied Biosystems 433A peptide synthesizer using standard protocols¹⁷ and purified as described previously⁶ (by reverse-phase HPLC on a C18 column at a flow rate of 10 mL/min using a linear gradient varying from 0.1% TFA in water to 0.1% TFA in 9:1 $\text{CH}_3\text{CN}:\text{H}_2\text{O}$ over 25-35 minutes). Pure peptides were characterized by electrospray mass spectrometry. Peptide stock solutions were prepared in doubly distilled water that had been purged with argon to minimize oxidation of thiol-containing peptides. The concentrations for peptides containing Cys sites were determined by calculating the thiol concentration using a published assay with 5,5'-dithiobis-(2-nitrobenzoic acid) (Ellman's reagent).^{18,19} The concentrations for peptides containing Penicillamine (Pen) sites were similarly determined using a published assay with 4,4'-dipyridyl disulphide.²⁰ Concentrations of **TRIL23H** solutions were based on amino acid analysis performed by the Protein Structure Facility at the University of Michigan. Concentrations of **TRIL2WL23H** solutions were based on the tryptophan absorbance at 280 nm using $\epsilon = 5500 \text{ M}^{-1} \text{ cm}^{-1}$.

Circular Dichroism (CD) and Ultraviolet-Visible (UV-Vis) Spectroscopy. CD and UV-Vis spectra were recorded in quartz cuvettes at 25 °C on an AVIV 62DS spectrometer and Cary 100 Bio UV/Vis spectrometer, respectively. Guanidine hydrochloride (GuHCl) CD titrations were performed at pH 8.5 and 9.5 as described previously.⁵ All solutions were purged with argon prior to use in order to minimize oxidation of peptides and formation of disulfide bonds.

Hg(II)-binding titrations. $\text{Hg}(\text{II})$ into peptide titrations were performed at room temperature and monitored by UV-Vis spectroscopy in a 1-cm quartz cuvette. Aliquots of a HgCl_2 stock solution (2-2.5 mM, standardized using inductively coupled plasma-optical emission spectroscopy) were added to a 2.5 mL solution containing 30 μM peptide

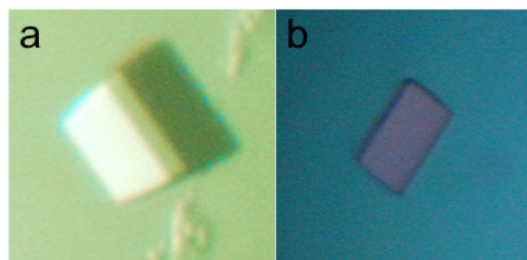


Figure 2-1. Single crystals of $[\text{Hg}(\text{II})]_s[\text{Zn}(\text{II})(\text{OH}_2/\text{OH})]_n(\text{CSL9PenL23H})_3^{n+}$. Crystal growth conditions are a) 13.8 mg/mL CSL9PenL23H, 15 mM $\text{Zn}(\text{OAc})_2$, 5 mM Tris pH 8.5, 100 mM Imidazole pH 8.5, 28% PEG-8000, 200 mM NaCl and b) 13.8 mg/mL CSL9PenL23H, 15 mM $\text{Zn}(\text{OAc})_2$, 5 mM Tris pH 8.5, 100 mM Imidazole pH 7.5, 31% PEG-8000, 200 mM NaCl.

(monomer) and 50 mM CHES (with 0.1 M Na_2SO_4) at pH 8.5 or 9.5. For all titrations, the difference spectra were obtained by subtracting the background spectrum of the peptide under identical conditions, but in the absence of metal.

Crystallization. Crystals of CSL9PenL23H (Pen = penicillamine, sequence Ac-EWEALEKK PenAALESK LQALEKK HEALEHG-NH₂, pH 8.5, Figure 2-1a) were grown by vapor diffusion at 20 °C in a hanging drop with equal volumes of peptide (13.8 mg/mL CSL9PenL23H, 15 mM $\text{Zn}(\text{OAc})_2$, 5 mM Tris pH 8.5) and precipitant (100 mM Imidazole pH 8.5, 28% PEG-8000, 200 mM NaCl), and frozen in the mother liquor for data collection. Similarly, crystals of CSL9PenL23H (pH 7.5, Figure 2-1b) were grown by vapor diffusion at 20°C in a hanging drop with equal volumes of peptide (13.8 mg/mL CSL9PenL23H, 15 mM $\text{Zn}(\text{OAc})_2$, 5 mM Tris pH 8.5) and precipitant (100 mM Imidazole pH 7.5, 31% PEG-8000, 200 mM NaCl), and frozen in the mother liquor for data collection.

Data Collection and Refinement. Data for CSL9PenL23H crystals at pH 8.5 was collected at the Advanced Photon Source in the Argonne National Laboratory on the LS-CAT Beamline 21-ID-F equipped with a Mar 225 CCD (Mar USA, Evanston, IL) and at wavelength 0.97872 Å. One hundred and eighty frames of data were collected at -180 °C with a 1° rotation and 1-s exposure rate. Data were processed and scaled with the program HKL2000.²¹ The crystals were of the space group $P2_1$ with unit cell parameters

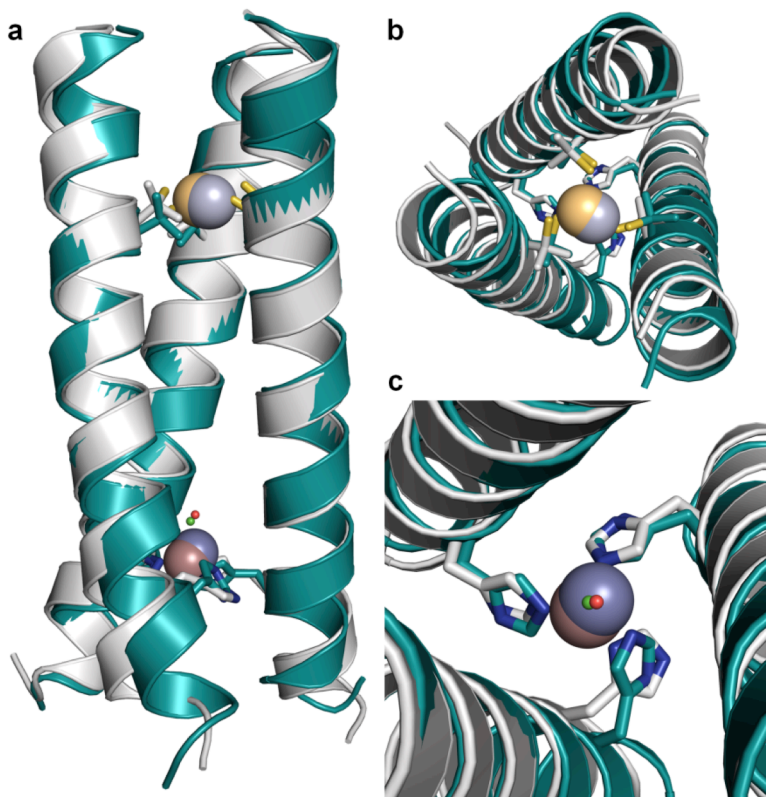


Figure 2-2. Overlay of the two different three-helix bundles in the asymmetric unit of $[\text{Hg}(\text{II})]_5[\text{Zn}(\text{II})(\text{OH}_2/\text{OH})]_N(\text{CSL9PenL23H})_3^{n+}$. The 3SCC containing chains ABC (with the trigonal $\text{Hg}(\text{II})\text{S}_3$ site and $\text{Zn}(\text{II})\text{N}_3\text{Cl}$ site) is colored grey (main chain atoms), tan (zinc atom), green (chloride), and yellow (mercury atom). The 3SCC containing chains DEF (T-shaped $\text{Hg}(\text{II})\text{S}_3$ and $\text{Zn}(\text{II})\text{N}_3\text{O}$) is colored cyan (main chain atoms). a) Overlay of the two trimers, as performed manually in PyMOL.²⁷ b) A top-down view of the three-helix bundles, focusing on the $\text{Hg}(\text{II})\text{S}_3$ sites. c) A close-up top-down view of the two $\text{Zn}(\text{II})\text{N}_3\text{X}$ sites. The overlay of the two trimers demonstrates that, even though there are slight differences in the mercury sites (T-shaped or trigonal) and zinc sites ($\text{Zn}(\text{II})\text{N}_3\text{O}$ or $\text{Zn}(\text{II})\text{N}_3\text{Cl}$), the overall fold remains essentially identical. It is also apparent that the C-terminal ends of the trimers (where the $\text{Zn}(\text{II})$ sites are) display a higher degree of “fraying”, as compared to the N-terminal ends.

$$a = 25.88 \text{ \AA}, b = 38.65 \text{ \AA}, c = 75.66 \text{ \AA}, \alpha = \gamma = 90^\circ \text{ and } \beta = 95.06^\circ.$$

The structures were solved by molecular replacement, with Phaser from the CCP4 suite^{22,23}, using as a model single α -helices based on pdb 3H5F.²⁴ The model was refined to 2.2 \AA resolution with restrained refinement in Buster 2.8.0²⁵ and built in Coot²⁶. The final structure has $R_{\text{working}} = 20.5\%$ and $R_{\text{free}} = 26.4\%$. The correlation coefficient plots calculated by Buster 2.8.0 indicate that the model structure is complete to 2.20 \AA and the data does not show anisotropy. There are two independent trimers present in the

Table 2-2. Metal-ligand bond distances and angles in [Hg(II)]_S[Zn(II)(OH₂/OH⁻)]_N(CSL9PenL23H)₃ⁿ⁺ at pH 8.5.

Zn(II)N ₃ Cl site		Hg(II)S ₃ trigonal		Zn(II)N ₃ O site		Hg(II)S ₃ t-shaped	
bond distances (Å)^a							
Zn-N _A	1.94	Hg-S _A	2.21	Zn-N _D	1.96	Hg-S _D	2.29
Zn-N _B	1.92	Hg-S _B	2.07	Zn-N _E	2.02	Hg-S _E	2.13
Zn-N _C	1.92	Hg-S _C	2.41	Zn-N _F	2.03	Hg-S _F	3.06
Zn-Cl	2.24			Zn-O	2.18		
bond angles (°)							
N _A -Zn-N _B	115.66	S _A -Hg-S _B	135.80	N _D -Zn-N _E	101.77	S _D -Hg-S _E	160.11
N _B -Zn-N _C	125.14	S _B -Hg-S _C	115.65	N _E -Zn-N _F	114.48	S _E -Hg-S _F	90.55
N _A -Zn-N _C	95.52	S _A -Hg-S _C	108.26	N _D -Zn-N _F	93.32	S _D -Hg-S _F	106.52
N _A -Zn-Cl	96.00			N _D -Zn-O	129.01		
N _B -Zn-Cl	119.51			N _E -Zn-O	111.34		
N _C -Zn-Cl	98.98			N _F -Zn-O	106.07		

a. Subscripts represent which helix chain the ligand belongs to (the ligands are ‘N’ for the nitrogen of His and ‘S’ for the sulfur of Pen).

asymmetric unit (ASU) and fraying of the C-termini is observed, resulting in larger B-factors in this region. An overlay of the two trimers in the ASU demonstrates that they have similar overall folds and that the Zn(II) sites have the same geometry (Figure 2-2). To deduce the configuration of the metal sites, the atoms of these sites were initially refined without imposing geometric restraints. Once their positions were determined,

Table 2-3. Data collection statistics at pH 8.5.

Data collection	
Space group	<i>P</i> 2 ₁
Cell dimensions	
<i>a</i> , <i>b</i> , <i>c</i> (Å)	25.88, 38.65, 75.66
α, β, γ (°)	90, 95.06, 90
Wavelength (Å)	0.97872
Resolution (Å) ^a	2.2(2.24-2.20)
<i>R</i> _{sym} (%) ^b	5.8(32.1)
< <i>I</i> /σ <i>I</i> > ^c	> 20(2)
Completeness (%) ^d	98.3(97.1)
Redundancy	3.0(2.9)
Beamline	LS-CAT 21-ID-F

a. Statistics for highest resolution bin of reflections in parentheses.

b. $R_{\text{sym}} = \sum_h \sum_j |I_{hj} - \langle I_h \rangle| / \sum_h \sum_j I_{hj}$, where I_{hj} is the intensity of observation *j* of reflection *h* and $\langle I_h \rangle$ is the mean intensity for multiply recorded reflections.

c. Intensity signal-to-noise ratio.

d. Completeness of the unique diffraction data.

Table 2-4. Refinement statistics at pH 8.5.

Refinement	
Resolution (Å)	2.20(26.98-2.20)
No. reflections	7625
R_{factor} (%) ^a	20.5
R_{free} (%) ^b	26.4
No. atoms	
Protein ^c	1359
Ligand/ion	13
Water	66
RSCC/RSR for metal sites ^d	
Zn(II) in ZnN ₃ Cl site	0.969/0.046
Cl ⁻ in ZnN ₃ Cl	0.952/0.122
Zn(II) in ZnN ₃ O	0.926/0.104
Hg(II) in trigonal site	0.851/0.085
Hg(II) in T-shaped site	0.955/0.087
Occupancies of metal sites/B-factors ^e	
Zn(II) in ZnN ₃ Cl site	1.0/41.77
Zn(II) in ZnN ₃ O site	1.0/76.96
Hg(II) in trigonal site	0.55/54.73
Hg(II) in T-shaped	0.60/46.36
B-factors ^e	
Protein	51.4
Ligand/ion	55.1
Water	51.1
R.m.s. deviations ^f	
Bond lengths (Å)	0.014
Bond angles (°)	1.73

a. $R_{\text{factor}} = \sum_h | |F_o| - |F_c| | / \sum_h |F_o|$, where F_o and F_c are the observed and calculated structure factor amplitudes for reflection h .

b. R_{free} is calculated against a 10% random sampling of the reflections that were removed before structure refinement.

c. Total number of protein atoms refined in the ASU.

d. Real-space correlation coefficient (RSCC) and real-space R values (RSR) as obtained from the Uppsala Electron Density Server.⁸³

e. B factors are higher than what is typically expected for a refined crystal structure. This is likely due to the fraying of the C-termini. Due to the fraying, three very similar molecular replacement solutions for this structure were seen, the clearest of which was used for refinement of the structure presented here. Notably, the core residues including the metal positions were virtually identical in all solutions.

f. Root mean square deviation of bond lengths and bond angles.

geometric parameters were used to restrain the bond lengths and angles of the metal-coordinating atoms (refer to Table 2-2 for distances and angles of each metal site). Since the B-factors on several of the metals were found to be higher than their coordinating atoms, the B-factors for these metals were set to the Wilson B for a round of occupancy

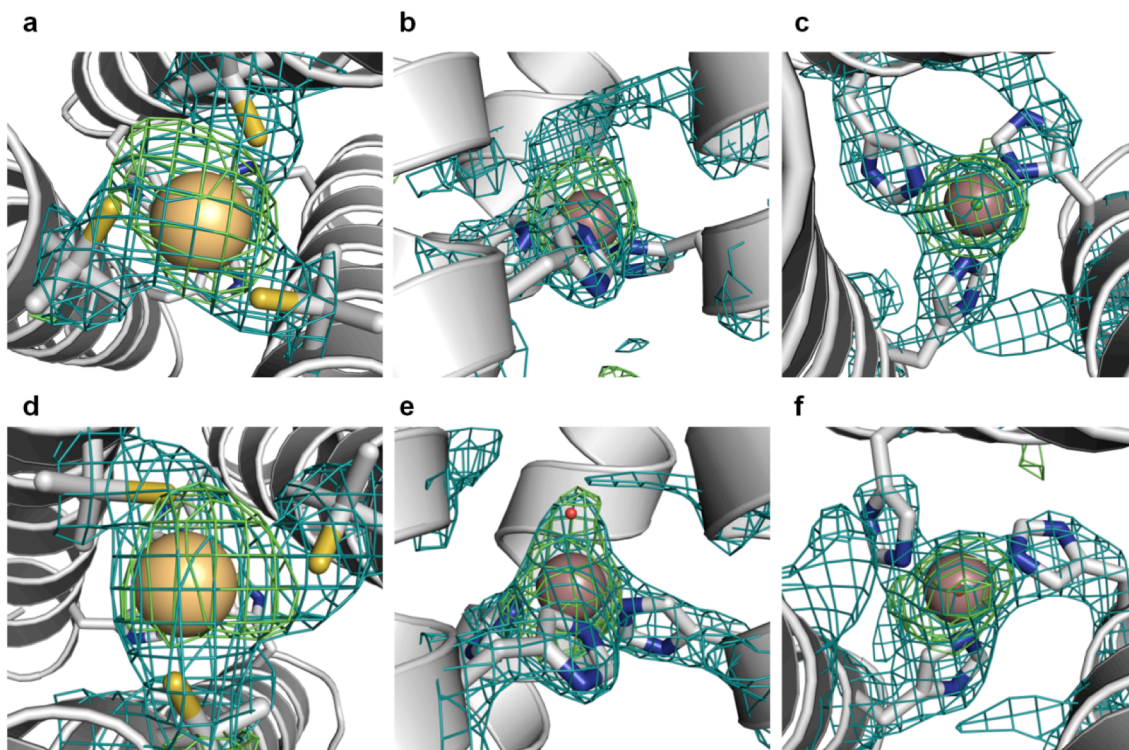


Figure 2-3. Omit maps for the metal sites in $[\text{Hg(II)}]_s[\text{Zn(II)(OH}_2/\text{OH)}]_N(\text{CSL9PenL23H})_3^{n+}$. Shown are the main chain atoms represented as helical ribbons (light grey) and the Pen and His side chains in stick form (sulfur = yellow, nitrogen = blue, oxygen = red, chloride = green). The mercury atom is colored light orange and zinc is colored tan. Electron density maps were generated through refinement with the metal occupancies set to zero. $2F_o - F_c$ electron density is shown for each metal site contoured at 1.5σ and colored blue. $F_o - F_c$ electron density is shown for each metal contoured at 3σ and colored green. a) Top-down view of the trigonal Hg(II)S_3 site (metal occupancy = 0.55), b) side-on view of the $\text{Zn(II)N}_3\text{Cl}$ site (metal occupancy = 1.0), c) top-down view of the $\text{Zn(II)N}_3\text{Cl}$ site, d) top-down view of the T-shaped Hg(II)S_3 site (metal occupancy = 0.60), e) side-on view of the $\text{Zn(II)N}_3\text{O}$ site (metal occupancy = 1.0), f) top-down view of the $\text{Zn(II)N}_3\text{O}$ site. No evidence of alternate ligand-metal geometries or metal positions is observed.

refinement. The refined occupancies and accompanying B-values are shown in Table 2-4. Omit maps of the metal sites confirmed a single position for each metal (i.e., no alternate positions for the metals were apparent in the density) (Figure 2-3). Metal difference density for each metal as observed at the start of refinement is shown in Figure 2-4. Data collection and refinement statistics are given in Tables 2-3-2-4. The atomic coordinates and structure factors have been deposited in the Protein Data Bank with the ID code

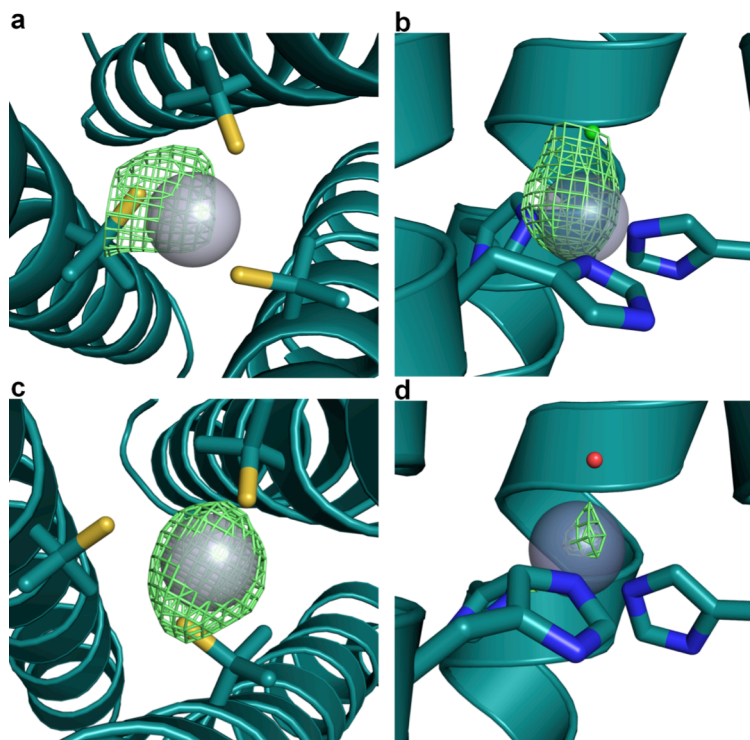


Figure 2-4. Metal difference density as observed at the start of refinement. Shown are the metal difference electron densities ($F_o - F_c$) contoured at 3.0σ for each site in each trimer in the asymmetric unit. a) Trigonal Hg(II) S_3 site, b) Zn(II) N_3Cl site, c) T-shaped Hg(II) site, d) Zn(II) N_3O site. These confirm that the metal positions at the end of refinement are the same as they were at the start.

Table 2-5. Metal-ligand bond distances and angles in $[Hg(II)]_3[Zn(II)(OH_2/OH^-)]_3(CSL9PenL23H)_3^{n+}$ at pH 7.5.

Zn(II) N_3Cl site	Hg(II) S_3 ABC		Zn(II) N_3Cl site	Hg(II) S_3 DEF			
bond distances (\AA)^a							
Zn- N_A	1.92	Hg- S_A	2.15	Zn- N_D	2.08	Hg- S_D	1.49
Zn- N_B	1.91	Hg- S_B	1.89	Zn- N_E	1.93	Hg- S_E	1.93
Zn- N_C	1.92	Hg- S_C	2.89	Zn- N_F	2.11	Hg- S_F	2.93
Zn-Cl	2.30	Hg ^{ex} -S	2.51	Zn-Cl	2.21	Hg ^{ex} -S	2.55
bond angles ($^\circ$)							
N_A -Zn- N_B	110.61	S_A -Hg- S_B	156.99	N_D -Zn- N_E	118.21	S_D -Hg- S_E	128.38
N_B -Zn- N_C	112.76	S_B -Hg- S_C	97.21	N_E -Zn- N_F	102.99	S_E -Hg- S_F	105.40
N_A -Zn- N_C	100.07	S_A -Hg- S_C	105.78	N_D -Zn- N_F	83.61	S_D -Hg- S_F	126.20
N_A -Zn-Cl	109.22			N_D -Zn-Cl	128.46		
N_B -Zn-Cl	109.98			N_E -Zn-Cl	108.87		
N_C -Zn-Cl	113.77			N_F -Zn-Cl	105.86		

a. Subscripts represent which helix chain the ligand belongs to (the ligands are ‘N’ for the nitrogen of His and ‘S’ for the sulfur of Pen).

3PBJ. Figures were generated in PyMOL.²⁷

Data for CSL9PenL23H crystals at pH 7.5 was collected at the Advanced Photon Source in the Argonne National Laboratory on the LS-CAT Beamline 21-ID-D equipped with a Mar 300 CCD (Mar USA, Evanston, IL) and at wavelength 1.07817 Å. Three hundred and sixty frames of data were collected at -180 °C with a 1° rotation and 3-s

Table 2-6. Data collection statistics at pH 7.5.

Data collection	
Space group	$P2_1$
Cell dimensions	
<i>a</i> , <i>b</i> , <i>c</i> (Å)	27.12, 41.38, 75.36
α , β , γ (°)	90, 91.89, 90
Wavelength (Å)	1.07817
Resolution (Å) ^a	2.2(2.24-2.20)
R_{sym} (%) ^b	
$\langle I/\sigma \rangle$ ^c	
Completeness (%) ^d	
Redundancy	
Beamline	LS-CAT 21-ID-D

a. Statistics for highest resolution bin of reflections in parentheses.

b. $R_{\text{sym}} = \sum_h \sum_j |I_{hj} - \langle I_h \rangle| / \sum_h \sum_j I_{hj}$, where I_{hj} is the intensity of observation *j* of reflection *h* and $\langle I_h \rangle$ is the mean intensity for multiply recorded reflections.

c. Intensity signal-to-noise ratio.

d. Completeness of the unique diffraction data.

exposure. Data were processed and scaled with the program HKL-2000.²¹ The crystals were of the space group $P2_1$ with unit cell parameters $a = 27.12$ $b = 41.38$, $c = 75.36$, $\alpha = \gamma = 90^\circ$ and $\beta = 91.89^\circ$.

The structures were solved by molecular replacement, with Phaser from the CCP4 suite^{22,23}, using as a model a single 3SCC based on pdb 3PBJ.¹² The model was refined with restrained refinement in Buster 2.8.0²⁵ and built in Coot²⁶ using the $2F_o - F_c$ and $F_o - F_c$ electron density maps generated in Buster 2.8.0. The refinement (although currently incomplete) to 2.20 Å resulted in $R_{\text{working}} = 20.2\%$ and $R_{\text{free}} = 28.2\%$. There are two independent trimers present in the ASU and fraying of the termini, especially at the C-termini (like for the pH 8.5 structure), is observed. Current metal-ligand bond distances and angles are given in Table 2-5. Data collection and currently available refinement statistics are given in Tables 2-6-2-7. The atomic coordinates and structure factors will be deposited in the Protein Data Bank once refinement is complete and this work is published. Figures were generated in PyMOL.²⁷

Table 2-7. Refinement statistics at pH 7.5.

Refinement	
Resolution (Å)	2.20(27.85-2.20)
No. reflections	6045
R_{factor} (%) ^a	20.2
R_{free} (%) ^b	28.2
No. atoms	
Protein ^c	1341
Ligand/ion	13
Water	40
Occupancies of metal sites/B-factors ^d	
Zn(II) in ZnN ₃ Cl site (ABC trimer)	1.0/69.85
Zn(II) in ZnN ₃ O site (DEF trimer)	1.0/69.48
Hg(II) interior ABC trimer	0.53/62.99
Hg(II) interior DEF trimer	0.46/55.78
Hg(II) exterior ABC trimer	0.65/75
Hg(II) exterior DEF trimer	0.51/60
R.m.s. deviations ^e	
Bond lengths (Å)	0.010
Bond angles (°)	1.32

a. $R_{\text{factor}} = \sum_h |F_o| - |F_c| / \sum_h |F_o|$, where F_o and F_c are the observed and calculated structure factor amplitudes for reflection h .

b. R_{free} is calculated against a 10% random sampling of the reflections that were removed before structure refinement.

c. Total number of protein atoms refined in the ASU.

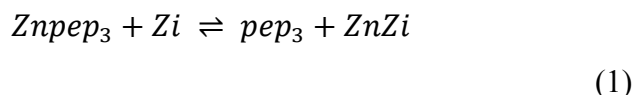
d. B factors are higher than what is typically expected for a refined crystal structure. This is likely due to the fraying of the C-termini. Due to the fraying, three very similar molecular replacement solutions for this structure were seen, the clearest of which was used for refinement of the structure presented here. Notably, the core residues including the metal positions were virtually identical in all solutions.

e. Root mean square deviation of bond lengths and bond angles.

Competitive Zn(II)-Binding Titrations. The apparent binding constants were determined by competition assay with the colorimetric Zn(II) chelator, Zincon (2-carboxy-2'-hydroxy-5'-(sulfoformazyl)benzene).^{28,29} Zn(II) forms a 1:1 complex with Zincon (Zi) with a distinct absorption band at 620 nm ($\epsilon \sim 16000 \text{ M}^{-1} \text{ cm}^{-1}$) at pH 7.5 and apparent dissociation constant ($K_{\text{d,app}}$) of $2.80 \times 10^{-6} \text{ M}$ (consistent with the range of reported values).^{28,30-34} These parameters were evaluated for each pH and each buffer used in these experiments (pH 7.5 in 50 mM HEPES, 0.1 M Na₂SO₄ and pH 9.0 in 50 mM CHES, 0.1 M Na₂SO₄) by titrating Zn(II) (stock solutions were standardized using inductively coupled plasma-optical emission spectroscopy) into a solution of 10 μM Zi. For pH 9.0, $\epsilon_{620} \sim 27500 \text{ M}^{-1} \text{ cm}^{-1}$ and $K_{\text{d,app}} = 5 \times 10^{-8} \text{ M}$ (a 5 cm pathlength cell was used

for the calibration titration at this pH). For experiments involving peptide, an excess of Zi over ZnSO₄ (10 μM Zi and 5 μM Zn(II) to ensure most Zn(II) is bound to ligand) was used as the starting point of the titration. Analogously, Zn(II) was bound to an excess of peptide (20 μM pep₃ and 10 μM Zn(II)) for the reverse titration. Both approaches should give similar apparent binding constants for Znpep₃, indicating equilibrium had been reached.

The binding equilibrium for this competition experiment can be expressed by eq 1.



The apparent dissociation constant of Znpep₃ can be calculated using eq 2.

$$\frac{K_{d,\text{znpep}_3}}{K_{d,\text{znzi}}} = \frac{([\text{ZnZi}][\text{pep}_3])}{([\text{Znpep}_3][\text{Zi}])} \quad (2)$$

For the forward titration, where a solution of Zi is titrated into Znpep₃, the absorption band at 620 nm is due to the ZnZi complex, and increases as Zi is added to Znpep₃, reflecting transfer of Zn(II) from pep₃ to Zi and therefore yielding [ZnZi] and [Znpep₃] for eq 2. [Znpep₃] can be defined as the total amount of Zn(II) present ([Zn]_T) minus the Zn(II)-bound fraction ([ZnZi]), under the conditions of this experiment. The amount of unbound peptide can then be defined as the total peptide minus the Zn(II)-bound fraction, [pep₃] = [pep₃]_T - [Znpep₃] = [pep₃]_T - ([Zn]_T - [ZnZi]). The amount of free Zi is then related to the total amount of Zi minus the Zn(II)-bound fraction, [Zi] = [Zi]_T - [ZnZi]. Substituting all of the above into eq 2 yields a quadratic expression, eq 3, which can be solved for [ZnZi]. Since this quantity is directly related to the absorbance at 620 nm by the Beer-Lambert law, the real solution to eq 3 can be inserted into eq 4 to give an equation which can be fitted in Prism 5 (GraphPad Software)³⁵ to yield the dissociation constant for Znpep₃.

$$\begin{aligned} & \left(\frac{K_{d,\text{znpep}_3}}{K_{d,\text{znzi}}} - 1 \right) [\text{ZnZi}]^2 \\ & + \left(-\frac{K_{d,\text{znpep}_3}}{K_{d,\text{znzi}}} x - \frac{K_{d,\text{znpep}_3}}{K_{d,\text{znzi}}} [\text{Zn}]_T - [\text{pep}_3]_T + [\text{Zn}]_T \right) [\text{ZnZi}] + \frac{K_{d,\text{znpep}_3}}{K_{d,\text{znzi}}} [\text{Zn}]_T x \\ & = 0 \end{aligned}$$

(3)

$$A_{620} = y = \varepsilon * b * [ZnZi]$$

(4)

An analogous approach was used for the reverse titration, in which pep₃ is added to ZnZi.

Esterase Activity Assays. The esterase activities of [Hg(II)_S][Zn(II)(OH₂/OH)]_N(TRIL9CL23H)₃ⁿ⁺ were determined spectrophotometrically with *p*NPA as substrate (0.03-1.2 mM) at 25 °C. Measurements were made at 348 nm, the isosbestic point for *p*-nitrophenol and *p*-nitrophenolate ion ($\varepsilon = 5000 \text{ M}^{-1} \text{ cm}^{-1}$).³⁶ The observed activities were corrected for background ester hydrolysis in the absence of enzyme. A control containing ZnSO₄ without enzyme did not exhibit any activity above that of the blank. Activities were determined over the following pH range and conditions: pH 7.5-8.0, 50 mM HEPES, 0.1 M Na₂SO₄; pH 8.5-9.5, 50 mM CHES, 0.1 M Na₂SO₄. The substrate solution was prepared fresh each day beginning with a 0.1 M solution of *p*NPA in acetone and slowly adding doubly distilled H₂O (ddH₂O) with vigorous stirring to dilute to 3 mM *p*NPA. For measuring esterase activity: in a 1 mm pathlength spectrophotometric cuvette, buffer (50 mM), ddH₂O, and *p*NPA were mixed and the absorbance recorded (after baseline correction with solution containing only buffer and ddH₂O). Then, after addition of peptide (10 μM ZnSO₄ and 50 μM [Hg(II)_S](TRIL9CL23H)₃⁻, to ensure all Zn(II) was bound to the peptide), the increase in absorption at 348 nm was measured at least every 25 seconds for a minimum of 10 minutes, and longer for the slower rates at lower pH values. In addition to background correction for spontaneous hydrolysis in each buffer solution, the rates were corrected for background peptide activity (40 μM [Hg(II)_S](TRIL9CL23H)₃⁻, added to the control cuvette at the same time the catalyst, peptide-zinc complex, was added), as imidazole is known to modestly catalyze this reaction. Initial rates for each substrate concentration ([S], repeated at least twice per concentration per pH) were determined from linear fits of plots of product formation versus time. These slopes (or initial rates, *v*) were then plotted as a function of [S] and their reciprocals taken to give double reciprocal or Lineweaver-Burke plots (fitted in OriginPro 8), from which V_{max}/K_M , V_{max} , and K_M values and their

errors were determined based on the equation $1/v = 1/V_{\max} + K_M/V_{\max}[S]$. k_{cat} and k_{cat}/K_M values were determined based on the concentration of $[\text{Hg(II)}]_S[\text{Zn(II)(OH}_2/\text{OH}^-)]_N(\text{TRIL9CL23H})_3^{n+}$ catalyst, 10 μM . Similar values are obtained by performing a non-linear fit of the initial rates to the Michaelis-Menten equation in Prism 5 (GraphPad Software).³⁵ k_{cat} and K_M values have rather large errors due to the solubility limitations of *p*NPA, which precluded my ability to test substrate concentrations at or above the K_M values (the highest achievable under these conditions is 1.2 mM). $\text{p}K_a$'s were determined from fits of k_{cat}/K_M and k_{cat} vs pH in OriginPro 8 and the reported errors for $[\text{Hg(II)}]_S[\text{Zn(II)(OH}_2/\text{OH}^-)]_N(\text{TRIL9CL23H})_3^{n+}$ are based on these fits. The same procedure was used for measuring the activity of $[\text{Zn(II)(OH}_2/\text{OH}^-)]_N(\text{TRIL23H})_3^{n+}$. For $[\text{Zn(II)(OH}_2/\text{OH}^-)]_N(\text{TRIL2WL23H})_3^{n+}$, initial rates were obtained with a metal-peptide solution of 20 μM Znpep₃ with 4x excess ZnSO₄ present (the same values can be obtained when using excess peptide, but using excess ZnSO₄ is more cost-effective). All values shown for this metal-peptide complex were obtained by performing non-linear fits of the initial rates to the Michaelis-Menten equation in Prism 5 (GraphPad Software).³⁵ For initial inhibition studies, the above procedure was also followed, with the exception that varying concentrations of potassium acetate (KOAc; 0, 0.2, 0.5, 0.7 M) were included in the initial buffer solution before addition of substrate and then enzyme. For more extensive inhibition studies, see the next section. The catalytic efficiencies of several controls were also determined. For $[\text{Hg(II)}]_S(\text{TRIL9CL23H})_3^-$ and apo- $(\text{TRIL9CL23H})_3^{n-}$ (pH 9.0), 40 μM of peptide complex was used and run in parallel with spontaneous *p*NPA hydrolysis as the control and the rates corrected for this. The approach taken for $[\text{Hg(II)}]_S[\text{Zn(II)(OH}_2/\text{OH}^-)]_N(\text{CSL9PenL23H})_3^{n+}$ (pH 9.5) was identical to that used for $[\text{Hg(II)}]_S[\text{Zn(II)(OH}_2/\text{OH}^-)]_N(\text{TRIL9CL23H})_3^{n+}$. Finally, the activity of $[\text{Hg(II)}]_S(\text{TRIL9C})_3^- + \text{Zn(II)}$ (50 μM total, 10 μM ZnSO₄) was measured as an unbound Zn(II) control at pH 9.0 and compared to that of $[\text{Hg(II)}]_S(\text{TRIL9C})_3^-$ (40 μM), both of which were corrected for spontaneous hydrolysis. Catalytic efficiencies (k_{cat}/K_M) of all of the above controls could be successfully determined both utilizing Lineweaver-Burke plots as described above and non-linear fits of the initial rates to the Michaelis-Menten

equation in Prism 5 (GraphPad Software).³⁵ However, as considerable errors were observed for individual k_{cat} and K_M values, these are not reported.

Acetate Inhibition Assays. Inhibition experiments were performed under the same buffer conditions and with the same general procedure as described above for $[\text{Zn}(\text{II})(\text{OH}_2/\text{OH})]_N(\text{TRIL2WL23H})_3^{n+}$ (excess Zn(II) conditions). KOAc stock solutions (~7-10 M) were prepared by dissolving KOAc in a small amount of water, adjusting pH to 8.5 with glacial acetic acid (and vigorous stirring), followed by dilution to the final volume with ddH₂O. The acetate concentration is determined by combining the concentration from the amount of solid and from the acetic acid added. For running the assays, buffer, ddH₂O, KOAc, and enzyme were mixed together, then *p*NPA added and the absorbance monitored as above. Metal-peptide solutions were 20 μM Znpep₃ with 4x excess ZnSO₄ present. Controls contained all components except peptide and the difference between initial rates was taken. Initial rates were plotted and fitted as described above (non-linear fits to the Michaelis-Menten equation in Prism 5 (GraphPad Software)³⁵). For each peptide, at least three different concentrations of KOAc were tested, and plots of initial rates vs [*p*NPA] were prepared and fitted to competitive, non-competitive, and mixed inhibition equations in Prism 5 (GraphPad Software)³⁵. The individual kinetic parameters for each concentration of acetate were examined in order to estimate the applicable inhibition model (all peptides had increasing K_M and decreasing k_{cat} values as a function of increasing substrate concentration supporting a competitive inhibition model).³⁷ Lineweaver-Burke plots, in addition to examination of the α value from a mixed model fit for each complex, were also used to conclude that the inhibition observed was competitive for all peptide complexes containing a ZnHis₃ site (Lineweaver-Burke plots intersect on the y-axis and $\alpha > 1$). The α value determines the degree to which inhibitor binding changes the enzyme's affinity for substrate. If $\alpha > 1$ (and especially if it is very large), then inhibitor binding prevents substrate binding and the mixed model represents competitive inhibition.³⁷

Results

Characterization of Structural and Catalytic Sites.

a) Hg(II) Binding. The binding of Hg(II) to TRIL9CL23H was measured by UV-Vis spectroscopy. Aliquots of HgCl₂ were added to a solution of 10 μM (TRIL9CL23H)₃ⁿ⁻ in 50 mM CHES buffer (with 0.1 M Na₂SO₄) at pH 8.5. As the HgS₃ complex was formed, an increase in absorbance at 247 nm (maximum at one equivalent per trimer) with shoulders at 265 and 295 nm was observed (Figure 2-5). Previous work in the group has demonstrated that this spectrum is characteristic of a three-coordinate HgS₃ complex.^{38,39} In the presence of excess Hg(II), the spectrum is converted to that typical of a HgS₂ site in a 2SCC. Along with ¹⁹⁹Hg NMR data collected by Dr. Anna F. A. Peacock, a previous postdoctoral researcher in the group, this confirms Hg(II) binding exclusively to the Cys₃ site.

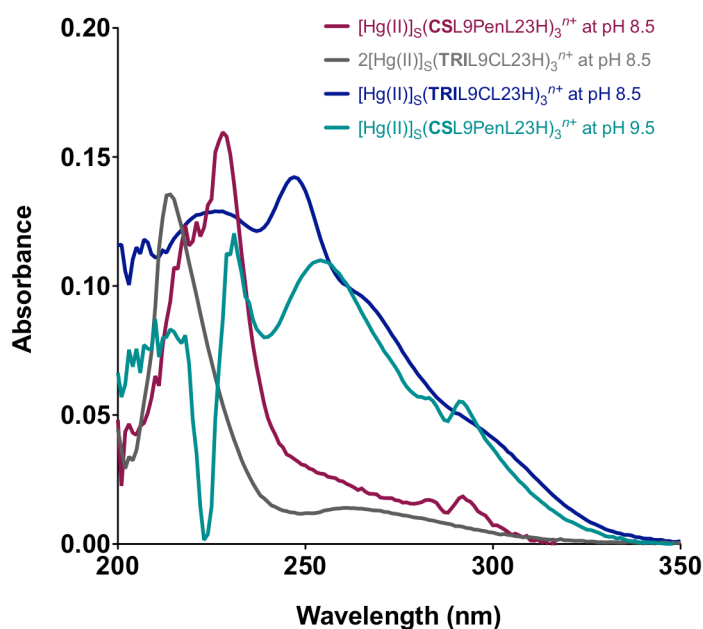


Figure 2-5. UV absorbance difference spectra for HgS₃ centers in TRIL9CL23H and CSL9PenL23H. Magenta: 10 μM HgCl₂ and 10 μM (CSL9PenL23H)₃ⁿ⁻ at pH 8.5 in 50 mM CHES, 0.1 M Na₂SO₄. Grey: 20 μM HgCl₂ and 10 μM (TRIL9CL23H)₃ⁿ⁻ at pH 8.5 in 50 mM CHES, 0.1 M Na₂SO₄. Blue: 10 μM HgCl₂ and 10 μM (TRIL9CL23H)₃ⁿ⁻ at pH 8.5 in 50 mM CHES, 0.1 M Na₂SO₄. Teal: 10 μM HgCl₂ and 10 μM (CSL9PenL23H)₃ⁿ⁻ at pH 9.5 in 50 mM CHES, 0.1 M Na₂SO₄. The negative absorbance present at ~220 nm is likely due to changes in the folding of the peptide upon addition of Hg(II), since the background apo-peptide spectra are subtracted from the metal-bound spectra.

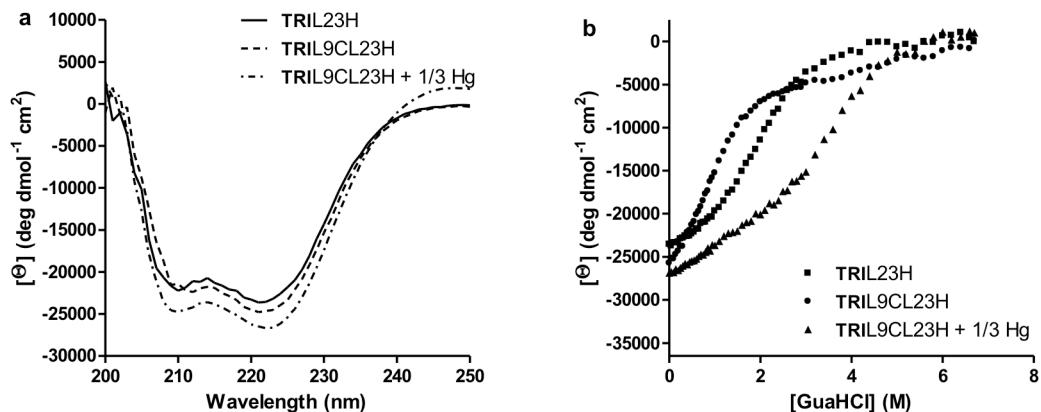


Figure 2-6. Folding of TRIL23H, TRIL9CL23H, and TRIL9CL23H + 1/3 Hg(II) as monitored by CD. a) CD spectra of TRIL23H (—), TRIL9CL23H (---), and TRIL9CL23H + 1/3 Hg(II) (· · ·) at pH 8.5 and ambient temperature. b) GuHCl denaturation titrations represented by the molar ellipticity values $[\Theta]$ at 222 nm versus denaturant concentration for TRIL23H (■), TRIL9CL23H (●), and TRIL9CL23H + 1/3 Hg(II) (▲), respectively. Addition of Hg(II) to TRIL23H does not result in additional stabilization (not shown). I have refrained from giving a quantitative determination of free energy values because the denaturation curve for TRIL9CL23H does not level off at zero concentration of denaturant. For the TRIL9CL23H + 1/3 Hg(II) curve, competition of chloride with the sulfur ligands may lead to a decrease in stability so that what is observed is a minimum value for Hg(II) folding and therefore, the system is too complicated to fit to a simple two-state folding unfolding model. Nonetheless, the midpoint has shifted dramatically, demonstrating the stability enforced by Hg(II) binding.

The binding of Hg(II) to CSL9PenL23H was also measured using UV-Vis spectroscopy. Aliquots of HgCl₂ were added to a solution of 10 μM (CSL9PenL23H)₃⁷⁻ in 50 mM CHES buffer (with 0.1 M Na₂SO₄) at pH 8.5. At this pH, an increase in absorbance at 230 nm (maximum at one equivalent per trimer) was observed with minor features at lower energies. This spectrum more closely resembles that of a HgCys₂ complex than HgCys₃. However, at pH 9.5, an increase in absorbance at 254 nm with shoulders at 283 nm and 292 nm was observed, and more closely resembles that of a HgCys₃ complex. The shift in energies is likely due to differences in the electronic environment resulting from the Pen ligand. The increase in pH required to observe the HgS₃ complex likely reflects a higher pK_a for metal binding (according to preliminary pH titration data, the pK_a is > 9, whereas for Hg(II) binding to the Cys₃ site, it is ~7.1).

b) Circular Dichroism (CD) of Apo- and Metal-Bound Peptides. To measure whether the presence of this HgS_3 site confers thermodynamic stability on the 3SCC, GuHCl denaturation titrations were monitored using CD spectroscopy. Specifically, the folding of **TRIL9CL23H** in the presence and absence of Hg(II) was measured and also compared to the peptide **TRIL23H**, which lacked the structural site substitution altogether. The peptide region of the CD spectrum yields characteristic coiled coil peaks

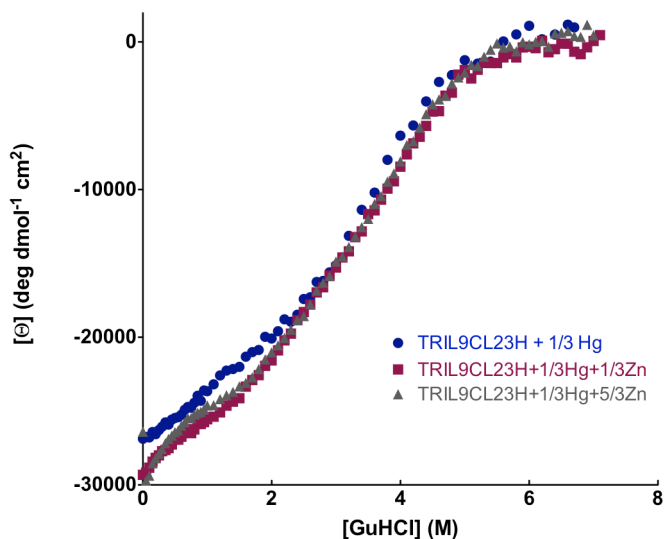


Figure 2-7. Comparison of the unfolding of $\text{TRIL9CL23H} + 1/3 \text{Hg(II)}$ in the presence of 0, 1, and 5 equivalents of Zn(II) .¹² GuHCl denaturation titrations at pH 8.5 represented by the molar ellipticity values $[\Theta]$ at 222 nm vs denaturant concentration for $\text{TRIL9CL23H} + 1/3 \text{Hg(II)}$ (\bullet)¹², $\text{TRIL9CL23H} + 1/3 \text{Hg(II)} + 1/3 \text{Zn(II)}$ (\blacksquare), and $\text{TRIL9CL23H} + 1/3 \text{Hg(II)} + 5/3 \text{Zn(II)}$ (\blacktriangle). There is no shift in the midpoint of unfolding in the presence of Zn(II) .

with negative minima at 208 and 222 nm. By monitoring this region, molar ellipticity values $[\Theta]$ obtained at 222 nm and pH 8.5 of $\sim -24100 \text{ deg dmol}^{-1} \text{ cm}^2$ for $(\text{TRIL23H})_3$ and $\sim -25700 \text{ deg dmol}^{-1} \text{ cm}^2$ for $(\text{TRIL9CL23H})_3^{n-}$ were determined. The molar ellipticity of $[\text{Hg(II)}_s](\text{TRIL9CL23H})_3^-$ is $\sim -26800 \text{ deg dmol}^{-1} \text{ cm}^2$. This data cannot be quantitatively fit to a two-state model (Figure 2-6), so the midpoint for unfolding of complexes is used to compare the relative stabilities of the coiled coils. The presence of one and five equivalents ZnSO_4 does not alter the unfolding of $[\text{Hg(II)}_s](\text{TRIL9CL23H})_3^-$ (Figure 2-7).

GuHCl denaturation titrations were also performed for the crystallographic analog sequence CSL9PenL23H in the presence and absence of Hg(II) at pH 8.5 and 9.5. At pH 8.5, the molar ellipticity for apo-(CSL9PenL23H)₃ⁿ⁻ is ~ -19800 deg dmol⁻¹ cm² and for the Hg(II)-bound version is ~ -25800 deg dmol⁻¹ cm². At pH 9.5, these values drop to ~ -9100 and ~ -17300 deg dmol⁻¹ cm², as expected for this less stable sequence (compared to **TRI**). Comparison of the midpoint of unfolding for these complexes at pH 8.5 (Figure 2-8) and 9.5 (not shown) indicates an increase in thermodynamic stability conferred by the Hg(II) site (although it is not as pronounced as that for **TRIL9CL23H**).

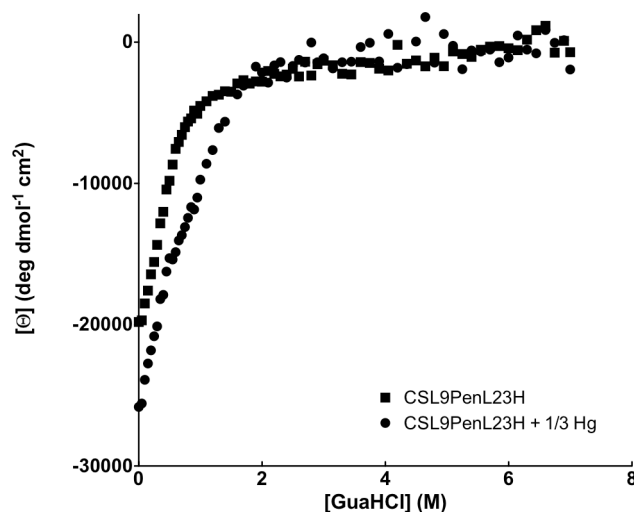


Figure 2-8. Folding of CSL9PenL23H and CSL9PenL23H + 1/3 Hg(II) as monitored by CD. GuHCl denaturation titrations represented by [Θ] at 222 nm vs denaturant concentration for CSL9PenL23H (■) and CSL9PenL23H + 1/3 Hg(II) (●).

c) Crystallographic Characterization at pH 8.5. The X-ray crystal structure of [Hg(II)]_S[Zn(II)(OH₂/OH⁻)]_N(CSL9PenL23H)₃ⁿ⁺ was solved to 2.2 Å resolution. Crystals in space group *P2*₁ were obtained at pH 8.5 and the structure was solved using molecular replacement. The resulting model, [Hg(II)]_S[Zn(II)(OH₂/OH⁻)]_N(CSL9PenL23H)₃ⁿ⁺ (pdb 3PBJ), contains two independent well-folded, parallel 3SCCs in the ASU (Figures 2-9-2-10). One contains Hg(II) bound to the sulfurs of Pen in a trigonal planar structure (Figure 2-10b) with Hg(II)-S distances 2.21, 2.07, 2.41 Å, and four-coordinate zinc bound to three His ligands and a chloride ion. The other 3SCC contains a T-shaped Hg(II) ion (Hg(II)-S distances 2.29, 2.13, 3.06 Å) (Figure 2-9b) and a four-coordinate Zn(II) ion

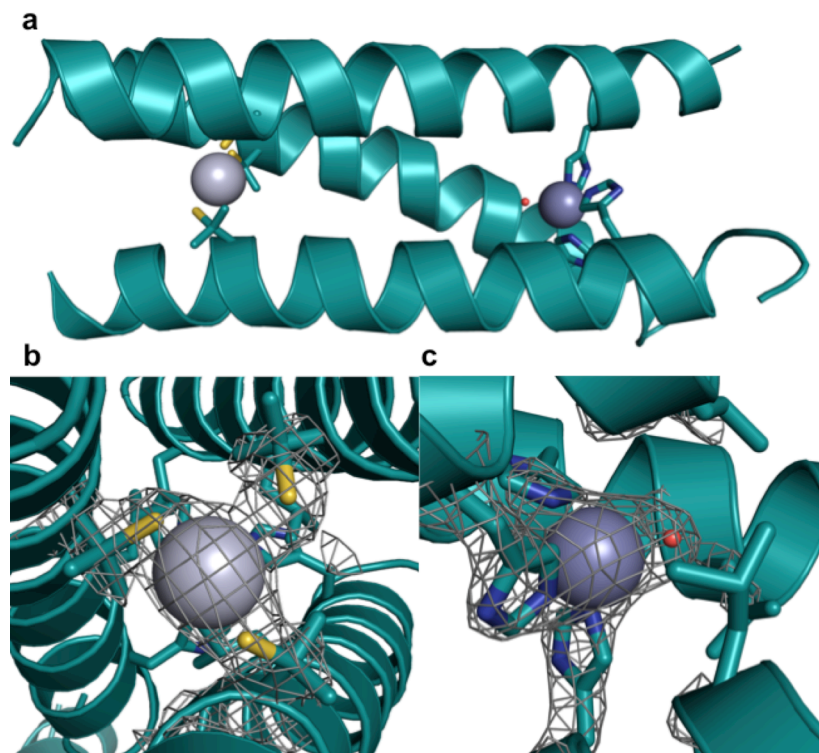


Figure 2-9. Ribbon diagrams of the $[\text{Hg(II)}]_s[\text{Zn(II)(OH}_2/\text{OH}^-)]_N(\text{CSL9PenL23H})_3^{n+}$ parallel 3SCC (one of two different three-helix bundles present in the ASU) at pH 8.5. Shown are the main chain atoms represented as helical ribbons (cyan) and the Pen and His side chains in stick form (sulfur = yellow, nitrogen = blue, oxygen = red). a) One of two trimers found in the ASU of the crystal structure. b) A top-down view of the structural T-shaped thiolate site, $\text{Hg(II)}\text{S}_3$, confirming one of the proposed structures of Hg(II) in Cys-containing TRI peptides.^{16,50} c) A side-on view of the tetrahedral catalytic site, $\text{Zn(II)}\text{N}_3\text{O}$, which closely mimics carbonic anhydrase and matrix metalloproteinase active sites.⁸⁴ All figures are shown with $2F_o - F_c$ electron density contoured at 1.5σ overlaid.

with three His residues and a water/hydroxyl ligand (Figure 2-9c). The $\text{Zn(II)}\text{-N}_{\text{His}}$ distances in both 3SCCs are close to 2.0 Å.

d) Crystallographic Characterization at pH 7.5. The X-ray crystal structure of $[\text{Hg(II)}]_s[\text{Zn(II)(OH}_2/\text{OH}^-)]_N(\text{CSL9PenL23H})_3^{n+}$ was solved to 2.2 Å resolution. Crystals in space group $P2_1$ were obtained at pH 7.5 and the structure was solved using molecular replacement. The resulting model, like that for pH 8.5, $[\text{Hg(II)}]_s[\text{Zn(II)(OH}_2/\text{OH}^-)]_N(\text{CSL9PenL23H})_3^{n+}$, contains two independent well-folded, parallel 3SCCs in the ASU (Figure 2-11a). In both trimers, Hg(II) is bound to the sulfur

atoms of Pen in an apparently dynamic structure. There are two Hg(II) atoms present around each site, one in the interior bound in a T-shaped fashion (Hg(II)-S distances of 2.15, 1.89, and 2.89 Å in the first trimer, ABC, and 1.49, 1.93, 2.93 Å in the DEF trimer (Table 2-5, Figure 2-11b-2-11c)). The second, exterior Hg(II) atom is present in two

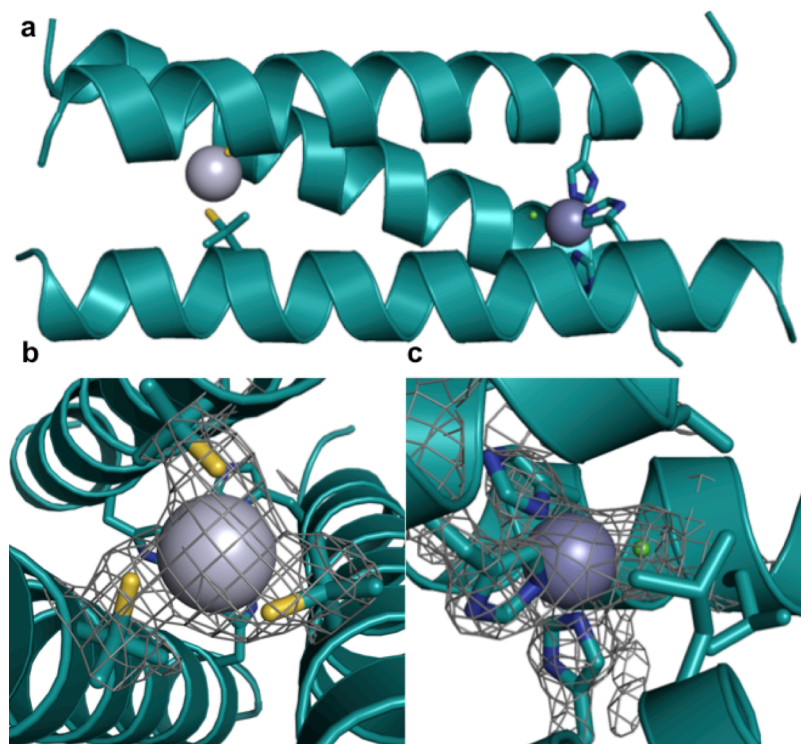


Figure 2-10. Ribbon diagrams of the $[\text{Hg(II)}]_s[\text{Zn(II)(OH}_2/\text{OH}^-)]_N(\text{CSL9PenL23H})_3^{n+}$ parallel 3SCC (one of two different three-helix bundles present in the ASU) at pH 8.5. Shown are the main chain atoms represented as helical ribbons (cyan) and the Pen and His side chains in stick form (sulfur = yellow, nitrogen = blue, oxygen = red). a) One of two trimers found in the ASU of the crystal structure. b) A top-down view of the structural trigonal thiolate site, $\text{Hg(II)}\text{S}_3$, confirming the proposed structure of Hg(II) in Cys-containing TRI peptides.¹⁶ This metal site should mimic well the structural site in the metalloregulatory protein MerR.⁵¹ c) A side-on view of the tetrahedral catalytic site with chloride bound (NaCl is present at 200 mM in the precipitant solution for crystal growth), $\text{Zn(II)}\text{N}_3\text{Cl}$, which also closely mimics carbonic anhydrase and matrix metalloproteinase active sites.⁸⁴ All figures are shown with $2F_o - F_c$ electron density contoured at 1.5σ overlaid.

conformations. In one, Hg(II) is bound to a thiolate from a Pen residue which swings out from the interior (Hg(II)-S = 2.51 Å for ABC and 2.55 Å for DEF), and the other is further from the thiolate and bound only to an exterior Glu residue (Hg(II)-O ~2.6 Å). Four-coordinate Zn(II)N₃Cl sites are found in both trimers, and closely resemble the

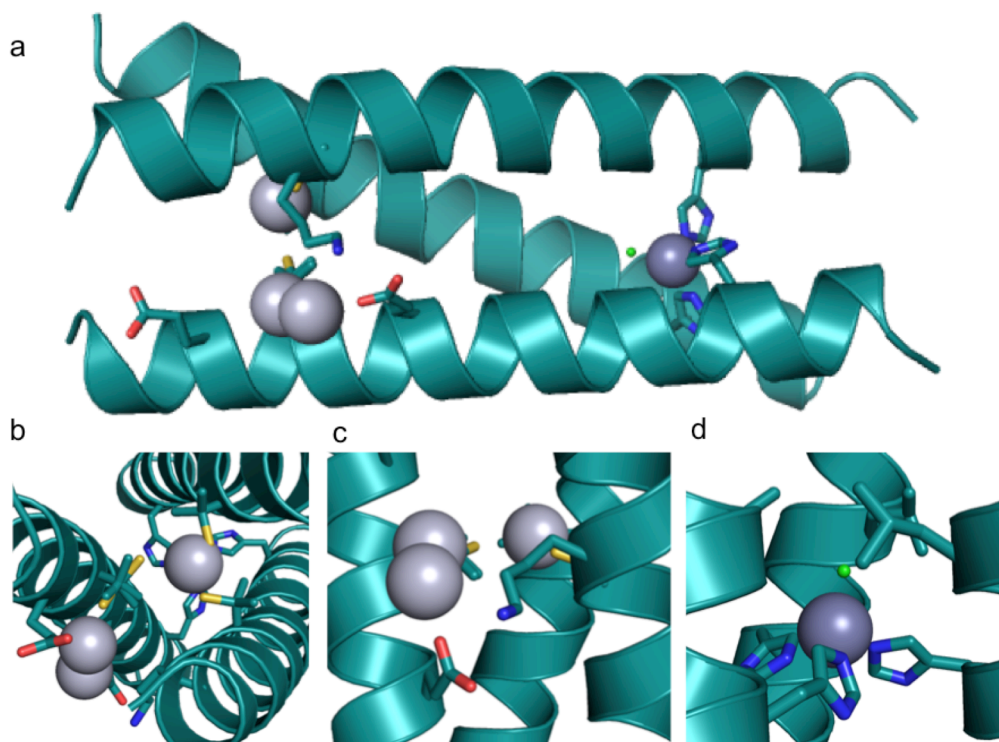


Figure 2-11. Ribbon diagrams of the $[\text{Hg(II)}]_s[\text{Zn(II)(OH}_2/\text{OH)}]_n(\text{CSL9PenL23H})_3^{n+}$ parallel 3SCC (one of two similar three-helix bundles present in the ASU) at pH 7.5. Shown are the main chain atoms represented as helical ribbons (cyan) and the Pen and His side chains in stick form (sulfur = yellow, nitrogen = blue, oxygen = red). a) One of two trimers found in the ASU of the crystal structure (unlike for the pH 8.5 structure, the metal sites in these trimers are nearly identical). b) A top-down view of the T-shaped thiolate site, $\text{Hg(II)}\text{S}_3$, with a dynamic exterior Hg(II) bound to one of the thiolates and exterior carboxylates. c) A side-on view of the Hg(II) site to show how the exterior Hg(II) is bound. d) A side-on view of the tetrahedral catalytic site, $\text{Zn(II)}\text{Cl}_3\text{O}$ (almost identical to that in the pH 8.5 structure), which closely mimics carbonic anhydrase and matrix metalloproteinase active sites.⁸⁴

Zn(II) sites in the pH 8.5 structure. The Zn(II)-N bond distances are all in the range of $\sim 1.9\text{-}2.1$ Å, and Zn(II)-Cl is $\sim 2.2\text{-}2.3$ Å (Table 2-5, Figure 2-11d).

e) Zn(II) Binding to Cys_3 and His_3 Sites. The colorimetric chelator Zincon was used in competitive binding titrations to measure the apparent binding affinities of Zn(II) to $[\text{Hg(II)}]_s(\text{TRIL9CL23H})_3^-$, $(\text{TRIL2WL23H})_3$, $[\text{Hg(II)}]_s(\text{CSL9PenL23H})_3^-$ (which represent potential His_3 binding sites), $(\text{TRIL2WL16C})_3^{n-}$, $(\text{TRIL9C})_3^{n-}$, $(\text{CSL16C})_3^{n-}$ (which represent potential Cys_3 sites), and $(\text{TRIL2W})_3$ and $[\text{Hg(II)}]_s(\text{CSL12C})_3^-$ (as

Table 2-8. Apparent dissociation constants for Zn(II) binding to His₃ and Cys₃ sites in the TRI and CS peptides.^a

Peptide complex	$K_{d,app}$ (μ M) at pH 7.5	$K_{d,app}$ (μ M) at pH 9.0
$[\text{Zn(II)(OH}_2/\text{OH}^-)]_N(\text{TRIL2WL23H})_3^{n+}$	0.6 ± 0.1	0.24 ± 0.02
$[\text{Hg(II)}]_S[\text{Zn(II)(OH}_2/\text{OH}^-)]_N(\text{TRIL9CL23H})_3^{n+}$	0.8 ± 0.1	0.22 ± 0.06
$[\text{Hg(II)}]_S[\text{Zn(II)(OH}_2/\text{OH}^-)]_N(\text{CSL9PenL23H})_3^{n+}$	~ 0.016	0.007 ± 0.001
$[\text{Zn(II)(X)}]_S(\text{TRIL9C})_3^{n+}$	NA	0.0043 ± 0.0015
$[\text{Zn(II)(X)}]_S(\text{TRIL2WL16C})_3^{n+}$	~ 6	0.0034 ± 0.0007
$[\text{Zn(II)(X)}]_S(\text{CSL16C})_3^{n+}$	~ 5	0.0034 ± 0.0012

a. pH 7.5 measured in 50 mM HEPES buffer, 0.1 M Na₂SO₄; pH 9.0 measured in 50 mM CHES buffer, 0.1 M Na₂SO₄.

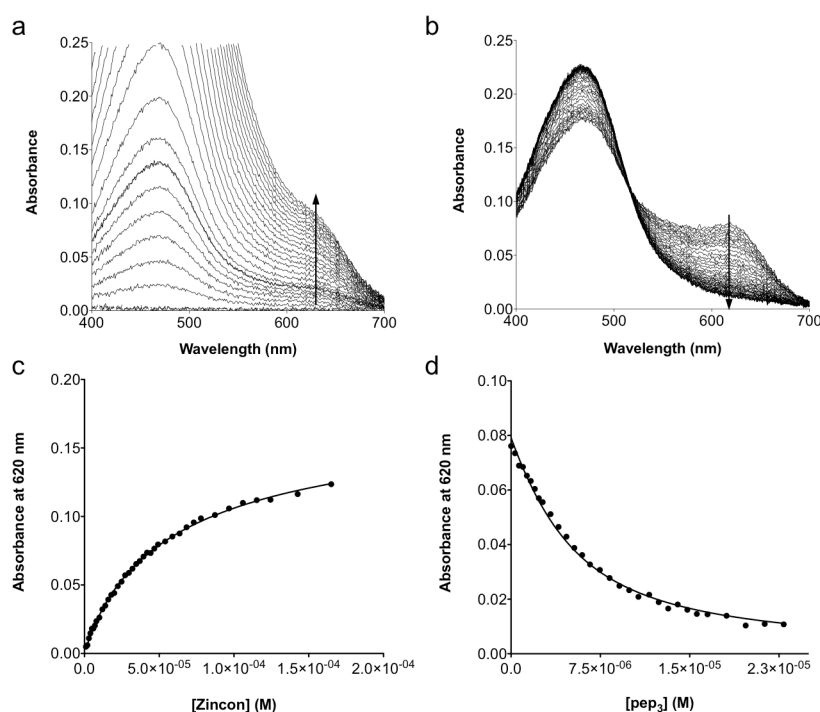


Figure 2-12. Competitive Zn(II)-binding titrations against Zincon at pH 7.5 for [Hg(II)]_S(TRIL9CL23H)₃⁻ in the forward (10 μ M Zn(II)pep₃ + Zincon) and reverse (5 μ M Zn(II)Zi + pep₃) directions. a) Representative UV-Vis spectra for the titration in the forward direction and b) in the reverse direction. c) Plot of absorbance at 620 nm as a function of increasing [Zincon] for the forward titration and d) as a function of increasing [pep₃] for the reverse titration.

controls which should not contain free metal-binding sites). The binding affinities were measured for at least one pH, 7.5 or 9.0, if not both. Apparent dissociation constants resulting from fits of the data (as described in Materials and Methods) are reported in Table 2-8. Representative plots of fitted data are shown for [Hg(II)]_S(TRIL9CL23H)₃⁻ and (TRIL2WL23H)₃ at pH 7.5 and 9.0 (Figures 2-12-2-14). Similar dissociation

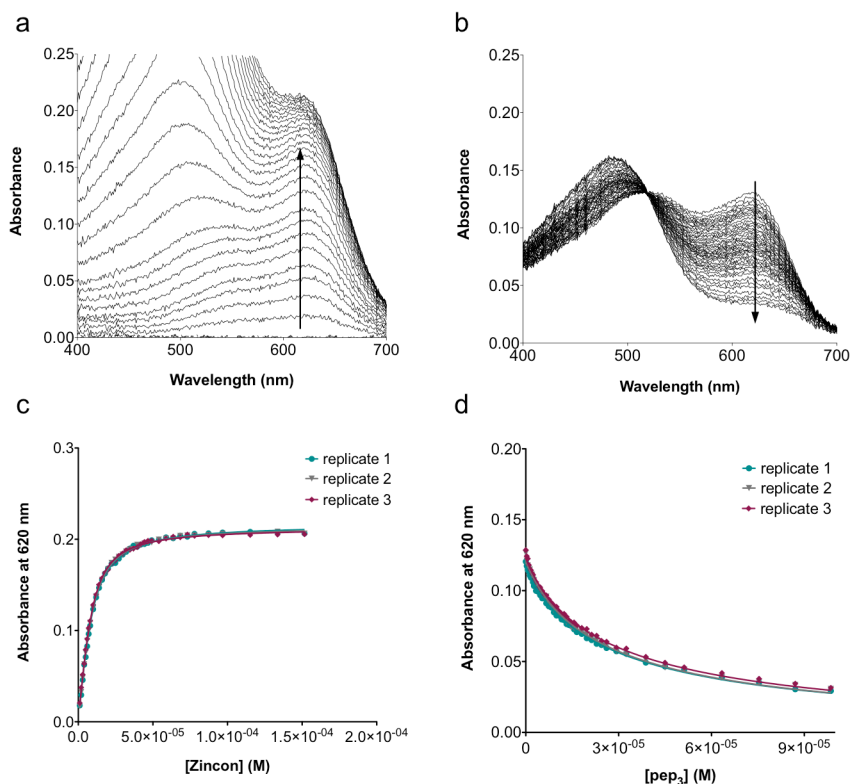


Figure 2-13. Competitive Zn(II)-binding titrations against Zincon at pH 9.0 for [Hg(II)]_s(TRIL9CL23H)₃⁻ in the forward (10 μM Zn(II)pep₃ + Zincon) and reverse (5 μM Zn(II)Zi + pep₃) direction. a) Representative UV-Vis spectra for the titration in the forward direction and b) in the reverse direction. c) Plot of absorbance at 620 nm as a function of increasing [Zincon] for the forward titration and d) as a function of increasing [pep₃] for the reverse titration.

constants were obtained at both pH's examined for the His-containing peptides [Hg(II)]_s(TRIL9CL23H)₃⁻ and (TRIL2WL23H)₃, ~0.7 μM for pH 7.5 and ~0.2 μM for pH 9.0. Stronger dissociation constants at both pH's were determined for the crystallographic analog [Hg(II)]_s(CSL9PenL23H)₃⁻, perhaps due to the presence of another His in the sequence near the C-terminus. This may be expected since there are often multiple exterior Zn(II) sites found in the CS crystal structures (which aid in the formation of diffraction-quality crystals). Zn(II) binding to Cys₃ sites in both TRI and a CS peptide indicate relatively weak binding at pH 7.5 (~5-6 μM) and very strong binding at pH 9.0, ~3-4 nM. These binding affinities for Zn(II) to Cys₃ at pH 7.5 and especially pH 9.0, highlight the importance of using Hg(II) to “block” the structural site in order to drive complete Zn(II) binding to the His site.

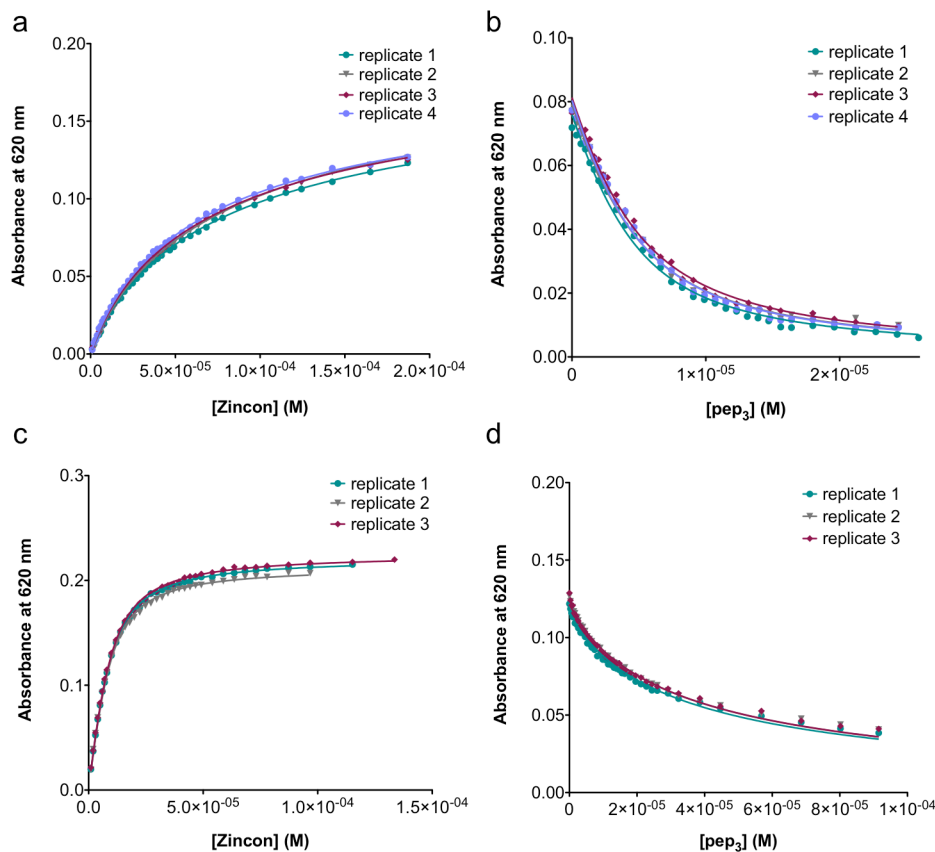


Figure 2-14. Competitive Zn(II)-binding titrations against Zincon for (TRIL2WL23H)₃ in the forward (10 μM Zn(II)pep₃ + Zincon) and reverse (5 μM Zn(II)Zi + pep₃) directions at each pH. Plots of absorbances at 620 nm vs [Zincon] at pH 7.5 for the a) forward titration and b) reverse titration and at pH 9.0 for the c) forward titration and d) reverse titration.

Characterization of Ester Hydrolysis and Inhibition

a) Zn(II) Site in Original Models.

[Hg(II)]_S[Zn(II)(OH₂/OH⁻)]_N(TRIL9CL23H)₃ⁿ⁺ exhibits saturation kinetics for *p*NPA hydrolysis in buffered aqueous solution, with $k_{\text{cat}} = 2.2 (\pm 0.5) \times 10^{-3} \text{ s}^{-1}$ and $k_{\text{cat}}/K_{\text{M}} = 1.38 \pm 0.04 \text{ M}^{-1} \text{ s}^{-1}$ at pH 7.5 (25 °C, 10 μM catalyst, turnover number (TON) > 10, Table 2-9). Both rate and catalytic efficiency of [Hg(II)]_S[Zn(II)(OH₂/OH⁻)]_N(TRIL9CL23H)₃ⁿ⁺ increase as a function of increasing pH (presumably due to deprotonation of the Zn(II)-aqua ligand to produce the active Zn(II)-hydroxide species). $k_{\text{cat}}/K_{\text{M}}$ of up to $23.3 \pm 0.3 \text{ M}^{-1} \text{ s}^{-1}$ can be reached at pH 9.5, while the K_{M} values remain essentially constant (~

Table 2-9. pH-dependent kinetic parameters for hydrolysis of *p*NPA by TRI peptides^a as compared to CAII.

Catalyst ^b	pH ^c	k_{cat}/K_M [M ⁻¹ s ⁻¹]	k_{cat} [s ⁻¹]	K_M [mM]
[Zn(II)(OH ₂ /OH ⁻)] _N (TRIL2WL23H) ₃ ⁿ⁺ pK _a = 9.2 ± 0.1	7.5	0.41 ± 0.03	0.0011 ± 0.0002	2.7 ± 0.8
	8.0	1.07 ± 0.06	0.0029 ± 0.0005	2.7 ± 0.6
	8.5	3.3 ± 0.2	0.0060 ± 0.0007	1.8 ± 0.3
	9.0	8.9 ± 0.4	0.016 ± 0.001	1.8 ± 0.2
	9.25	12.9 ± 0.4	0.022 ± 0.001	1.7 ± 0.2
	9.5	15.5 ± 0.4	0.033 ± 0.002	2.1 ± 0.2
	max ^d	25 ± 2		
[Hg(II)] _S [Zn(II)(OH ₂ /OH ⁻)] _N (TRIL9CL23H) ₃ ⁿ⁺ pK _a = 9.0 ± 0.1	7.5	1.38 ± 0.04	0.0022 ± 0.0005	1.6 ± 0.4
	8.0	3.1 ± 0.1	0.0054 ± 0.0015	1.7 ± 0.5
	8.5	6.0 ± 0.1	0.012 ± 0.004	1.9 ± 0.6
	8.75	10.8 ± 0.3	0.021 ± 0.010	2.0 ± 0.9
	9.0	17.6 ± 0.3	0.038 ± 0.010	2.1 ± 0.6
	9.5	23.3 ± 0.3	0.040 ± 0.012	1.7 ± 0.5
	max ^d	31 ± 4		
CAII pK _a = 6.8	7.0 ^e	1670	37 ± 10	22.1 ± 5.0
	7.4 ^f	2600 ± 5		30.53 ± 2.10
	8.0 ^e	2550	53 ± 10	20.7
	9.0 ^e	2320	56 ± 10	23.9

a. Error bars result from fitting all individual rates measured (three per concentration of substrate, without averaging) to the Michaelis-Menten equation in Prism 5 (GraphPad Software)³⁵ or from Lineweaver-Burke analysis.

b. 10-20 μM active Zn(II)-bound complex.

c. pH 7.5-8.0 measured in 50 mM HEPES, 0.1 M Na₂SO₄; pH 8.5-9.5 measured in 50 mM CHES, 0.1 M Na₂SO₄.

d. Maximal catalytic efficiency from the fitting of k_{cat}/K_M values vs pH (assuming 100% active enzyme complex is present).

e. Taken from ref. 36.

f. Taken from ref. 78.

mM, within error) over the range. pH-dependency profiles can be fitted (for the midpoint) to yield pK_a's of 8.82 ± 0.11 for k_{cat}/K_M vs pH and 8.77 ± 0.08 for k_{cat} vs pH, suggesting that the rate-limiting step is chemical in nature (Figure 2-15). When the pH-dependency profile is fitted to equation 5,

$$k_{obs} = \frac{(k_{max} * 10^{(pH-pK_a)}) + k_{min}}{1 + 10^{(pH-pK_a)}} \quad (5)$$

a similar pK_a of 9.0 ± 0.1 is obtained and the maximal k_{cat}/K_M (when 100% hydroxide is present) can be determined, 31 ± 4 M⁻¹ s⁻¹ (Figure 2-16). Notably, variation of the concentration of [Hg(II)]_S[Zn(II)(OH₂/OH⁻)]_N(TRIL9CL23H)₃ⁿ⁺ relative to substrate at

pH 9.5 confirms that the reaction is first order in Zn(II) protein concentration over the tested range of 10 to 60 μM catalyst. The activity of $[\text{Zn}(\text{II})(\text{OH}_2/\text{OH}^-)]_{\text{N}}(\text{TRIL2WL23H})_3^{n+}$ was measured as a comparison lacking the structural site. The kinetic parameters are similar to those with the structural site, except possibly at pH 9.5 where $[\text{Zn}(\text{II})(\text{OH}_2/\text{OH}^-)]_{\text{N}}(\text{TRIL2WL23H})_3^{n+}$ has a slightly decreased efficiency which may be attributed to decreased stability of the complex in basic media (Table 2-9). The $\text{p}K_{\text{a}}$ and maximal $k_{\text{cat}}/K_{\text{M}}$ for this complex are 9.2 ± 0.1 and $25 \pm 2 \text{ M}^{-1} \text{ s}^{-1}$, respectively. The same trends are observed for the other kinetic parameters, k_{cat} (increasing with pH) and K_{M} ($\sim 2 \text{ mM}$ at all pH's) (Figure 2-17). When this work was first reported, the complex $[\text{Zn}(\text{II})(\text{OH}_2/\text{OH}^-)]_{\text{N}}(\text{TRIL23H})_3^{n+}$ was also measured for its hydrolytic activity towards *p*NPA. While the sample concentrations of this peptide, lacking a spectroscopic tag, are not as accurate as those for TRIL2WL23H, similar kinetic parameters were observed, with a small loss at higher pH. The $\text{p}K_{\text{a}}$ based on the midpoint of the profile was estimated at ~ 9.0 .

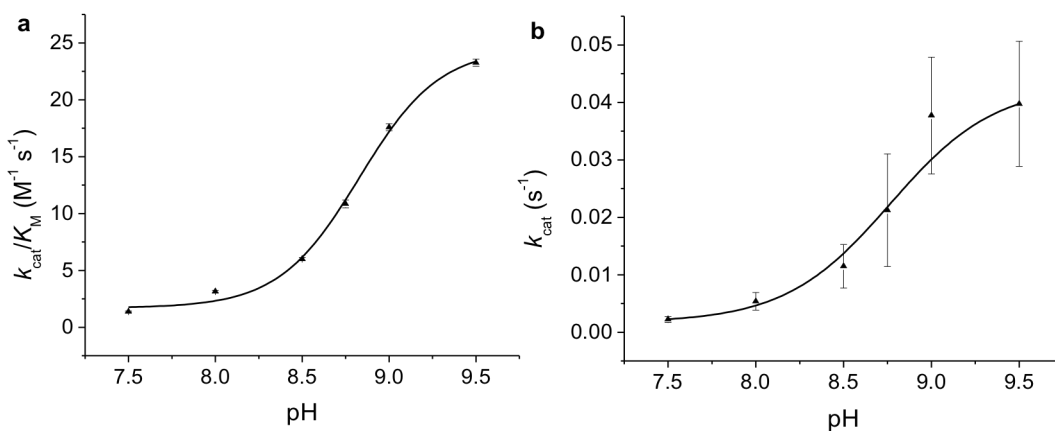


Figure 2-15. pH-dependency of *p*NPA hydrolysis by $[\text{Hg}(\text{II})]_{\text{S}}[\text{Zn}(\text{II})(\text{OH}_2/\text{OH}^-)]_{\text{N}}(\text{TRIL9CL23H})_3^{n+}$. Plots of a) $k_{\text{cat}}/K_{\text{M}}$ vs pH and b) k_{cat} vs pH for the hydrolysis of *p*NPA by $[\text{Hg}(\text{II})]_{\text{S}}[\text{Zn}(\text{II})(\text{OH}_2/\text{OH}^-)]_{\text{N}}(\text{TRIL9CL23H})_3^{n+}$ (10 μM). $\text{p}K_{\text{a}}$ values of 8.82 ± 0.11 and 8.77 ± 0.08 for plots a) and b), respectively, can be determined from the fittings and presumably represent the deprotonation of Zn-OH₂ to form an active Zn-OH⁻ nucleophile, as with CAII. The fitting and error analysis can be found in the Materials and Methods section.

b) Controls. Given that imidazole is known to catalyze *p*NPA hydrolysis, the apo-peptide (containing three imidazoles in the trimer) also facilitates hydrolysis with an

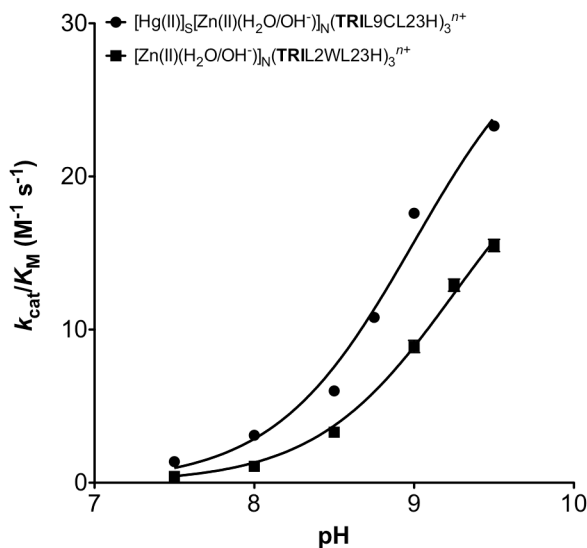


Figure 2-16. pH-dependency of the catalytic efficiency for *p*NPA hydrolysis by Zn(II)-bound TRI peptides: [Hg(II)]_S[Zn(II)(OH₂/OH⁻)]_N(TRIL9CL23H)₃ⁿ⁺ (●), [Zn(II)(OH₂/OH⁻)]_N(TRIL2WL23H)₃ⁿ⁺ (■). Error bars (small and hard to see on this plot) result from fitting all individual initial rates measured (three per concentration of substrate, without averaging) to the Michaelis-Menten equation in Prism 5 (GraphPad Software).³⁵ The fitting equation used for the pH-dependence (eq 5) is described in the Discussion section.

efficiency at pH 9.0 that represents ~30% of that of the Zn(II)-bound trimer (this activity is accounted for in the values reported for Zn(II)-facilitated hydrolysis) (Table 2-10). As described above, [Hg(II)]_S[Zn(II)(OH₂/OH⁻)]_N(TRIL9CL23H)₃ⁿ⁺ exhibits a catalytic efficiency of $23.3 \pm 0.3 \text{ M}^{-1} \text{ s}^{-1}$ at pH 9.5 and of $17.6 \pm 0.3 \text{ M}^{-1} \text{ s}^{-1}$ at pH 9.0. Importantly, in the presence of Hg(II), but in the absence of Zn(II), an efficiency of only $6.0 \pm 0.1 \text{ M}^{-1} \text{ s}^{-1}$ was measured at pH 9.0 (Table 2-10). In the absence of both metals, apo-(TRIL9CL23H)₃ⁿ⁻ exhibits an identical catalytic efficiency. These both represent ~34% of the activity of the Zn(II)-bound version. The fact that the values are the same in the presence and absence of Hg(II) indicates that this activity is due primarily to the three His residues in the trimer acting as catalysts. This observation is within a factor of two of the catalytic efficiency for His-based hydrolysis of *p*NPA reported by Bolon and Mayo.⁴⁰ The rate of apo-CA towards *p*NPA hydrolysis is not readily available in the literature as a catalytic efficiency or second order rate constant value. Typically, the background activity is measured using the acetazolamide-inhibited enzyme, in which case the free imidazole residues are still bound to Zn(II) and therefore not available to contribute to

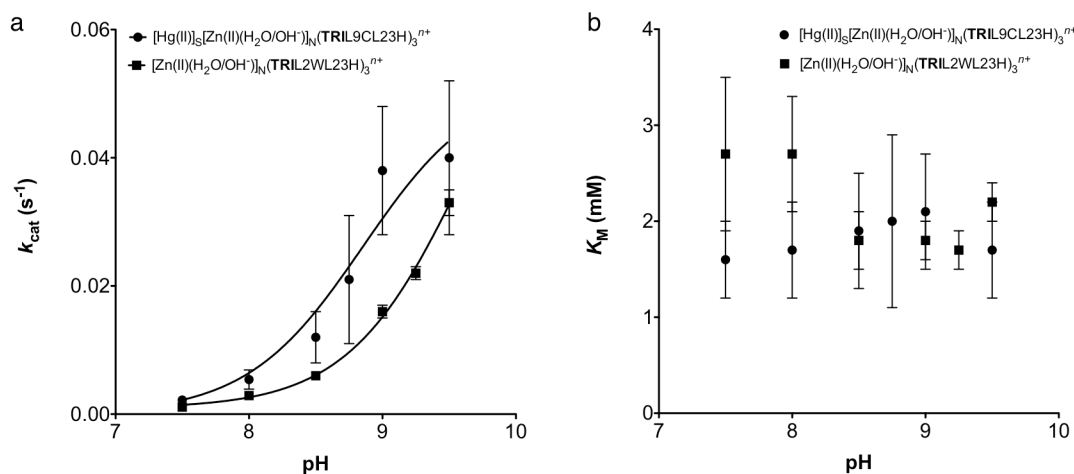


Figure 2-17. pH-dependency of a) k_{cat} and b) K_M parameters for *p*NPA hydrolysis by Zn(II)His₃O sites in the TRI peptides. Results are shown for 20 μ M [Zn(II)(OH₂/OH⁻)]_N(TRIL2WL23H)₃ⁿ⁺ and 10 μ M [Hg(II)]_S[Zn(II)(OH₂/OH⁻)]_N(TRIL9CL23H)₃ⁿ⁺ in 50 mM HEPES (pH 7.5-8.0) or CHES (pH 8.5-9.5), both 0.1 M Na₂SO₄. Error bars result from fitting all individual initial rates measured (three per concentration of substrate, without averaging) to the Michaelis-Menten equation in Prism 5 (GraphPad Software).³⁵ The fitting equation used for the pH-dependence (eq 5) is described in the Discussion section.

catalysis.

In order to determine the activity of an unbound Zn(II) control peptide (that is, with Zn(II) present but not bound in the designed His₃ site), **TRIL9C** was used. This peptide has Leu residues in place of His at the 23rd position. [Hg(II)]_S(**TRIL9C**)₃⁻ and [Hg(II)]_S(**TRIL9C**)₃⁻ + Zn(II) were run in parallel. The difference between the two rates is essentially negligible (k_{cat}/K_M values were $1.9 \pm 0.3 \text{ M}^{-1} \text{ s}^{-1}$ in the absence of Zn(II) and $1.8 \pm 0.2 \text{ M}^{-1} \text{ s}^{-1}$ in its presence (Table 2-10)). These results support the conclusion that Zn(II) must be bound to the designed His₃ site to observe the reported high activity.

A control experiment in which the trimer is denatured was performed at pH 9.0 in the presence of $\sim 4.8 \text{ M}$ GuHCl. For this experiment, the initial rate at only a single concentration of *p*NPA (500 μ M) was determined and corrected for spontaneous background hydrolysis. Approximately 12% activity in the presence of Zn(II) is observed over the [Hg(II)]_S(**TRIL9CL23H**)₃⁻ peptide without Zn(II). From the GuHCl denaturation curve, the peptide is approximately 6% folded at this concentration (using an ideal ellipticity of -35500 to calculate percent folding). Given that the activity and the folding

Table 2-10. Comparisons of the kinetics for pNPA hydrolysis by selected catalysts at 25 °C.

Catalyst	pK _a ^a	pH	k _{cat} /K _M (M ⁻¹ s ⁻¹)	k ₂ (M ⁻¹ s ⁻¹)
[Hg(II)] _s [Zn(II)(OH)] _N	8.8	9.5	23.3 ± 0.3	
(TRIL9CL23H) ₃ ⁿ⁺		9.0	17.6 ± 0.3	
[Hg(II)] _s [Zn(II)(OH ₂)] _N	8.8	7.5	1.38 ± 0.04	
(TRIL9CL23H) ₃ ⁿ⁺				
[Hg(II)] _s (TRIL9CL23H) ₃ ⁻	-	9.0	6.0 ± 0.1	
apo-(TRIL9CL23H) ₃ ⁿ⁻	-	9.0	6.0 ± 0.1	
[Zn(II)] _N (TRIL23H) ₃ ⁿ⁺	9.0	9.0	14.1 ± 0.3	
[Hg(II)] _s [Zn(II)(OH)] _N	ND	9.5	20.2 ± 2.3 ^b	
(CSL9PenL23H) ₃ ⁿ⁺				
[Hg(II)] _s (TRIL9C) ₃ ⁻	-	9.0	1.9 ± 0.3	
[Hg(II)] _s (TRIL9C) ₃ ⁻ +Zn(II)	-	9.0	1.8 ± 0.2	
CAII ^c	6.8	9.0	2320	
CAI ^c	7.3	9.0	370	
[12]aneN ₃ ^d	7.3	8.2		0.041
[15]aneN ₃ O ₂ ^e	8.8			0.6
tris(4,5-di- <i>n</i> -propyl-2-imidazolyl) phosphine	8.7			0.86/0.0186 ^f
[12]aneN ₄ ^g	7.9	9.3		0.1
[12]aneN ₄ hexadecyl derivative ^h	7.56	10.5		5
KO-42	-	5.1/7.0		0.29/~0.7 ⁱ
PZD2 ^j	-	7.0	2.7	

a. For deprotonation of Zn(II)-OH₂ to form catalytically active Zn(II)-OH⁻ in Zn(II)N_x (in CA and CA-like models)

b. Normalized according to the folding concentration of [Hg(II)]_s(CSL9PenCL23H)₃⁻ relative to [Hg(II)]_s(TRIL9CL23H)₃⁻.

c. Taken from ref. 36.

d. Taken from ref. 63.

e. Estimated by extrapolating to the 100% active Zn(II)-OH⁻ form of the complex from pH-dependent data.⁶⁶

f. The former value is that measured in micellar medium; the latter estimated under aqueous conditions.⁶⁵

g. Taken from ref. 69.

h. Taken from ref. 70.

i. *De novo* designed four-helix bundle containing six His residues that contribute to a second-order rate constant and whose value at pH 7.0 is extrapolated from the reported value at pH 5.1 of 0.29 M⁻¹ s⁻¹ using pH rate profiles reported for similarly activated esters.^{40,71,72}

j. A computationally redesigned thioredoxin to include a nucleophilic His residue.⁴⁰

Table 2-11. Kinetic parameters for the inhibition of *p*NPA hydrolysis by Zn(II)-bound TRI peptides at pH 8.5.^a

Peptide complex ^b & its K_I (M)	[OAc ⁻] [M]	k_{cat}/K_M [M ⁻¹ s ⁻¹]	k_{cat} [s ⁻¹]	K_M [mM]
[Zn(II)(OH ₂ /OH ⁻)] _N (TRIL2WL23H) ₃ ⁿ⁺ $K_I = 0.34 \pm 0.01$	0	3.2 ± 0.1	0.0065 ± 0.0006	2.0 ± 0.3
	0.1	2.51 ± 0.05	0.0068 ± 0.0004	2.7 ± 0.2
	0.25	2.01 ± 0.07	0.0058 ± 0.0006	2.9 ± 0.4
	0.435	1.32 ± 0.07	0.0067 ± 0.0021	5.1 ± 1.9
[Hg(II)] _S [Zn(II)(OH ₂ /OH ⁻)] _N (TRIL9CL23H) ₃ ⁿ⁺ $K_I = 0.32 \pm 0.01$	0	5.4 ± 0.1	0.011 ± 0.001	2.0 ± 0.2
	0.1	4.5 ± 0.2	0.012 ± 0.001	2.6 ± 0.4
	0.2	3.6 ± 0.2	0.010 ± 0.002	2.6 ± 0.6
	0.4	2.5 ± 0.1	0.012 ± 0.003	5.0 ± 1.2
	0.6	1.8 ± 0.1	0.010 ± 0.003	5.7 ± 1.8

a. Error bars result from fitting all individual initial rates measured (three per concentration of substrate, without averaging) to the Michaelis Menten equation in Prism 5 (GraphPad Software).³⁵

b. 20 μM active Zn(II)-bound peptide complex.

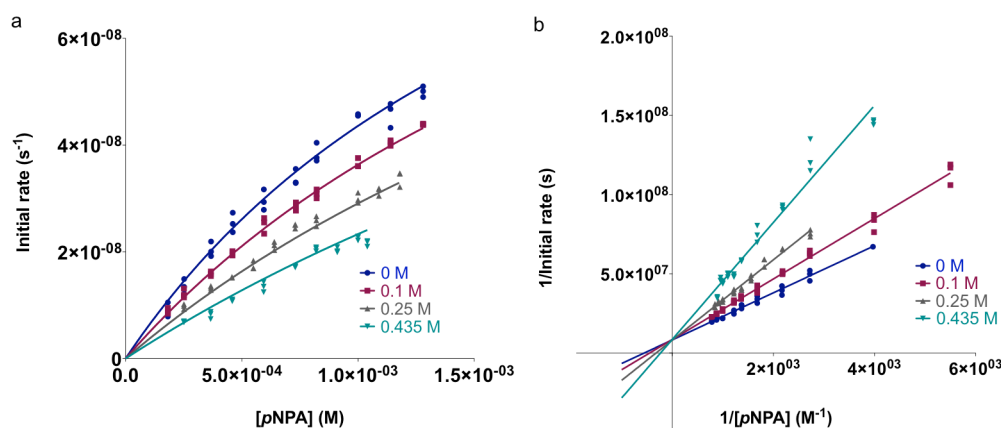


Figure 2-18. Inhibition of 20 μM [Zn(II)(OH₂/OH⁻)]_N(TRIL2WL23H)₃ⁿ⁺-catalyzed *p*NPA hydrolysis by acetate. a) Initial rates as a function of substrate concentration in the presence of 0 M, 0.1 M, 0.25 M, and 0.435 M KOAc fitted to a competitive inhibition model in Prism 5 (GraphPad Software).³⁵ The global data yields the reported K_I and corresponding error. Data shown consists of each individual measured initial rate and does not represent averages. Fitting the same data to a mixed inhibition model yielded $\alpha \approx 6 \times 10^{19}$ supporting the assignment of a competitive inhibition model.³⁷ b) Lineweaver-Burke (double-reciprocal) plots corresponding to the data in a). Visual inspection of the intersection of linear fits to each dataset (at the y-axis) also supports a competitive inhibition model.

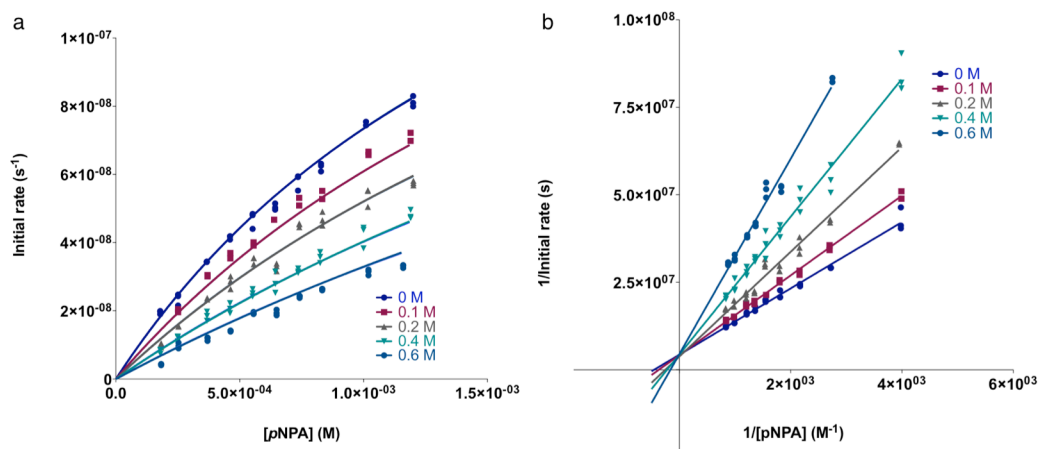


Figure 2-19. Inhibition of 20 μM $[\text{Hg}(\text{II})]_S[\text{Zn}(\text{II})(\text{OH}_2/\text{OH}^-)]_N(\text{TRIL9CL23H})_3^{n+}$ -catalyzed *p*NPA hydrolysis by acetate at pH 8.5. a) Initial rates as a function of substrate concentration in the presence of 0, 0.1, 0.2, 0.4, and 0.6 M KOAc fitted to a competitive inhibition model in Prism 5 (GraphPad Software).³⁵ The global data yields the reported K_i and corresponding error. Data shown consists of each individual measured initial rate and does not represent averages. Fitting the same data to a mixed inhibition model yielded $\alpha \approx 14$ supporting the assignment of a competitive inhibition model.⁸⁵ b) Lineweaver-Burke (double-reciprocal) plots corresponding to the data in a). Visual inspection of the intersection of linear fits to each dataset (at the y-axis) also supports a competitive inhibition model.

percentages are within experimental error, it is expected that the residual activity observed is due to the residual folded peptide.

Notably, the activity of the crystallographic analog $[\text{Hg}(\text{II})]_S[\text{Zn}(\text{II})(\text{OH}_2/\text{OH}^-)]_N(\text{CSL9PenL23H})_3^{n+}$ was measured at pH 9.5 and, after correcting for the folding concentration, a catalytic efficiency of $20.2 \pm 2.3 \text{ M}^{-1} \text{ s}^{-1}$ is obtained. This compares well to that for $[\text{Hg}(\text{II})]_S[\text{Zn}(\text{II})(\text{OH}_2/\text{OH}^-)]_N(\text{TRIL9CL23H})_3^{n+}$, which is $23.3 \pm 0.3 \text{ M}^{-1} \text{ s}^{-1}$.

c) Product Inhibition. The peptide complexes $[\text{Hg}(\text{II})]_S[\text{Zn}(\text{II})(\text{OH}_2/\text{OH}^-)]_N(\text{TRIL9CL23H})_3^{n+}$ and $[\text{Zn}(\text{II})(\text{OH}_2/\text{OH}^-)]_N(\text{TRIL2WL23H})_3^{n+}$ were measured for the extent of product inhibition at pH 8.5. The kinetic parameters at each concentration of acetate are given in Table 2-11. As described in the Materials and Methods section, both peptide complexes fit a competitive inhibition model, as based on non-linear competitive fits and Lineweaver-Burke analysis (Figures 2-18-2-19). The α -values obtained from

non-linear mixed inhibition fits in Prism 5 (GraphPad Software)³⁵ further support a competitive inhibition model ($\alpha > 1$).³⁷ No inhibition was observed at pH 9.5.

The apo-peptides can also catalyze *p*NPA hydrolysis due to the presence of free His residues. A control experiment in which I attempted to inhibit this activity using 0.5 M acetate showed some inhibition (it is possible that acetate may block *p*NPA from entering the 3SCC to some extent), but it was less than half of that observed in the presence of Zn(II) and did not strictly fit any inhibition model. Therefore, I conclude that the observed competitive inhibition is due to acetate competing for the ZnN₃O site.

Discussion

The aim of the work presented in this chapter is to create a *de novo* designed protein, which could bind two different metals in spatially separated sites, with different functions. The sequence chosen to achieve this original goal is **TRIL9CL23H**, where His in the 23rd position is intended for formation of a catalytic ZnHis₃X site, like that in CA. In addition to this envisioned catalytic site, a stabilizing structure site (HgS₃) was engineered into the 9th position utilizing principles for heavy metal binding defined by earlier work in the group (Chapter 1). The strategy for distinguishing the sites quantitatively was to use an ion with high affinity for thiolate ligation but low affinity for His ligands (Hg(II)) while exploiting the high stability of the Hg(II)-thiolate ligation to allow discrimination of Zn(II) solely to the His position. Thus, the structural site is made up of Hg(II) bound to three thiolates, which stabilizes the pre-folded structure. In Chapter 1, I discussed how Cys-substituted **TRI** peptides can be used to enforce a trigonal coordination environment on Hg(II) and also how Hg(II) can be used to induce the folding of a random coil structure with the **Baby** peptides.^{6,41} Here, the aim was to use this work in order to generate a peptide in which the presence of Hg(II) would lead to a more thermodynamically stable complex in the face of the presence of a second, separate metal-binding site made up of His residues. The second part of this aim was to incorporate His residues in place of one layer of Leu residues in the interior of **TRI** for generation of an active site similar to that in CA (ZnN₃O), which catalyzes the reversible hydration of CO₂ and is one of the fastest known zinc metalloenzymes.⁴² Although these

sequences can withstand multiple thiol substitutions⁴³, it was not known whether or not the incorporation of His residues would lead to a stable construct. Therefore, it was not initially desirable to place a bulky substitution in the center of the sequence where it may interrupt the packing in the middle of the coiled coil structure. Based on previous CS crystal structures containing solely thiol substitutions, the C-terminal end of the 3SCC tends to be more ‘frayed’ than the N-terminus and, therefore, it was hypothesized that this location (the 23rd position) could better accommodate bulkier residues. Finally, an **a** site was chosen instead of a **d** site since previous work involving heavy metal binding to thiolates indicates that most metals bind better to the **a** positions.^{15,39,43–45}

To address the objectives of this chapter, two peptides were initially examined, **TRIL9CL23H**, containing both a Cys substitution for the structurally stabilizing metal site and a separate His substitution for preparation of the transition metal site, and **TRIL23H**, containing only the His substitution for comparison. Having ensured that Hg(II) could bind in a trigonal manner to the thiol site of **TRIL9CL23H** (UV-Vis and NMR spectroscopy as described in the Results section), GuHCl denaturation experiments were performed with the goal of both ensuring folding of each peptide and monitoring the stability of the complexes in the presence and absence of Hg(II). Each peptide folds well with ~70-80% α -helical content, representing formation of the coiled coil in the absence of any denaturant and confirming that the **TRI** peptides can accommodate the bulky His

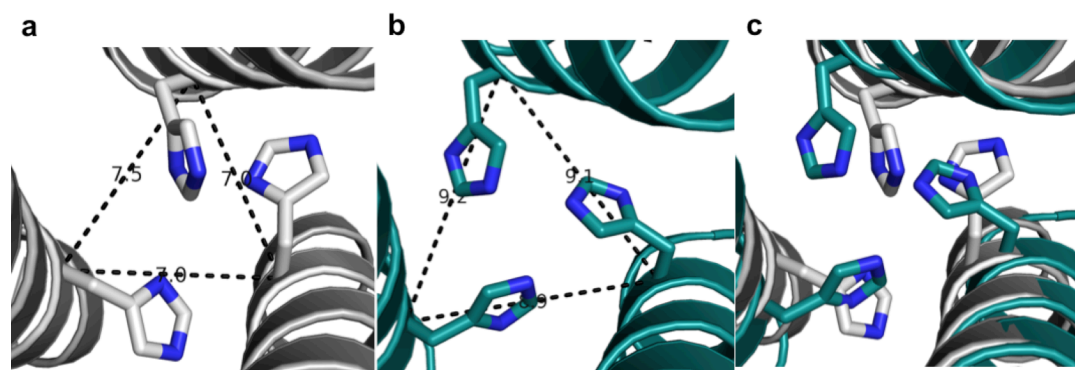


Figure 2-20. Comparison of the size of the active site cavities of (a) modeled apo-His₃ site in the 23rd position using the structure of [As(III)]_S(CSL9C)₃ (pdb 2JGO)⁴⁶ and (b) the actual structure containing the Zn(II)His₃ site (Zn(II) not shown), [Hg(II)]_S[Zn(II)(OH₂/OH)]_N(CSL9PenL23H)₃ⁿ⁺ (pdb 3PBJ)¹². (c) Overlay of the two sites with the model in gray and the actual structure in cyan.

substitution at the 23rd position (although this is somewhat lower than the folding for any reported peptides containing a single thiol substitution (~90%), due to increased fraying at the C-terminus (Figure 2-20)). The results from the GuHCl denaturation titrations indicate that the midpoint for unfolding of the doubly-substituted (**TRIL9CL23H**)₃ⁿ⁻ is at a lower concentration of denaturant than that for (**TRIL23H**)₃ (Figure 2-6). The lower stability of (**TRIL9CL23H**)₃ⁿ⁻ is anticipated as an additional hydrophobic packing layer has been substituted. As expected, a significant shift of the midpoint to a higher concentration is observed in the denaturation for [Hg(II)_S](**TRIL9CL23H**)₃⁻, incorporating the structural HgS₃ site, as compared to that for both apo-peptides. This shift clearly demonstrates the success and benefit of incorporating a structural Hg(II)S₃ site into the design.

The increased stabilization gained through incorporating a structural site facilitates growth of X-ray quality crystals of a derivative of the analogous **CoilSer** (**CS**) peptide, **CSL9PenL23H** (**CoilSer** behaves very similarly to the **TRI** peptide family, but is more amenable for crystallographic characterization).^{24,46} Although this peptide demonstrates poorer folding than the **TRI** analogs, Hg(II) provides increased stabilization (Figure 2-8). Excitingly, the Zn(II)His₃X site closely resembles that found in CA (pdb 2CBA, Figure 2-21a, b) and matrix metalloproteinases (MMPs) such as adamalysin II (pdb 1IAG, Figure 2-21c, d). It is important to point out that although the resemblance of the ZnN₃O site matches these native metalloenzyme active sites, the surrounding secondary interactions and protein folds differ drastically. Focusing on CA, the active site is embedded in a structure primarily made up of β-sheets whereas the designed structure is all α-helical. There are smaller differences in the primary site itself, in that the nitrogen atoms coordinating Zn(II) in the model are all in ε positions whereas CA has a mixed two ε and one δ structure, and also in the general orientations of the imidazole rings. The solvent molecule on Zn(II) in the model is in an identical position to that bound to Zn(II) in CA, but is shifted relative to the Zn(II)-bound solvent molecule in adamalysin II. While crystal structures at both pH 7.5 and 8.5 indicate little to no difference in the ZnN₃X site geometries, there are differences in the fourth coordination site, which is either chloride or a solvent molecule (Figures 2-9-2-11). In all cases, the position of the solvent or chloride on the Zn(II) center remains identical, but binding of chloride in some

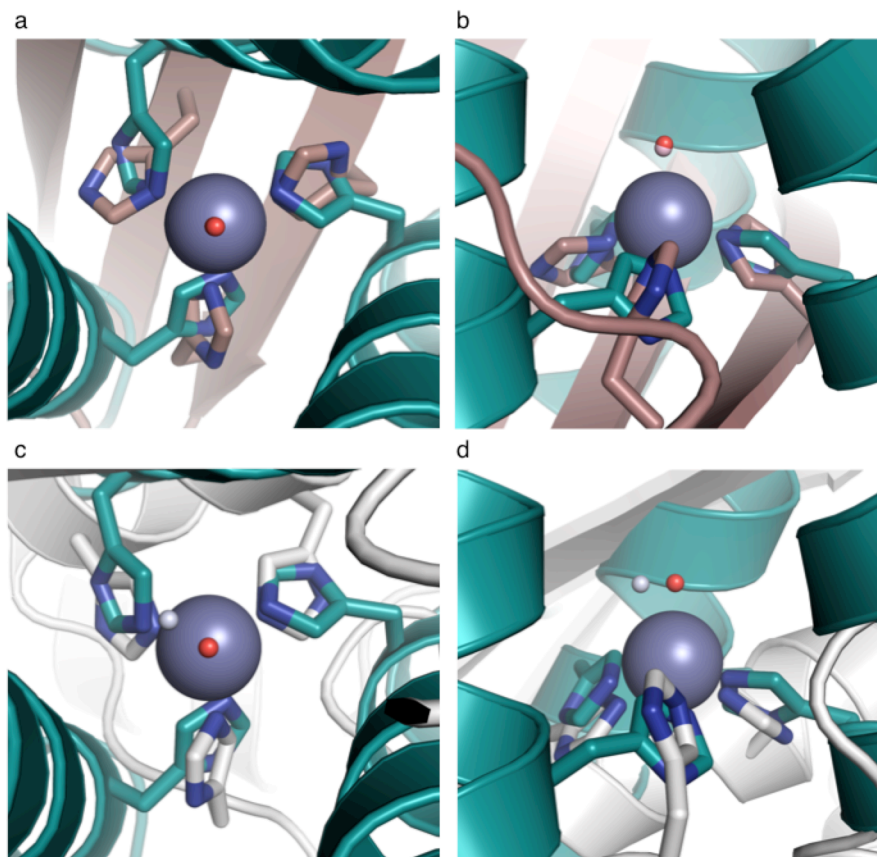


Figure 2-21. Overlay of the Zn(II)N₃O site in [Hg(II)]_s[Zn(II)(OH₂/OH)]_N(CSL9PenL23H)₃⁺⁺ with the active site of human CAII and the MMP adamalysin II. [Hg(II)]_s[Zn(II)(OH₂/OH)]_N(CSL9PenL23H)₃⁺⁺ is shown in cyan (pdb 3PBJ), CAII in tan (pdb 2CBA), and adamalysin II in grey (pdb code 1IAG). a) Top-down view of the overlay with CAII. The solvent molecule associated with [Hg(II)]_s[Zn(II)(OH₂/OH)]_N(CSL9PenL23H)₃⁺⁺ is shown in red and that associated with CAII lies underneath. b) Side-on view of the overlay with CAII. The model displays an excellent structural overlay for the first coordination sphere atoms with CAII; however, the orientation of the imidazoles differs between the two proteins. Another subtle difference is that the present structure has three ϵ amino nitrogens bound to the Zn(II) ion whereas CAII has a mixed two ϵ and one δ coordination sphere. c) Top-down view of the overlay with adamalysin II. The solvent molecule associated with adamalysin II is shown in grey. d) Side-on view of the overlay with adamalysin II. While the position of the His rings is close between the model and adamalysin II, the location of the solvent molecules differ noticeably. Unlike for CAII, three ϵ amino nitrogens bind to Zn(II) in adamalysin II.⁸⁶ Overlay was performed manually in PyMOL.²⁷

of these cases is not surprising as the crystal growth conditions contain 200 mM NaCl. Additionally, halides are known to bind to the metal center in CA and act as inhibitors.⁴⁷⁻

⁴⁹ There are several differences in the geometries and coordination environments of the structural sites between the two pH's. At both pH's there are two trimers in the ASU and at pH 8.5, one of these contains a trigonal HgS₃ site while the other better fits a T-shaped model. At lower pH, both trimers contain T-shaped HgS₃. Additionally, one of the thiolate ligands displays two conformations where the sulfur atom points both into the trimer and out towards the exterior (Figure 2-11). The interior Hg(II) has a two-coordinate geometry (distorted from linear) when this thiolate is pointing to the exterior. In both trimers, an exterior Hg(II) is present, in two conformations, and is bound to the thiolate that swings out in one conformation and is further away and bound only to an exterior Glu residue in the other. This apparent pH-dependence of the Hg(II) sites fits the model of Hg(II) binding previously proposed by the group based on spectroscopic solution studies, and this work provides the first structural characterization of Hg(II) binding in this family of peptides.^{38,50} According to the model, Hg(II) is bound two-coordinate at lower pH with the third sulfur-containing residue unbound. As the pH is raised, the thiol is deprotonated and Hg(II) can bind, resulting in a trigonal site. Importantly, the presence of a trigonal HgS₃ site provides the first crystallographic model for tris(cyseinato)Hg(II) complexation by the metalloregulatory protein MerR.⁵¹ The pH trend in these crystal structures fits the model, but the results indicate a more elevated pK_a than expected based on Hg(II) binding to a Cys₃ site in an a position (pK_a for Hg(II) in **TRIL9CL23H** is ~7.1). Indeed, measurement of the pK_a for Hg(II) binding to Pen in **CSL9PenL23H** and **TRIL16Pen** (as a control to ensure the difference was not due to **CS** vs **TRI**) indicates that it is > 9 (exact measurements were complicated due to unfolding at higher pH (> 10)). Given this apparent higher pK_a, I can now present structural models for the proposed mechanism of Hg(II) binding at both lower and higher pH. Furthermore, the multiple conformations of Hg(II) present at the exterior of the trimer provide structural evidence for the proposed mechanism for metal insertion into interior sites of these 3SCC's via the exterior carboxylate residues.⁵²

In addition to solid-state structural characterization, I also sought to gain an understanding of how Zn(II) binds to these peptides in solution. To measure the binding of Zn(II), UV-Vis spectroscopy with a colorimetric chelator (Zincon) was used due to the spectroscopically silent nature of this d¹⁰ metal ion. The binding of Zn(II) to several

peptide complexes was examined, including His sites and Cys sites, in order to determine the preference of Zn(II) for a given site (Table 2-8, Figures 2-12-2-14). Dissociation constants of 0.6 ± 0.1 (pH 7.5) and 0.24 ± 0.02 (pH 9.0) μM for $[\text{Zn(II)(OH}_2\text{/OH}^-)]_{\text{N}}(\text{TRIL2W23H})_3^{n+}$ and 0.8 ± 0.1 (pH 7.5) and 0.22 ± 0.06 (pH 9.0) μM for $[\text{Hg(II)}]_{\text{S}}[\text{Zn(II)(OH}_2\text{/OH}^-)]_{\text{N}}(\text{TRIL9CL23H})_3^{n+}$ are consistent with those reported for designed Zn(II)-binding sites with three protein ligands.^{8-11,53-56} There are no significant differences between these values for each peptide, demonstrating that although Hg(II) enhances the stability, this does not affect the strength of Zn(II) binding. This observation does not follow a previous report from the group in which the binding of Cd(II) to trigonal thiolate sites in **TRI** peptides exhibits a linear free energy correlation between peptide self-association and Cd(II) dissociation constants.⁵⁷ The dissociation constants for Zn(II) binding to Cys₃ sites in **TRI** peptides are ~60-fold stronger at pH 9.0 and ~10-fold weaker at pH 7.5. The weaker binding at low pH may result if the Cys residues are not all fully deprotonated to thiolates to allow for complete binding. Stronger binding to Cys₃ at high pH likely reflects a preference of Zn(II) for Cys residues in this class of designed proteins. When the Cys site is blocked by Hg(II) binding, no Zn(II) binding is observed. Similarly, little to no Zn(II) binding is observed for the peptide **TRIL2W**, which lacks a metal-binding site entirely. In both of these cases, there may be some non-specific binding to the exterior, but the data does not fit the same model used for peptides containing open metal-binding sites. The binding of Zn(II) to the crystallographic analog sequence was also explored for comparison. The K_{d} 's obtained, ~0.016 μM at pH 7.5 and 0.007 ± 0.001 μM at pH 9.0 are both ~30-40-fold stronger than for the same site in **TRI**. This is most likely due to the presence of an exterior His residue which may also bind Zn(II). The binding affinity of a corresponding Cys₃ site in **CS** is about the same as the Cys₃ sites in **TRI**, but ~20-fold stronger than that for Zn(II) binding to $[\text{Hg(II)}]_{\text{S}}[\text{Zn(II)(OH}_2\text{/OH}^-)]_{\text{N}}(\text{CSL9PenL23H})_3^{n+}$. These binding affinities are generally weaker than those for native Zn(II) enzymes, probably due to the lack of secondary coordination sphere interactions.^{42,58-61} Overall, the comparison of Zn(II) binding demonstrates that Zn(II) will bind well to either His₃ or Cys₃ sites in these peptides (as expected since Zn(II) is a borderline metal based on the hard-soft acid-base theory), with a greater affinity for the thiolate site. However, by blocking the thiol site with Hg(II),

Zn(II) binding can be driven to solely the His₃ site, therefore achieving the goal of designing a 3SCC which can discriminate between binding two different metals in spatially separated sites.

After demonstrating that I obtained an excellent structural model of CA, it was necessary to determine if this strictly first-coordination sphere structural relationship would be enough to confer catalytic activity. The α -CAs can hydrolyze esters such as *p*NPA by a similar mechanism (nucleophilic attack by Zn(II)-bound hydroxide) to the physiologically relevant CO₂ hydration reaction.^{36,62} Modeling the structure and reactivity of this metalloenzyme has been the focus of many studies, however, relatively few active model complexes that can be considered structurally true to the active site of CA have been reported for *p*NPA hydrolysis.⁶³⁻⁶⁸ Of these, there are three notable small molecule examples of N₃-type ligands reported to bind Zn(II) and facilitate the hydrolysis of *p*NPA with measurable second-order rate constants. These are the macrocyclic amine complexes [12]aneN₃ and [15]aneN₃O₂, and a tris(imidazolyl)phosphine complex. A second-order rate constant of 0.041 M⁻¹ s⁻¹ was reported for [12]aneN₃ at pH 8.2 and 25°C (pK_a = 7.3)⁶³ and of 0.6 M⁻¹ s⁻¹ for [15]aneN₃O₂, assuming 100% active hydroxide complex (pK_a = 8.8) (Table 2-10).⁶⁶ The Zn(II) complex of tris(4,5-di-*n*-propyl-2-imidazolyl)phosphine is reported to catalyze this reaction in micelles with a second order rate constant of 0.86 M⁻¹ s⁻¹, however, the corresponding estimated value under aqueous (and more comparable) conditions is only 0.0186 M⁻¹ s⁻¹.⁶⁵ There are also several relatively poor structural models, such as [12]aneN₄ with four coordinating nitrogens, which have rate constants up to 0.1 M⁻¹ s⁻¹ at pH 9.3 (pK_a = 7.9) in 10% CH₃CN⁶⁹ and up to 5.0 M⁻¹ s⁻¹ under micellar conditions (for the 1-hexadecyl derivative of [12]aneN₄).⁷⁰ Notably, these synthetic complexes, in addition to having important drawbacks such as not being able to perform in 100% aqueous solution and often dimerizing, typically suffer from product inhibition.

The two-site designed protein, [Hg(II)]_S[Zn(II)(OH₂/OH)]_N(**TRIL9CL23H**)₃ⁿ⁺, exhibits saturation kinetics for *p*NPA hydrolysis in buffered aqueous solution, with $k_{\text{cat}} = 2.2 (\pm 0.5) \times 10^{-3} \text{ s}^{-1}$ and $k_{\text{cat}}/K_{\text{M}} = 1.38 \pm 0.04 \text{ M}^{-1} \text{ s}^{-1}$ at pH 7.5 (25 °C, 10 μM catalyst, turnover number (TON) > 10, Table 2-9). Compared to the best small-molecule models (having mixed solvent systems), this designed metalloprotein is over 33-fold superior to [12]aneN₃ (pH 8.2, TON < 1 under the conditions at which this rate was measured) at its

slowest (pH 7.5) and over 550-fold at pH 9.5.⁶³ At pH 9.5, it is ~40-fold faster than the maximal rate for [15]aneN₃O₂⁶⁶ and 1250-fold faster than Brown's phosphine complex under comparable conditions.⁶⁵ Additionally, designed proteins have been reported which can catalyze this reaction using His residues. Their maximal activities (at pH 7.0) are ten-fold lower than the maximal [Hg(II)]_S[Zn(II)(OH₂/OH⁻)]_N(**TRIL9CL23H**)₃ⁿ⁺ activity at pH 9.5 (see below).^{40,71,72} The observed increase in rates and catalytic efficiencies of [Hg(II)]_S[Zn(II)(OH₂/OH⁻)]_N(**TRIL9CL23H**)₃ⁿ⁺ as a function of increasing pH suggests a change in the active site species, presumably deprotonation of the Zn(II)-aqua ligand. At pH 9.5, measured k_{cat}/K_M of up to $23.3 \pm 0.3 \text{ M}^{-1} \text{ s}^{-1}$ can be reached, while the K_M values remain essentially constant (~2 mM, within error) over the range. pH-dependency profiles of k_{cat}/K_M vs pH and k_{cat} vs pH yield similar $\text{p}K_a$'s (~9.0), indicating that the rate-limiting step is likely chemical in nature (Figures 2-15-2-17). It should be noted that since the relative k_{cat}/K_M values (both measured and maximal, Table 2-9) for [Zn(II)(OH₂/OH⁻)]_N(**TRIL2W23H**)₃ⁿ⁺ are similar/identical to those for the complex with the structural site, except possibly at high pH, the structural site enhances stability with no expense to catalytic activity. The slightly enhanced catalytic efficiency of [Hg(II)]_S[Zn(II)(OH₂/OH⁻)]_N(**TRIL9CL23H**)₃ⁿ⁺ under more basic conditions suggests the added stability conferred by Hg(II) may be important at higher pH.

Further, I evaluated product inhibition for both complexes, with and without the structural site. The products resulting from hydrolysis of *p*NPA are *p*-nitrophenol/*p*-nitrophenolate (*p*NP/*p*NP⁻) and acetate. No inhibition with either of these is observed under the conditions of the experiment (which only produces up to 1.4 mM product), demonstrating that product inhibition is not a concern during the course of these assays. This is an important benefit of this system since small molecule model complexes typically have extensive problems with product inhibition. Further analysis was undertaken using potassium acetate as it is reasonable that a smaller anion would have a better chance of binding in the designed complex (likely to Zn(II)) than *p*NP/*p*NP⁻. I found that higher concentrations of acetate (> 0.1 M) can competitively inhibit *p*NPA hydrolysis by these complexes at pH 8.5 ($0.34 \pm 0.01 \text{ M}$ for [Zn(II)(OH₂/OH⁻)]_N(**TRIL2WL23H**)₃ⁿ⁺ and $0.32 \pm 0.01 \text{ M}$ for [Hg(II)]_S[Zn(II)(OH₂/OH⁻)]_N(**TRIL9CL23H**)₃ⁿ⁺) (Table 2-11). No inhibition of the

reaction was observed at pH 9.5, consistent with the trend for CA, where less inhibition by chloride is observed with increasing pH.⁴⁷⁻⁴⁹ This is presumably due to increasing competition with hydroxide for the Zn(II) center. Again, the structural site does not appear to have a large effect on the catalytic site.

There are some designed nucleophilic catalysts which, while not meant to be CA models, do represent important designed protein catalysts for *p*NPA hydrolysis. Broo *et al.*^{71,72} reported a designed helix-loop-helix dimer, KO-42, which contains six His residues that contribute to a second-order rate constant of 0.29 M⁻¹ s⁻¹ at pH 5.1. This value can be extrapolated to ~0.7 M⁻¹ s⁻¹ at pH 7, based on the pH rate profiles reported for similarly activated esters.⁴⁰ Bolon and Mayo⁴⁰ have reported the redesign of thioredoxin to include an active site to support His-mediated nucleophilic hydrolysis of *p*NPA. At pH 7, PZD2 has a catalytic efficiency of 2.7 M⁻¹ s⁻¹. By comparison, [Hg(II)]_S[Zn(II)(OH₂/OH⁻)]_N(**TRIL9CL23H**)₃ⁿ⁺ exhibits a relatively similar catalytic efficiency at pH 7.5 (1.38 M⁻¹ s⁻¹). It is expected that in these His-catalyzed systems, the His residues are completely deprotonated by pH 7. In the metal-bound **TRI** peptide system, however, there is not a high proportion of the active species at low pH. The activity increases with increasing pH as the Zn(II)-bound water is deprotonated to form the Zn(II)-OH⁻ nucleophile. Therefore, when the activity of [Hg(II)]_S[Zn(II)(OH₂/OH⁻)]_N(**TRIL9CL23H**)₃ⁿ⁺ at its maximal measured value (pH 9.5, 23.3 M⁻¹ s⁻¹) is compared to those of the designed proteins discussed above, I find that [Hg(II)]_S[Zn(II)(OH₂/OH⁻)]_N(**TRIL9CL23H**)₃ⁿ⁺ performs this reaction with a ~10-fold enhanced catalytic efficiency.

Since this work was first published, the design of a *de novo* ZnHis₃ site the interface of two copies of the Rab4-binding domain of Rabenosyn was reported by the Kuhlman group.^{13,73} This site efficiently catalyzes both *p*NPA and *p*NPP hydrolysis. This work involved the use of computational methods to introduce a metal-binding site on the surface of a monomeric protein in order to direct the formation of a dimer (two His residues from one monomer, and two from the other to make up what was intended to be a ZnHis₄ site). The goal of the design was to use metal binding to improve the computational design of protein-protein interfaces, since metals can form stronger interactions with certain residues than simple protein-protein hydrogen bonds or van der

waals contacts. The approach is similar to that taken by the Tezcan group (Chapter 1).⁷⁴⁻
⁷⁶ When the X-ray crystal structure unexpectedly revealed a ZnHis₃ site at the interface, with tartrate filling the open coordination site, the authors tested the system for hydrolytic activity. At pH 8.5, the designed Zn(II) homodimer catalyzes the hydrolysis of *p*NPA with a rate of 0.22 s⁻¹ and $K_M = 0.47$ mM. As for [Hg(II)]_S[Zn(II)(OH₂/OH⁻)]_N (**TRIL9CL23H**)₃ⁿ⁺, the rate of hydrolysis is pH-dependent, increasing with increasing pH and MID1-Zn has a kinetic p*K*_a of 8.2 ± 0.1 and maximal efficiency of 630 ± 90 M⁻¹ s⁻¹. The authors demonstrate that mutating some of the surrounding residues to Glu results in a closed coordination sphere and corresponding loss of activity (supporting a Zn(II)-OH⁻ nucleophile-based mechanism). MID1-Zn can also effectively catalyze the hydrolysis of *p*NPP (14 M⁻¹ s⁻¹ at pH 8.5), although it is an intrinsically less reactive substrate. The authors discuss the importance of the binding cleft in achieving these efficiencies (the presence of tartrate in the crystal structure highlighted a binding pocket ~6 Å wide and 4 Å deep). Many synthetic models are relatively ineffective given that they have no binding cleft, although this can be improved somewhat in apolar solvents (and under micellar conditions) which can simulate the apolarity of an active site cleft.⁷⁷ The maximal efficiency of MID1-Zn towards *p*NPA hydrolysis is ~20-fold higher than that for [Hg(II)]_S[Zn(II)(OH₂/OH⁻)]_N(**TRIL9CL23H**)₃ⁿ⁺. One potential reason is the size of the active site; while there is room for substrate binding in [Hg(II)]_S[Zn(II)(OH₂/OH⁻)]_N (**TRIL9CL23H**)₃ⁿ⁺ (at least partial insertion through the interface between helices), it is in a hydrophobic core and not open to solvent as the interface site in MID1-Zn (Figure 2-22). If the activity of MID1-Zn towards CO₂ hydration is reported (it is not currently), then it would be interesting to determine how the CO₂ hydration rates might compare (described in Chapter 5 for [Hg(II)]_S[Zn(II)(OH₂/OH⁻)]_N(**TRIL9CL23H**)₃ⁿ⁺). As CO₂ is much smaller than *p*NPA, the size of the binding pockets may be removed as a potential source of disparity and allow for more complete evaluation of the differences between the Zn(II) sites due to the existing electrostatics of the surrounding protein matrix and solvent exposure of the metal sites.

The maximal k_{cat}/K_M for *p*NPA hydrolysis by [Hg(II)]_S[Zn(II)(OH₂/OH⁻)]_N(**TRIL9CL23H**)₃ⁿ⁺ is ~100-fold less than that of the fastest

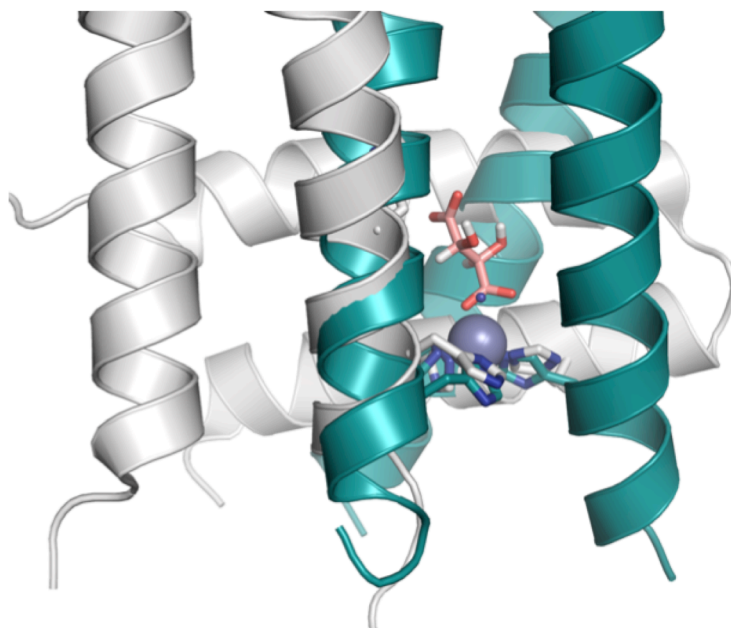


Figure 2-22. Overlay of the Zn(II)N₃O site in [Hg(II)]_s[Zn(II)(OH₂/OH⁻)]_N (CSL9PenL23H)₃ⁿ⁺ with the Zn(II)N₃X site in MID1-Zn. The crystal structure of [Hg(II)]_s[Zn(II)(OH₂/OH⁻)]_N(CSL9PenL23H)₃ⁿ⁺ is shown in cyan (pdb 3PBJ)¹², and the crystal structure of the designed dimer, MID1-Zn, in grey (pdb 3V1C).¹³ The solvent access to the active site varies between the two structures, with relatively high solvent access for the interface site in MID1-Zn over the ZnN₃O site within the hydrophobic interior of the α -helical coiled coil.

CA isozyme, CAII, at pH 8 (maximum efficiency). Furthermore, it is only ~12-fold less efficient than CAI.^{36,78} Notably, secondary interactions in CA (as in many metalloenzymes) are very important and in particular, mutation of Thr199 (which forms a hydrogen-bonding interaction with the hydroxide nucleophile of the Zn(II) center) in CAII results in a ~100-fold loss in catalytic efficiency and a 1.5-2.5 unit increase in p*K*_a from 6.8.^{79,80} These new kinetic parameters for T199A CAII would yield an enzyme possessing an efficiency within a factor of two of [Hg(II)]_s[Zn(II)(OH₂/OH⁻)]_N(TRIL9CL23H)₃ⁿ⁺ and exhibiting an essentially identical p*K*_a. Thus, the catalytic efficiency of the minimal first generation metallopeptide model presented in this chapter towards *p*NPA hydrolysis, which has yet to take into account these secondary interactions that significantly contribute to optimal activity in CA, is essentially mimicking one of the fastest known enzymes, CAII.

Conclusion

The design reported here takes advantage of the Pecoraro group's ability to generate peptides which contain adjacent metal ion sites with differing affinities, properties, and functions.^{81,82} Two spatially removed sites have been prepared within the interior of a coiled coil, in which very different coordinating ligands are presented to the metal ions. These sites differ greatly and as such it is now possible for the first time to build an artificial protein that contains both a structural and a catalytic site. Not only is this the first example of a true *de novo* designed protein containing two separate metal sites with different functions, but it is also the first hydrolytic metalloenzyme designed from scratch and competitive with one of the fastest known natural metalloenzymes, CA. Furthermore, it represents a unique synthetic model with rates higher than any previously reported nitrogenous small molecule catalytic Zn(II) complex for *p*NPA hydrolysis. An important question in protein design that is difficult, if not impossible, to address with mutagenesis studies on the natural protein in question, is what the minimal unit required for catalytic activity is. The work described in this chapter clearly indicates that an active site can be removed from a native enzyme, embedded into an entirely different and minimized protein fold, while retaining the first coordination sphere geometry and a significant amount of catalytic activity. The secondary structural features (β -sheets in CA and α -helices in the design) are apparently not critical to achieving this level of activity. However, interruption of secondary interactions such as hydrogen bonding in the native enzyme diminishes rate, catalytic efficiency, and Zn(II)-binding affinities. In fact, the designed Zn(II) active site is very competitive with CA mutants in which hydrogen-bonding interactions near the Zn(II) center are removed. This suggests that the importance of the protein structure beyond the first coordination sphere is critical for fine-tuning the active site in order to optimize binding affinity, pK_a , efficiency, rate, and likely also substrate selectivity. The versatility of the **TRI** system should allow one to readily make changes to incorporate residues capable of secondary interactions like hydrogen bonding and to study the resulting effects on both catalytic activity and pK_a . Such studies should help to determine what the minimal structure required to achieve optimal properties and top catalytic activity is. Is the whole protein matrix in the native enzyme necessary or can these optimal properties be reached in a smaller structure made

up of different structural elements? Understanding whether or not the protein matrix in native enzymes is absolutely necessary or simply a remnant of evolution will be critical for building novel *de novo* metalloenzymes. Overall, these results inspire confidence that more economically important processes may be developed within a biomolecular scaffold for future biotechnological and pharmaceutical applications.

References

- (1) Lu, Y.; Yeung, N.; Sieracki, N.; Marshall, N. M. *Nature* **2009**, *460*, 855–862.
- (2) Nanda, V.; Koder, R. L. *Nat. Chem.* **2010**, *2*, 15–24.
- (3) Kaplan, J.; DeGrado, W. F. *Proc. Natl. Acad. Sci. U.S.A.* **2004**, *101*, 11566–11570.
- (4) Faiella, M.; Andreozzi, C.; de Rosales, R. T. M.; Pavone, V.; Maglio, O.; Nastri, F.; DeGrado, W. F.; Lombardi, A. *Nat. Chem. Biol.* **2009**, *5*, 882–884.
- (5) Dieckmann, G. R.; McRorie, D. K.; Lear, J. D.; Sharp, K. A.; DeGrado, W. F.; Pecoraro, V. L. *J. Mol. Biol.* **1998**, *280*, 897–912.
- (6) Farrer, B. T.; Harris, N. P.; Balchus, K. E.; Pecoraro, V. L. *Biochemistry* **2001**, *40*, 14696–14705.
- (7) Handel, T.; DeGrado, W. F. *J. Am. Chem. Soc.* **1990**, *112*, 6710–6711.
- (8) Pessi, A.; Bianchi, E.; Cramer, A.; Venturini, S.; Tramontano, A.; Sollazzo, M. *Nature* **1993**, *362*, 367–369.
- (9) Kiyokawa, T.; Kanaori, K.; Tajima, K.; Koike, M.; Mizuno, T.; Oku, J.-I.; Tanaka, T. *J. Pept. Res.* **2004**, *63*, 347–353.
- (10) Müller, H. N.; Skerra, A. *Biochemistry* **1994**, *33*, 14126–14135.
- (11) Vita, C.; Roumestand, C.; Toma, F.; Ménez, A. *Proc. Natl. Acad. Sci. U.S.A.* **1995**, *92*, 6404–6408.
- (12) Zastrow, M. L.; Peacock, A. F. A.; Stuckey, J. A.; Pecoraro, V. L. *Nat. Chem.* **2012**, *4*, 118–123.
- (13) Der, B. S.; Edwards, D. R.; Kuhlman, B. *Biochemistry* **2012**, *51*, 3933–3940.
- (14) Farrer, B. T.; McClure, C. P.; Penner-Hahn, J. E.; Pecoraro, V. L. *Inorg. Chem.* **2000**, *39*, 5422–5423.
- (15) Matzapetakis, M.; Ghosh, D.; Weng, T.-C.; Penner-Hahn, J. E.; Pecoraro, V. L. *J. Biol. Inorg. Chem.* **2006**, *11*, 876–890.
- (16) Dieckmann, G. R.; McRorie, D. K.; Tierney, D. L.; Utschig, L. M.; Singer, C. P.; O'Halloran, T. V.; Penner-Hahn, J. E.; DeGrado, W. F.; Pecoraro, V. L. *J. Am. Chem. Soc.* **1997**, *119*, 6195–6196.
- (17) Chan, W. C.; White, P. D. *Fmoc Solid Phase Peptide Synthesis: A Practical Approach*; Chan, W. C.; White, P. D., Eds.; Oxford University Press: New York, 2000; Vol. 222.
- (18) Habeeb, A. F. *Meth. Enzymol.* **1972**, *25*, 457–464.
- (19) Riddles, P.; Blakeley, R.; Zerner, B. *Meth. Enzymol.* **1983**, *91*, 49–60.
- (20) Mantle, M.; Stewart, G.; Zayas, G.; King, M. *Biochem. J.* **1990**, *266*, 597–604.
- (21) Otwinowski, Z.; Minor, W. *Meth. Enzymol.* **1997**, *276*, 307–326.
- (22) Potterton, E.; Briggs, P.; Turkenburg, M.; Dodson, E. *Acta Crystallogr. D Biol. Crystallogr.* **2003**, *59*, 1131–1137.
- (23) McCoy, A. J.; Grosse-Kunstleve, R. W.; Adams, P. D.; Winn, M. D.; Storoni, L. C.; Read, R. J. *J. Appl. Crystallogr.* **2007**, *40*, 658–674.
- (24) Peacock, A. F. A.; Stuckey, J. A.; Pecoraro, V. L. *Angew. Chem., Int. Ed.* **2009**, *48*, 7371–7374.
- (25) Bricogne, G.; Blanc, E.; Brandl, M.; Flensburg, C.; Keller, P.; Paciorek, W.; Roversi, P.; Sharff, A.; Smart, O. S.; Vornrhein, C.; Womack, T. O. Buster version 2.8.0. **2010**, Cambridge, United Kingdom: Global Phasing Ltd.

- (26) Emsley, P.; Cowtan, K. *Acta Crystallogr. D Biol. Crystallogr.* **2004**, *60*, 2126–2132.
- (27) The PyMOL Molecular Graphics System, Version 1.5.0.4 Schrödinger, LLC.
- (28) Rush, R. M.; Yoe, J. H. *Anal. Chem.* **1954**, *26*, 1345–1347.
- (29) Sadek, F. S.; Schmid, R. W.; Reilley, C. N. *Talanta* **1959**, *2*, 38–51.
- (30) Talmard, C.; Bouzan, A.; Faller, P. *Biochemistry* **2007**, *46*, 13658–13666.
- (31) Shaw, C. F.; Laib, J. E.; Savas, M. M.; Petering, D. H. *Inorg. Chem.* **1990**, *29*, 403–408.
- (32) Mekmouche, Y.; Coppel, Y.; Hochgräfe, K.; Guilloureau, L.; Talmard, C.; Mazarguil, H.; Faller, P. *ChemBioChem* **2005**, *6*, 1663–1671.
- (33) Laib, J.; Shaw, C. F.; Petering, D. H.; Eidsness, M. K.; Elder, R. C.; Garvey, J. S. *Biochemistry* **1985**, *24*, 1977–1986.
- (34) Säbel, C. E.; Neureuther, J. M.; Siemann, S. *Anal. Biochem.* **2010**, *397*, 218–226.
- (35) GraphPad Prism version 5.00 for Mac, GraphPad Software, San Diego California USA, www.graphpad.com.
- (36) Verpoorte, J. A.; Mehta, S.; Edsall, J. T. *J. Biol. Chem.* **1967**, *242*, 4221–4229.
- (37) Marangoni, A. G. *Enzyme Kinetics; reversible enzyme inhibition*; John Wiley & Sons, Inc.: Hoboken, NJ, USA, 2002; pp. 61–69.
- (38) Pecoraro, V. L.; Peacock, A. F. A.; Iranzo, O.; Luczkowski, M. *ACS Symp. Ser.* **2009**, *1012*, 183–197.
- (39) Matzapetakis, M.; Farrer, B. T.; Weng, T.-C.; Hemmingsen, L.; Penner-Hahn, J. E.; Pecoraro, V. L. *J. Am. Chem. Soc.* **2002**, *124*, 8042–8054.
- (40) Bolon, D. N.; Mayo, S. L. *Proc. Natl. Acad. Sci. U.S.A.* **2001**, *98*, 14274–14279.
- (41) Farrer, B. T.; Pecoraro, V. L. *Proc. Natl. Acad. Sci. U.S.A.* **2003**, *100*, 3760–3765.
- (42) Christianson, D. W.; Fierke, C. A. *Acc. Chem. Res.* **1996**, *29*, 331–339.
- (43) Matzapetakis, M.; Pecoraro, V. L. *J. Am. Chem. Soc.* **2005**, *127*, 18229–18233.
- (44) Chakraborty, S.; Touw, D. S.; Peacock, A. F. A.; Stuckey, J.; Pecoraro, V. L. *J. Am. Chem. Soc.* **2010**, *132*, 13240–13250.
- (45) Zampella, G.; Neupane, K. P.; De Gioia, L.; Pecoraro, V. L. *Chem.--Eur. J.* **2012**, *18*, 2040–2050.
- (46) Touw, D. S.; Nordman, C. E.; Stuckey, J. A.; Pecoraro, V. L. *Proc. Natl. Acad. Sci. U.S.A.* **2007**, *104*, 11969–11974.
- (47) Pocker, Y.; Stone, J. T. *Biochemistry* **1968**, *7*, 2936–2945.
- (48) Pocker, Y.; Deits, T. L. *J. Am. Chem. Soc.* **1982**, *104*, 2424–2434.
- (49) Pocker, Y.; Stone, J. T. *Biochemistry* **1967**, *6*, 668–678.
- (50) Iranzo, O.; Thulstrup, P. W.; Ryu, S.-B.; Hemmingsen, L.; Pecoraro, V. L. *Chem.--Eur. J.* **2007**, *13*, 9178–9190.
- (51) Wright, J. G.; Tsang, H. T.; Penner-Hahn, J. E.; O'Halloran, T. V. *J. Am. Chem. Soc.* **1990**, *112*, 2434–2435.
- (52) Chakraborty, S.; Iranzo, O.; Zuiderweg, E. R. P.; Pecoraro, V. L. *J. Am. Chem. Soc.* **2012**, *134*, 6191–6203.
- (53) Regan, L. *Trends Biochem. Sci.* **1995**, *20*, 280–285.
- (54) Stewart, J. D.; Roberts, V. A.; Crowder, M. W.; Getzoff, E. D.; Benkovic, S. J. *J. Am. Chem. Soc.* **1994**, *116*, 415–416.
- (55) Wade, W. S.; Koh, J. S.; Han, N.; Hoekstra, D. M.; Lerner, R. A. *J. Am. Chem. Soc.* **1993**, *115*, 4449–4456.

- (56) Handel, T. T.; Williams, S. A.; DeGrado, W. F. *Science* **1993**, *261*, 879–885.
- (57) Ghosh, D.; Lee, K.-H.; Demeler, B.; Pecoraro, V. L. *Biochemistry* **2005**, *44*, 10732–10740.
- (58) Hitomi, Y.; Outten, C. E.; O’Halloran, T. V. *J. Am. Chem. Soc.* **2001**, *123*, 8614–8615.
- (59) Fierke, C. A.; Thompson, R. B. *Biometals* **2001**, *14*, 205–222.
- (60) Song, H.; Wilson, D. L.; Farquhar, E. R.; Lewis, E. A.; Emerson, J. P. *Inorg. Chem.* **2012**, *51*, 11098–11105.
- (61) Namuswe, F.; Berg, J. M. *J. Inorg. Biochem.* **2012**, *111*, 146–149.
- (62) Gould, S. M.; Tawfik, D. S. *Biochemistry* **2005**, *44*, 5444–5452.
- (63) Kimura, E.; Shiota, T.; Koike, T.; Shiro, M.; Kodama, M. *J. Am. Chem. Soc.* **1990**, *112*, 5805–5811.
- (64) Pérez Olmo, C.; Böhmerle, K.; Vahrenkamp, H. *Inorg. Chim. Acta* **2007**, *360*, 1510–1516.
- (65) Koerner, T. B.; Brown, R. S. *Can. J. Chem.* **2002**, *80*, 183–191.
- (66) Bazzicalupi, C.; Bencini, A.; Bianchi, A.; Fusi, V.; Giorgi, C.; Paoletti, P.; Valtancoli, B.; Zanchi, D. *Inorg. Chem.* **1997**, *36*, 2784–2790.
- (67) Sprigings, T. G.; Hall, C. D. *J. Chem. Soc. Perkin Trans. II* **2001**, 2063–2067.
- (68) Jairam, R.; Potvin, P. G.; Balsky, S. *J. Chem. Soc. Perkin Trans. II* **1999**, 363–368.
- (69) Koike, T.; Takamura, M.; Kimura, E. *J. Am. Chem. Soc.* **1994**, *116*, 8443–8449.
- (70) Kimura, E.; Hashimoto, H.; Koike, T. *J. Am. Chem. Soc.* **1996**, *118*, 10963–10970.
- (71) Broo, K. S.; Brive, L.; Ahlberg, P.; Baltzer, L. *J. Am. Chem. Soc.* **1997**, *119*, 11362–11372.
- (72) Nilsson, J.; Baltzer, L. *Chem.--Eur. J.* **2000**, *6*, 2214–2220.
- (73) Der, B. S.; Machius, M.; Miley, M. J.; Mills, J. L.; Szyperski, T.; Kuhlman, B. *J. Am. Chem. Soc.* **2012**, *134*, 375–385.
- (74) Salgado, E. N.; Radford, R. J.; Tezcan, F. A. *Acc. Chem. Res.* **2010**, *43*, 661–672.
- (75) Radford, R. J.; Brodin, J. D.; Salgado, E. N.; Tezcan, F. A. *Coord. Chem. Rev.* **2011**, *255*, 790–803.
- (76) Salgado, E. N.; Faraone-Mennella, J.; Tezcan, F. A. *J. Am. Chem. Soc.* **2007**, *129*, 13374–13375.
- (77) Gomez-Tagle, P.; Vargas-Zúñiga, I.; Taran, O.; Yatsimirsky, A. K. *J. Org. Chem.* **2006**, *71*, 9713–9722.
- (78) Innocenti, A.; Scozzafava, A.; Parkkila, S.; Puccetti, L.; De Simone, G.; Supuran, C. T. *Bioorg. Med. Chem. Lett.* **2008**, *18*, 2267–2271.
- (79) Liang, Z.; Xue, Y.; Behravan, G.; Jonsson, B. H.; Lindskog, S. *Eur. J. Biochem.* **1993**, *211*, 821–827.
- (80) Krebs, J. F.; Ippolito, J. A.; Christianson, D. W.; Fierke, C. A. *J. Biol. Chem.* **1993**, *268*, 27458–27466.
- (81) Iranzo, O.; Cabello, C.; Pecoraro, V. L. *Angew. Chem., Int. Ed.* **2007**, *46*, 6688–6691.
- (82) Peacock, A. F. A.; Hemmingsen, L.; Pecoraro, V. L. *Proc. Natl. Acad. Sci. U.S.A.* **2008**, *105*, 16566–16571.
- (83) Kleywegt, G. J.; Harris, M. R.; Zou, J. Y.; Taylor, T. C.; Wählby, A.; Jones, T. A. *Acta Crystallogr. D Biol. Crystallogr.* **2004**, *60*, 2240–2249.
- (84) Holm, R. H.; Kennepohl, P.; Solomon, E. I. *Chem. Rev.* **1996**, *96*, 2239–2314.

- (85) Marangoni, A. G. *Enzyme Kinetics*; John Wiley & Sons, Inc.: Hoboken, NJ, USA, 2002; pp. 102–115.
- (86) Gomis-Rüth, F. X.; Kress, L. F.; Bode, W. *EMBO J.* **1993**, *12*, 4151–4157.

Chapter III. Evaluating the influence of location on catalysis and metal-binding affinity in a *de novo* designed metalloprotein

Introduction

Although there are many examples of *de novo* designed metal sites¹⁻⁵ (some catalytically active), no study thoroughly examines protein matrix effects on the primary metal site. The question of whether the specific location of a metal site along the primary sequence matters, while important, has not been addressed. Insights into how the placement of an active site in differing environments around a protein affects active site properties (rate, substrate access, binding affinity) should greatly assist design efforts. Understanding these effects is important for deciding whether the location of a metal site matters for the properties one is interested in optimizing in a given system and, if so, where to engineer the desired activity within a protein.

In Chapter 2, I described the structure and hydrolytic activity of $[\text{Hg(II)}]_{\text{S}}[\text{Zn(II)(OH}_2/\text{OH)}]_{\text{N}}(\text{TRIL9CL23H})_3^{n+}$ towards *p*-nitrophenyl acetate (*p*NPA, $23.3 \text{ M}^{-1} \text{ s}^{-1}$ at pH 9.5).⁶ As described in Chapter 1, other *de novo* designed Zn(II)His₃ proteins have been reported^{1,6-11}, but few with structures and catalytic activities.^{6,7} $[\text{Hg(II)}]_{\text{S}}[\text{Zn(II)(OH}_2/\text{OH)}]_{\text{N}}(\text{TRIL9CL23H})_3^{n+}$ is only ~100-fold less efficient towards *p*NPA hydrolysis than the fastest carbonic anhydrase (CA)¹². Its efficiency is even more competitive with mutant CA's, where important secondary interactions such as hydrogen bonding to the coordinated solvent molecule of the active site Zn(II) have been removed (this T199A mutant suffers from a loss of ~100-fold catalytic efficiency for both *p*NPA hydrolysis and CO₂ hydration^{13,14}). Given that these interactions are not currently included in this well-defined minimal model, the most important next step is to begin incorporating hydrogen-bonding networks with the goal of improving reactivity. However, the design of hydrogen-bonding channels could be strongly dependent on location of the metal site in the three-stranded coiled coil (3SCC) and factors such as

solvent and substrate access and metal-binding affinities. The effects of changing the location to accommodate such a channel in an α -helical system on the catalytic efficiency are not known. The aim of this chapter is to address how catalytic efficiency may be affected when moving the active site to different locations to control rate, substrate access, and binding affinity, depending on the desired secondary interactions.

Table 3-1. TRI and Grand peptide family sequences used in these studies.

Peptide	a	b	c	d	e	f	g
TRIL2W	Ac-G	W KALEEK	LKALEEK	LKALEEK	LKALEEK	LKALEEK	G-NH ₂
TRIL2WL23H	Ac-G	W KALEEK	LKALEEK	LKALEEK	LKALEEK	H KALEEK	G-NH ₂
TRIL9CL23H	Ac-G	LKALEEK	C KALEEK	LKALEEK	LKALEEK	H KALEEK	G-NH ₂
TRIL9HL23C	Ac-G	LKALEEK	H KALEEK	LKALEEK	LKALEEK	C KALEEK	G-NH ₂
TRIL9CL19H	Ac-G	LKALEEK	C KALEEK	LKA H EEK	LKALEEK	LKALEEK	G-NH ₂
GRL2WL16C	Ac-G	W KALEEK	LKALEEK	C KALEEK	LKALEEK	LKALEEK	H KALEEK
L30H							

N- and C-termini are capped by Ac and NH₂ groups (acetylated and amidated), respectively.

The general sequences for the peptides used in the present work (Table 3-1) retain the Hg(II)-bound tris-thiolate site and the Zn(II)(His)₃(Solvent) site while altering the structures in a systematic way. The Pecoraro group has previously reported that there are differences in selectivity for heavy metal binding to thiols in **a** versus **d** sites in each heptad¹⁵⁻¹⁷, and also demonstrated how the position of a metal site along the sequence of a peptide that folds into a 3SCC can define the physical properties of Cd(II) binding.¹⁸ One might imagine that factors such as catalyst proximity to the frayed ends of the helix, orientation of the active site with respect to the helical dipole, or the location near the center versus the end of the coiled coil might influence catalytic efficiency, rate, substrate access, and/or binding affinity in these systems. In addition, the incorporation of the metal site into a more stable sequence (related but lengthened by one heptad repeat), could influence the kinetic parameters or metal binding by impacting the breathing motions/fraying of the coiled coil. A major benefit of the **TRI** peptide architecture is that it is very straightforward to move the metal site along the primary sequence in order to interrogate the chemistry in alternative positions. There is one example of a redesigned system in which a mononuclear non-heme iron site was incorporated into six different positions of thioredoxin (within three different types of surface locations: groove, shallow pocket, and deep pocket) for superoxide dismutase function.¹⁹ That study demonstrated

that one could see significant functional differences in the metal center without “prior adaptations” for the protein structure. Another example in which the site location was varied, this time for a structural Zn(II) site in order to examine the effects on binding affinity and structural stability, is the redesign of thioredoxin to incorporate a ZnHis₂Cys₂ site (Chapter 1).²⁰ In this case, variation of the site location resulted in identification of a correlation between how well the designed protein folded and the strength of Zn(II) binding. Another example of incorporating a structural ZnHis₂Cys₂ site into various locations of a protein (*de novo* designed DS119, a small protein with βαβ-type structure) demonstrated that placing the Zn(II)-binding ligands in the hydrophobic core generally resulted in an unfolded structure, even in the presence of Zn(II), while sites in the loop regions or at flexible terminals demonstrated significant Zn(II) binding ($K_d \sim 2\text{-}20 \mu\text{M}$).¹⁰ Since systematic variation of a catalytic center has never been examined within a helical (or any *de novo* designed) structure this allows one, for the first time, to be able to address how orientation and distance relative to the helical dipole and frayed termini matter, specifically with respect to metal-binding affinities, catalytic activity, and kinetic pK_a 's. The results will have significant implications for the selection of active site location in future *de novo* design studies, particularly since, to date, the majority of systems incorporate metal sites into α-helical scaffolds.

Materials and Methods

The nomenclature used to describe the metal complexes prepared in these studies is as described in Chapter 2.

Peptide Synthesis and Purification. Peptides were synthesized on an Applied Biosystems 433A peptide synthesizer using standard protocols²¹ and purified as described previously²² (by reverse-phase HPLC on a C18 column at a flow rate of 10 mL/min using a linear gradient varying from 0.1% TFA in water to 0.1% TFA in 9:1 CH₃CN:H₂O over 25-35 minutes). Pure peptides were characterized by electrospray mass spectrometry. Peptide stock solutions were prepared in doubly distilled water that had been purged with argon to minimize oxidation of thiol-containing peptides. The concentrations for **TRI**

peptides containing Cys sites were determined by calculating the thiol concentration using a published assay with 5,5'-dithiobis-(2-nitrobenzoic acid) (Ellman's reagent).^{23,24} The concentrations for **Grand** peptides (one heptad repeat longer) containing Cys sites were similarly determined using a published assay with 4,4'-dipyridyl disulphide²⁵ or were based on the tryptophan absorbance at 280 nm using $\epsilon = 5500 \text{ M}^{-1} \text{ cm}^{-1}$. Concentrations of **TRIL2WL23H** solutions were based on the tryptophan absorbance at 280 nm using $\epsilon = 5500 \text{ M}^{-1} \text{ cm}^{-1}$.

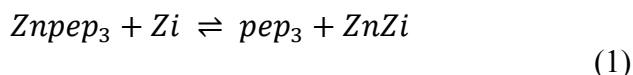
Circular Dichroism (CD) and Ultraviolet-Visible (UV-Vis) Spectroscopy. CD and UV-Vis spectra were recorded in quartz cuvettes at 25 °C on an AVIV 62DS spectrometer and Cary 100 Bio UV/Vis spectrometer, respectively. Guanidine hydrochloride (GuHCl) CD titrations were performed at pH 8.5 as described previously.²⁶ All solutions were purged with argon prior to use in order to minimize oxidation of peptides and formation of disulfide bonds.

Hg(II)-binding titrations. Hg(II) into peptide titrations were performed at room temperature and monitored by UV-Vis spectroscopy in a 1-cm quartz cuvette. Aliquots of a HgCl₂ stock solution (2-2.5 mM, standardized using inductively coupled plasma-optical emission spectroscopy) were added to a 2.5 mL solution containing 30 μM peptide (monomer) and 50 mM CHES (with 0.1 M Na₂SO₄) at pH 8.5. For all titrations, the difference spectra were obtained by subtracting the background spectrum of the peptide under identical conditions but in the absence of metal.

Competitive Zn(II)-Binding Titrations. The apparent binding constants were determined by competition assay with the colorimetric Zn(II) chelator, Zincon (2-carboxy-2'-hydroxy-5'-(sulfoformazyl)benzene).^{27,28} Zn(II) forms a 1:1 complex with Zincon (Zi) with a distinct absorption band at 620 nm ($\epsilon \sim 16000 \text{ M}^{-1} \text{ cm}^{-1}$) at pH 7.5 and apparent dissociation constant ($K_{d,app}$) of $2.80 \times 10^{-6} \text{ M}$ (consistent with the range of reported values).^{27,29-33} These parameters were evaluated for each pH and each buffer used in my experiments (pH 7.5 in 50 mM HEPES, 0.1 M Na₂SO₄ and pH 9.0 in 50 mM CHES, 0.1 M Na₂SO₄) by titrating Zn(II) (stock solutions were standardized using

inductively coupled plasma-optical emission spectroscopy) into a solution of 10 μM Zi. For pH 9.0, $\epsilon_{620} \sim 27500 \text{ M}^{-1} \text{ cm}^{-1}$ and $K_{d,\text{app}} = 5 \times 10^{-8} \text{ M}$ (a 5 cm pathlength cell was used for the calibration titration at this pH). For experiments involving peptide, an excess of Zi over ZnSO_4 (10 μM Zi and 5 μM Zn(II) to ensure most Zn(II) is bound to ligand) was used as the starting point of the titration. Analogously, Zn(II) was bound to an excess of peptide (20 μM pep₃ and 10 μM Zn(II)) for the reverse titration (in the case for $[\text{Hg(II)}]_s(\text{TRIL9HL23C})_3^-$, 5 μM Zi/2.5 μM Zn(II) and 30 μM pep₃/15 μM Zn(II) were used for the forward and reverse titrations, respectively, because this peptide had a weaker $K_{d,\text{app}}$ compared to the others). Both approaches should give similar apparent binding constants for Znpep₃, testing whether equilibrium had been reached.

The binding equilibrium for this competition experiment can be expressed by eq 1.



The apparent dissociation constant of Znpep₃ can be calculated using eq 2.

$$\frac{K_{d,\text{znpep}_3}}{K_{d,\text{znzi}}} = \frac{([\text{ZnZi}][\text{pep}_3])}{([\text{Znpep}_3][\text{Zi}]} \quad (2)$$

For the forward titration, where a solution of Zi is titrated into Znpep₃, the absorption band at 620 nm is due to the ZnZi complex, and increases as Zi is added to Znpep₃, reflecting transfer of Zn(II) from pep₃ to Zi and therefore yielding [ZnZi] and [Znpep₃] for eq 2. [Znpep₃] can be defined as the total amount of Zn(II) present ($[\text{Zn}]_T$) minus the Zn(II)-bound fraction ($[\text{ZnZi}]$), under the conditions of this experiment. The amount of unbound peptide can then be defined as the total peptide minus the Zn(II)-bound fraction, $[\text{pep}_3] = [\text{pep}_3]_T - [\text{Znpep}_3] = [\text{pep}_3]_T - ([\text{Zn}]_T - [\text{ZnZi}])$. The amount of free Zi is then related to the total amount of Zi minus the Zn(II)-bound fraction, $[\text{Zi}] = [\text{Zi}]_T - [\text{ZnZi}]$. Substituting all of the above into eq 2 yields a quadratic expression, eq 3, which can be solved for [ZnZi]. Since this quantity is directly related to the absorbance at 620 nm by the Beer-Lambert law, the real solution to eq 3 can be inserted into eq 4 to give an equation which can be fitted in Prism 5 (GraphPad Software)³⁴ to yield the dissociation constant for Znpep₃.

$$\begin{aligned} & \left(\frac{K_{d,Znpep3}}{K_{d,ZnZi}} - 1 \right) [ZnZi]^2 \\ & + \left(-\frac{K_{d,Znpep3}}{K_{d,ZnZi}} x - \frac{K_{d,Znpep3}}{K_{d,ZnZi}} [Zn]_T - [pep_3]_T + [Zn]_T \right) [ZnZi] + \frac{K_{d,Znpep3}}{K_{d,ZnZi}} [Zn]_T x \\ & = 0 \end{aligned} \tag{3}$$

$$A_{620} = y = \varepsilon * b * [ZnZi] \tag{4}$$

An analogous approach was used for the reverse titration, in which pep₃ is added to ZnZi.

Esterase Activity Assays. The esterase activities of Zn(II)-bound peptides were determined spectrophotometrically with *p*NPA as substrate (200-1400 mM) at 25°C. Measurements were made at 348 nm, the isosbestic point for *p*-nitrophenol and *p*-nitrophenolate anion ($\varepsilon = 5000 \text{ M}^{-1} \text{ cm}^{-1}$).³⁵ The procedure is similar to that which was previously described⁶ in Chapter 2, with some modifications. The substrate solution was prepared by quickly diluting a 0.1 M *p*NPA in acetone solution into doubly-distilled water (ddH₂O) to a concentration of 3 mM. The procedure for measuring esterase activity is as follows: in a 1 mm pathlength quartz cuvette, buffer (50 mM, HEPES if pH 7.5 or 8.0, CHES for pH 8.5-9.65, both buffers with 0.1 M Na₂SO₄), ddH₂O, and metal-peptide solution were mixed. *p*NPA was added, mixed, and the absorbance increase recorded every 25 seconds for 7-20 minutes. Metal-peptide solutions contained either excess peptide or excess ZnSO₄ in order to ensure all Zn(II) was bound to the peptide. Controls then contained either apo-peptide or ZnSO₄, respectively, and their initial rates were subtracted from those of Zn(II)-bound peptide samples. The controls containing ZnSO₄ do not exhibit any activity over blank controls, but there is some activity from the free peptide, due to unbound His residues.⁶ Initial rates determined from linear fits of the first 2-10% of the reaction were plotted as a function of *p*NPA concentration and fitted to the Michaelis-Menten equation in Prism 5 (GraphPad Software).³⁴ The concentration of enzyme is 20 μM and is accounted for in all reported values.

Acetate Inhibition Assays. Inhibition experiments were performed under the same buffer conditions and with the same general procedure as above. Potassium acetate

(KOAc) stock solutions (~7-10 M) were prepared by dissolving KOAc in a small amount of water, adjusting pH to 8.5 with glacial acetic acid (and vigorous stirring), followed by dilution to the final volume with ddH₂O. The acetate concentration is determined by combining the concentration from the amount of solid and from the acetic acid added. For running the assays, buffer, ddH₂O, KOAc, and enzyme were mixed together, then *p*NPA added and the absorbance monitored as above. Metal-peptide solutions were either 20 or 50 μ M Znpep₃ with 4x excess ZnSO₄ present. Controls contained all components except peptide and the difference between initial rates was taken. Initial rates were plotted and fitted as described above. For each peptide, at least three different concentrations of KOAc were tested, and plots of initial rates vs [*p*NPA] were prepared and fitted to competitive, non-competitive, and mixed inhibition equations in Prism 5 (GraphPad Software).³⁴ The individual kinetic parameters for each concentration of acetate were examined in order to estimate the applicable inhibition model (all peptides had increasing K_M and decreasing k_{cat} values as a function of increasing substrate concentration supporting a competitive inhibition model).³⁶ Lineweaver-Burke plots, in addition to examination of the α value from a mixed model fit for each complex, were also used to conclude that the inhibition observed was competitive for all peptide complexes containing a ZnHis₃ site (Lineweaver-Burke plots intersect on the y-axis and $\alpha > 1$). The α value determines the degree to which inhibitor binding changes the enzyme's affinity for substrate. If $\alpha > 1$ (and especially if it is very large), then inhibitor binding prevents substrate binding and the mixed model represents competitive inhibition.³⁶

Results

Characterization of Structural and Catalytic Sites

a) Hg(II) Binding. The binding of Hg(II) to TRIL9HL23C was measured by UV-Vis spectroscopy in which aliquots of HgCl₂ were added to a solution of 10 μ M (TRIL9HL23C)₃³⁻ in 50 mM CHES buffer (with 0.1 M Na₂SO₄) at pH 8.5. As the HgS₃ complex was formed, an increase in absorbance at 247 nm (maximum at one equivalent per trimer) with shoulders at 265 and 295 nm was observed (Figure 3-1). According to

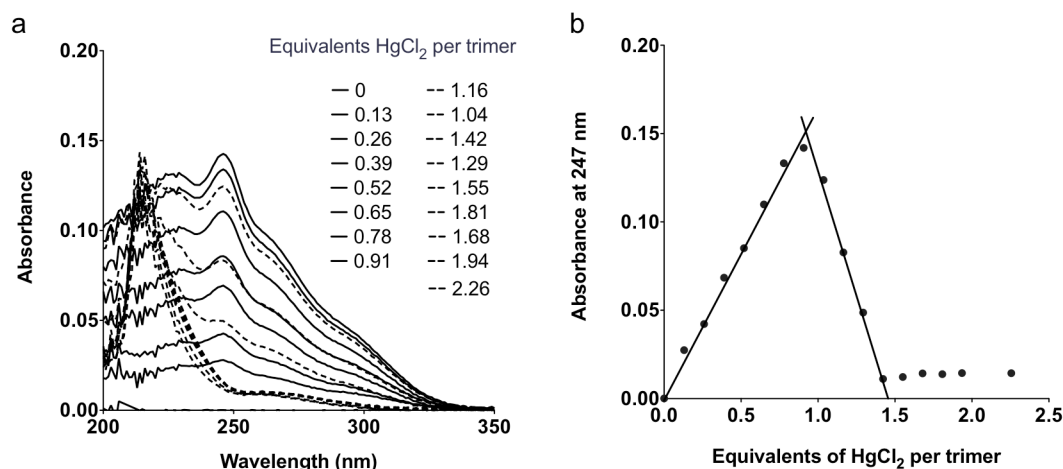


Figure 3-1. UV-Vis titration of HgCl₂ to a solution containing 30 μM TRIL9HL23C in 50 mM CHES buffer (0.1 M Na₂SO₄) at pH 8.5. a) A plot of absorbance difference spectra vs wavelength. b) A plot of the absorbance at 247 nm (characteristic of HgS₃) as a function of equivalents of HgCl₂ per trimer to show that maximal absorbance occurs at one equivalent of Hg(II) per trimer.

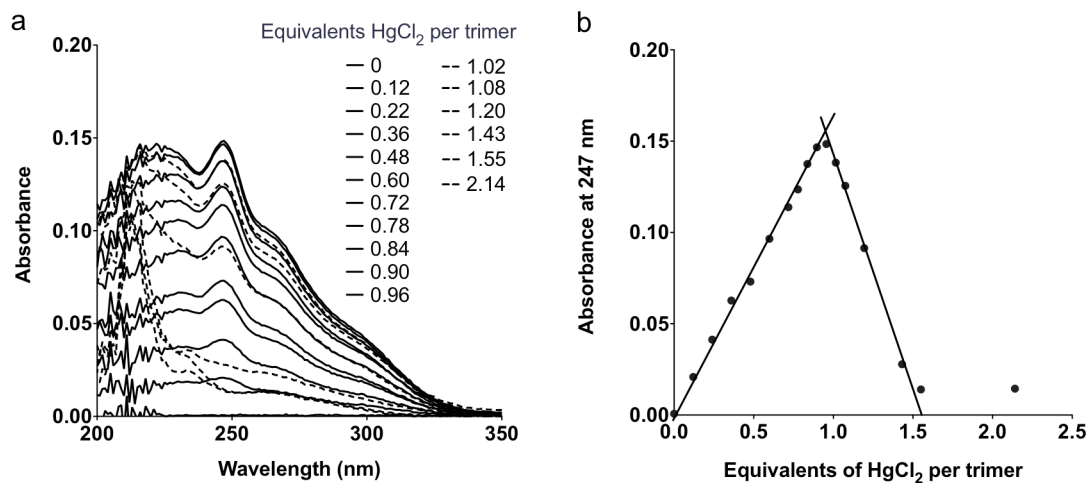


Figure 3-2. UV-Vis titration of HgCl₂ to a solution containing 30 μM TRIL9CL19H in 50 mM CHES buffer (0.1 M Na₂SO₄) at pH 8.5. a) A plot of absorbance difference spectra vs wavelength. b) A plot of the absorbance at 247 nm (characteristic of HgS₃) as a function of equivalents of HgCl₂ per trimer to show that maximal absorbance occurs at one equivalent of Hg(II) per trimer.

previous work in the group, these spectral features are characteristic of a three-coordinate HgS₃ complex.^{16,37} Following the same procedure, similar results were obtained for Hg(II) binding to TRIL9CL19H (Figure 3-2).

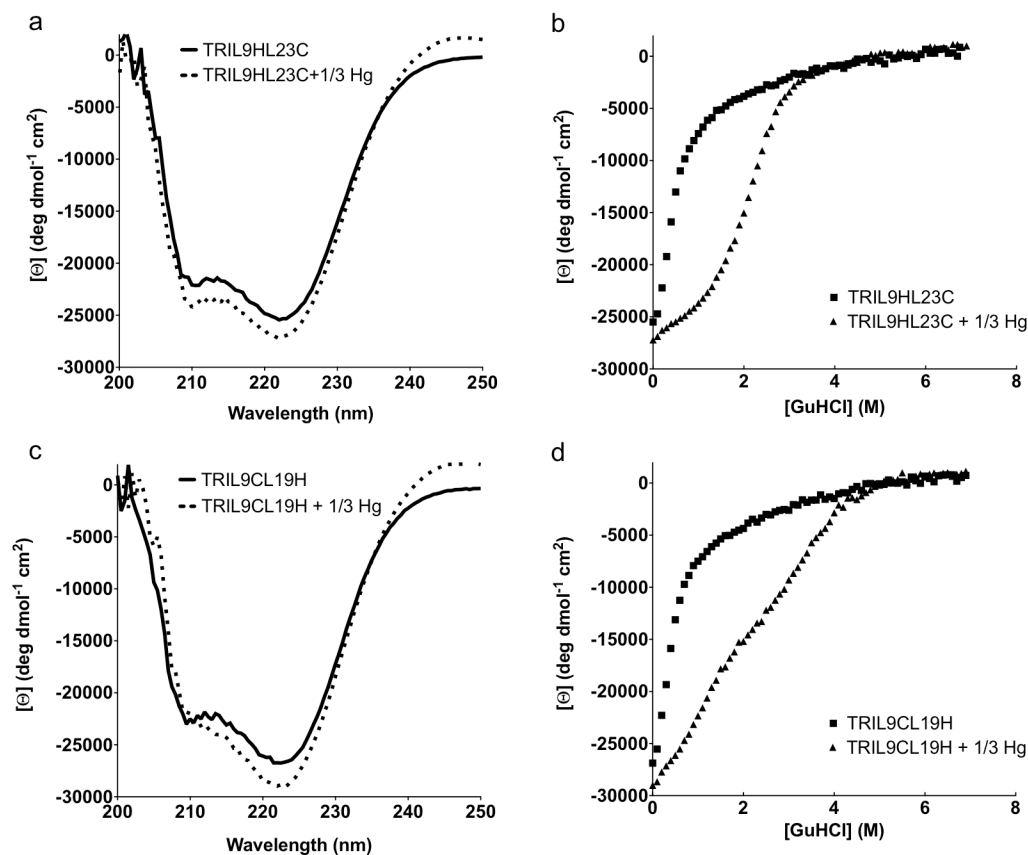


Figure 3-3. Folding of TRIL9HL23C (apo and + 1/3 Hg(II)) and TRIL9CL19H (apo and + 1/3 Hg(II)) as monitored by CD. a) CD spectra of TRIL9HL23C and TRIL9HL23C + 1/3 Hg(II) at pH 8.5 and 25 °C. The molar ellipticities $[\Theta]$ at 222 nm are ~ -25500 and ~ -27200 deg $\text{dmol}^{-1} \text{cm}^2$, respectively. b) GuHCl denaturation titrations represented by $[\Theta]$ at 222 nm vs denaturant concentration for TRIL9HL23C and TRIL9HL23C + 1/3 Hg(II). c) CD spectra of TRIL9CL19H and TRIL9CL19H + 1/3 Hg(II) at pH 8.5 and 25 °C. The $[\Theta]$ values at 222 nm are ~ -26900 and ~ -29000 deg $\text{dmol}^{-1} \text{cm}^2$, respectively. d) GuHCl denaturation titrations represented by $[\Theta]$ at 222 nm vs denaturant concentration for TRIL9CL19H and TRIL9CL19H + 1/3 Hg(II). As for the previously reported His-containing TRI peptides, I have not reported a quantitative determination of free energy values because the denaturation curves for these peptides do not level off at zero concentration of denaturant.⁶

b) Circular Dichroism (CD) of Apo- and Metal-Bound Peptides. To measure whether the presence of this HgS_3 site confers thermodynamic stability on the 3SCC's formed by the sequences **TRIL9HL23C** and **TRIL9CL19H**, as for **TRIL9CL23H**,

GuHCl denaturation titrations were monitored using CD spectroscopy (Figure 3-3). Specifically, the folding of each trimer in the presence and absence of one equivalent of Hg(II) per trimer was measured. Characteristic α -helical coiled coil peaks with negative minima at 208 and 222 nm are present in the CD spectra. The apo-peptides (**TRIL9HL23C**)₃ⁿ⁻ and (**TRIL9CL19H**)₃ⁿ⁻ have CD spectra characteristic of well-folded α -helical coiled coils at pH 8.5 with molar ellipticity values $[\Theta]$ obtained at 222 nm of ~ -25500 deg dmol⁻¹ cm² and ~ -26900 deg dmol⁻¹ cm², respectively. Similarly, for the

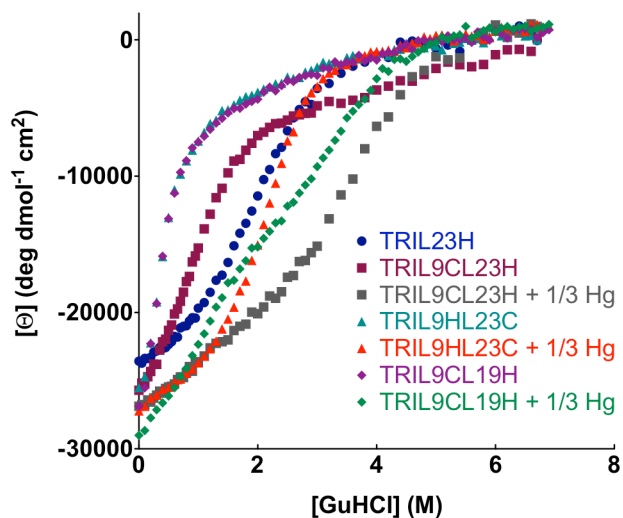


Figure 3-4. Comparison of the unfolding of TRIL9HL23C (apo and + 1/3 Hg(II)) and TRIL9CL19H (apo and + 1/3 Hg(II)) to TRIL23H and TRIL9CL23H (apo and + 1/3 Hg(II)). GuHCl denaturation titrations at pH 8.5 represented by $[\Theta]$ at 222 nm vs denaturant concentration for TRIL23H, TRIL9CL23H, TRIL9HL23C, and TRIL9CL19H. For each of the Cys-containing peptides, when comparing the apo versions and the Hg(II)-bound peptides, the midpoint is shifted to a higher denaturant concentration, demonstrating that the structural site confers stability on each of the constructs.

Hg(II)-bound trimers, $[\text{Hg(II)}_s](\text{TRIL9HL23C})_3^-$ and $[\text{Hg(II)}_s](\text{TRIL9CL19H})_3^-$, CD spectra indicate well-folded structures at pH 8.5 with $[\Theta]$ values obtained at 222 nm of ~ -27200 deg dmol⁻¹ cm² and ~ -29000 deg dmol⁻¹ cm², respectively. As reported for (**TRIL9CL23H**)₃ⁿ⁻, the addition of Hg(II) to the Cys₃ site further stabilizes both (**TRIL9HL23C**)₃ⁿ⁻ and (**TRIL9CL19H**)₃ⁿ⁻ (Figure 3-4). GuHCl denaturation titrations were also performed for (**GRL2WL16CL30H**)₃ⁿ⁻ and $[\text{Hg(II)}_s](\text{GRL2WL16CL30H})_3^-$ (Figure 3-5). The $[\Theta]$ values at zero concentration of denaturant are ~ -29700 deg dmol⁻¹

cm^2 and $\sim -30000 \text{ deg dmol}^{-1} \text{ cm}^2$, respectively. Analysis of the unfolding curves confirms that the midpoint is shifted to a higher concentration of denaturant, demonstrating Hg(II)-assisted structural stabilization, as observed for all **TRI** peptides I have described thus far (Figure 3-6).

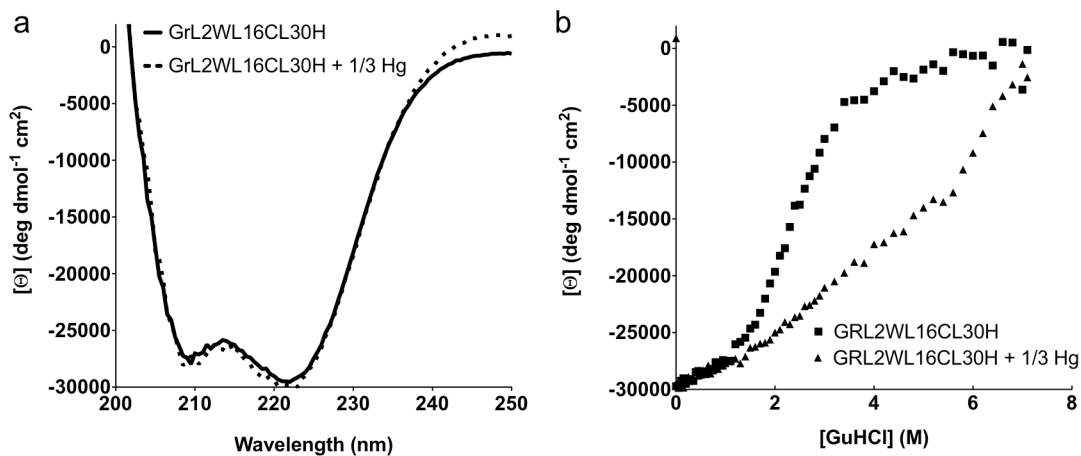


Figure 3-5. Folding of GRL2WL16CL30H (apo and + 1/3 Hg(II)) as monitored by CD. a) CD spectra of GRL2WL16CL30H and GRL2WL16CL30H + 1/3 Hg(II) at pH 8.5 and 25 °C. The $[\Theta]$ values at 222 nm are ~ -29700 and $\sim -30000 \text{ deg dmol}^{-1} \text{ cm}^2$, respectively. b) GuHCl denaturation titrations represented by the $[\Theta]$ values at 222 nm vs denaturant concentration for GRL2WL16CL30H and GRL2WL16CL30H + 1/3 Hg(II).

c) Zn(II) Binding to His₃ Sites. The colorimetric chelator Zincon was used in competitive binding titrations to measure the apparent binding affinities of Zn(II) to $[\text{Hg(II)}]_S(\text{TRIL9HL23C})_3^-$, $[\text{Hg(II)}]_S(\text{TRIL9CL19H})_3^-$, and $[\text{Hg(II)}]_S(\text{GRL2WL16CL30H})_3^-$, all of which represent potential His₃ binding sites. The binding affinities were measured for pH 7.5 and 9.0 and apparent dissociation constants resulting from fits of the data (as described in Materials and Methods) are reported in Table 3-2, along with comparisons to data from Chapter 2. Representative plots of fitted data are shown for each peptide, $[\text{Hg(II)}]_S(\text{TRIL9HL23C})_3^-$, $[\text{Hg(II)}]_S(\text{TRIL9CL19H})_3^-$, and $[\text{Hg(II)}]_S(\text{GRL2WL16CL30H})_3^-$, at pH 7.5 and 9.0 (Figures 3-7-3-8). For all three peptide complexes, Zn(II) binding was weaker at pH 7.5 but with dissociation constants in the low micromolar range ($\sim 8 \mu\text{M}$ for $[\text{Hg(II)}]_S(\text{TRIL9HL23C})_3^-$, $3.7 \pm 1.3 \mu\text{M}$ for $[\text{Hg(II)}]_S(\text{TRIL9CL19H})_3^-$, and $0.4 \pm 0.1 \mu\text{M}$ for $[\text{Hg(II)}]_S(\text{GRL2WL16CL30H})_3^-$). The

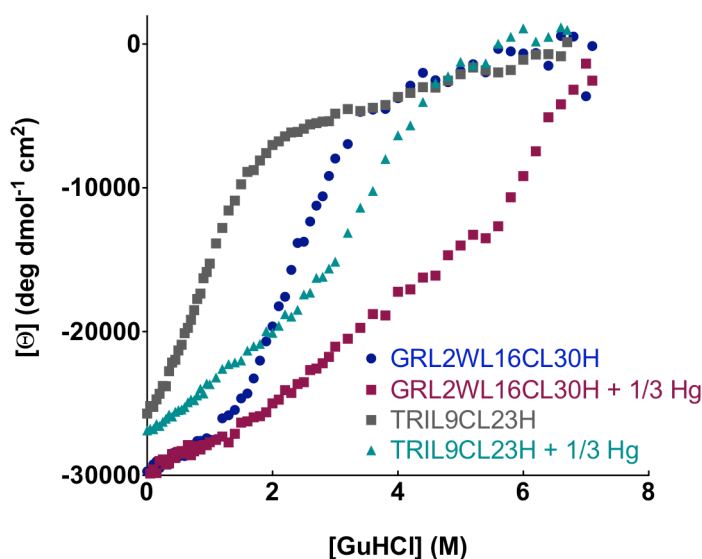


Figure 3-6. Comparison of the unfolding of GRL2WL16CL30H (apo and + 1/3 Hg(II)) to TRIL9CL23H (apo and + 1/3 Hg(II))⁶. GuHCl denaturation titrations at pH 8.5 represented by $[\Theta]$ at 222 nm vs denaturant concentration for GRL2WL16CL30H and TRIL9CL23H. For each peptide, when comparing the apo version and the Hg(II)-bound peptide, the midpoint is shifted to a higher denaturant concentration, demonstrating that the structural site confers stability on each of the constructs. Both of the Grand peptides (apo and + 1/3 Hg(II)) have increased stabilities relative to TRI peptides (apo and + 1/3 Hg(II), respectively).

Table 3-2. Apparent dissociation constants for Zn(II) binding to His₃ sites in the TRI and Grand peptides.^a

Peptide complex	$K_{d,app}$ (μ M) at pH 7.5	$K_{d,app}$ (μ M) at pH 9.0
$[\text{Zn}(\text{II})(\text{OH}_2/\text{OH}^-)]_N(\text{TRIL2WL23H})_3^{n+}$	0.6 ± 0.1	0.24 ± 0.02
$[\text{Hg}(\text{II})]_S[\text{Zn}(\text{II})(\text{OH}_2/\text{OH}^-)]_N(\text{TRIL9CL23H})_3^{n+}$	0.8 ± 0.1	0.22 ± 0.06
$[\text{Zn}(\text{II})(\text{OH}_2/\text{OH}^-)]_N[\text{Hg}(\text{II})]_S(\text{TRIL9HL23C})_3^{n+}$	~ 8	0.8 ± 0.3
$[\text{Hg}(\text{II})]_S[\text{Zn}(\text{II})(\text{OH}_2/\text{OH}^-)]_N(\text{TRIL9CL19H})_3^{n+}$	3.7 ± 1.3	0.4 ± 0.2
$[\text{Hg}(\text{II})]_S[\text{Zn}(\text{II})(\text{OH}_2/\text{OH}^-)]_N(\text{GRL2WL16CL30H})_3^{n+}$	0.4 ± 0.1	0.11 ± 0.05

a. pH 7.5 measured in 50 mM HEPES buffer, 0.1 M Na₂SO₄; pH 9.0 measured in 50 mM CHES buffer, 0.1 M Na₂SO₄.

two TRI peptides vary by about two-fold while the Grand peptide binds Zn(II) ten-fold stronger than $[\text{Hg}(\text{II})]_S(\text{TRIL9CL19H})_3^-$. The Grand peptide binds Zn(II) about two-fold stronger than the original model, $[\text{Hg}(\text{II})]_S(\text{TRIL9CL23H})_3^-$ (Chapter 2, Table 3-2). At pH 9.0, the dissociation constants for Zn(II) binding to both $[\text{Hg}(\text{II})]_S(\text{TRIL9HL23C})_3^-$ and $[\text{Hg}(\text{II})]_S(\text{TRIL9CL19H})_3^-$ are ten-fold stronger than at pH 7.5. The binding of

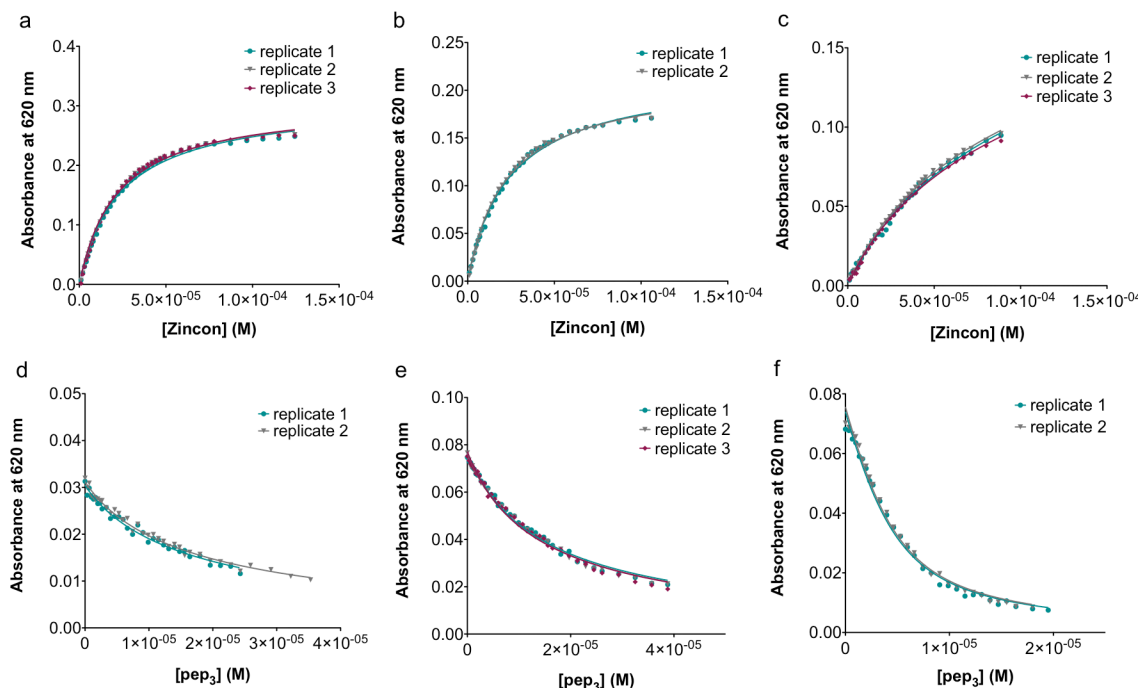


Figure 3-7. Competitive Zn(II)-binding titrations against Zincon at pH 7.5 for [Hg(II)]_S(TRIL9HL23C)₃⁻, [Hg(II)]_S(TRIL9CL19H)₃⁻, and [Hg(II)]_S(GRL2WL16CL30H)₃⁻. Plots of absorbance at 620 nm vs [Zincon] for the forward titrations of a) 15 μM [Zn(II)(OH₂/OH⁻)_N][Hg(II)]_S(TRIL9HL23C)₃ⁿ⁺, b) 10 μM [Zn(II)(OH₂/OH⁻)_N][Hg(II)]_S(TRIL9CL19H)₃ⁿ⁺, and c) 10 μM [Zn(II)(OH₂/OH⁻)_N][Hg(II)]_S(GRL2WL16CL30H)₃ⁿ⁺ and vs [pep₃] for the reverse titrations of d) [Hg(II)]_S(TRIL9HL23C)₃⁻ (2.5 μM Zn(II)Zi), e) [Hg(II)]_S(TRIL9CL19H)₃⁻ (5 μM Zn(II)Zi), and f) [Hg(II)]_S(GRL2WL16CL30H)₃⁻ (5 μM Zn(II)Zi).

Zn(II) to [Hg(II)]_S(GRL2WL16CL30H)₃⁻ is about four-fold stronger. According to these results, Zn(II) binding affinity is not significantly affected by moving the Zn(II) site along the TRI sequence or by adding an extra heptad to the sequence (**Grand**).

Characterization of Ester Hydrolysis and Inhibition

a) Zn(II) Site in [Zn(II)(OH₂/OH⁻)_N][Hg(II)]_S(TRIL9HL23C)₃ⁿ⁺. The complex [Zn(II)(OH₂/OH⁻)_N][Hg(II)]_S(TRIL9HL23C)₃ⁿ⁺ exhibits saturation kinetics for pH-dependent *p*NPA hydrolysis (Table 3-3). At pH 7.5, $k_{\text{cat}} = 0.5 (\pm 0.1) \times 10^{-3} \text{ s}^{-1}$ and $k_{\text{cat}}/K_M = 0.6 \pm 0.1 \text{ M}^{-1} \text{ s}^{-1}$ (25 °C, 20 μM catalyst). The kinetic parameters increase to 20.0 (±2.0)

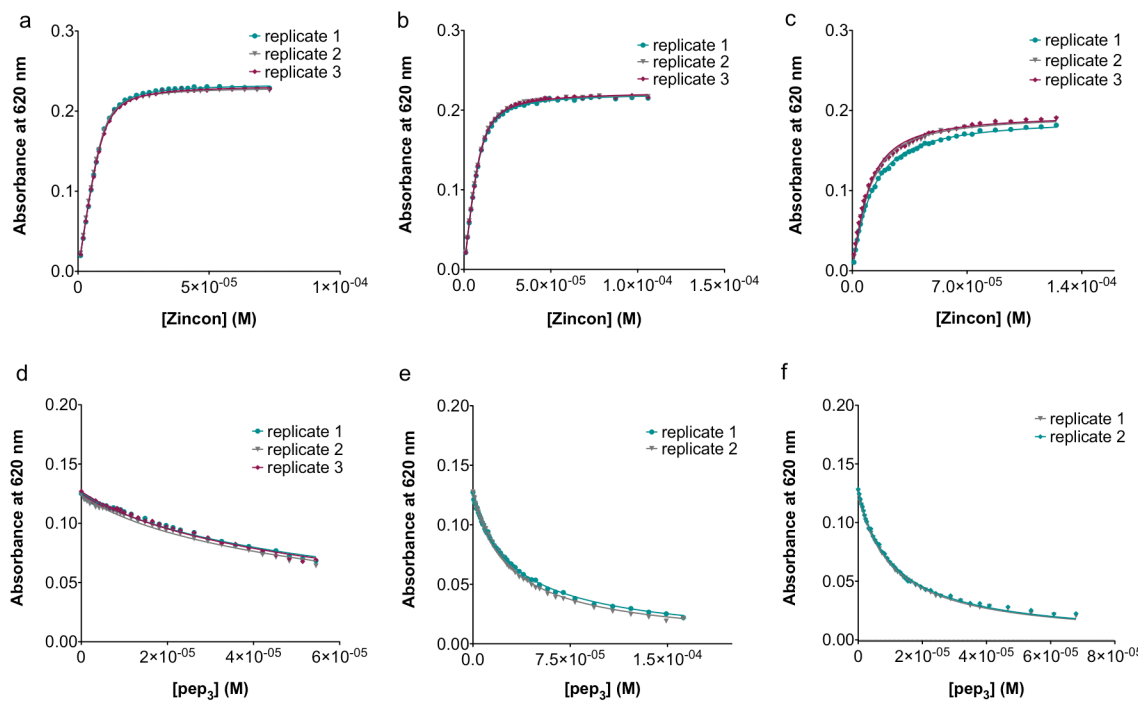


Figure 3-8. Competitive Zn(II)-binding titrations against Zincon at pH 9.0 for [Hg(II)]_s(TRIL9HL23C)₃⁻, [Hg(II)]_s(TRIL9CL19H)₃⁻, and [Hg(II)]_s(GRL2WL16CL30H)₃⁻. Plots of absorbance at 620 nm vs [Zincon] for the forward titrations of a) 10 μM [Zn(II)(OH₂/OH⁻)_N][Hg(II)]_s(TRIL9HL23C)₃ⁿ⁺, b) 10 μM [Hg(II)]_s[Zn(II)(OH₂/OH⁻)_N(TRIL9CL19H)₃ⁿ⁺, and c) 10 μM [Hg(II)]_s[Zn(II)(OH₂/OH⁻)_N(GRL2WL16CL30H)₃ⁿ⁺ and vs [pep₃] for the reverse titrations of d) [Hg(II)]_s(TRIL9HL23C)₃⁻ (5 μM Zn(II)Zi), e) [Hg(II)]_s(TRIL9CL19H)₃⁻ (5 μM Zn(II)Zi), and f) [Hg(II)]_s(GRL2WL16CL30H)₃⁻ (5 μM Zn(II)Zi).

$\times 10^{-3} \text{ s}^{-1}$ for k_{cat} and $15.8 \pm 1.1 \text{ M}^{-1} \text{ s}^{-1}$ for $k_{\text{cat}}/K_{\text{M}}$ at pH 9.5. The K_{M} values remain essentially constant, at $\sim 1 \text{ mM}$ over the pH range from 7.5 to 9.5. As for the L23H peptides, these results indicate a chemical rate-limiting step. The pH-dependency profile can be fitted ($k_{\text{cat}}/K_{\text{M}}$ vs pH) to eq 1, and a $\text{p}K_{\text{a}}$ of 9.2 ± 0.1 is obtained (Figure 3-9).

$$k_{\text{obs}} = \frac{(k_{\text{max}} * 10^{(\text{pH} - \text{p}K_{\text{a}})}) + k_{\text{min}}}{1 + 10^{(\text{pH} - \text{p}K_{\text{a}})}} \quad (1)$$

Further, the maximal $k_{\text{cat}}/K_{\text{M}}$ assuming 100% active Zn-hydroxide complex is $24 \pm 3 \text{ M}^{-1} \text{ s}^{-1}$. A similar trend is found for k_{cat} vs pH, but given the larger errors in k_{cat} due to poor

Table 3-3. pH-dependent kinetic parameters for hydrolysis of pNPA by Zn(II)-bound TRI and Grand peptides.^a

Peptide complex ^b	pH ^c	k_{cat}/K_M [M ⁻¹ s ⁻¹]	k_{cat} [s ⁻¹]	K_M [mM]
[Zn(II)(OH ₂ /OH ⁻)] _N (TRIL2WL23H) ₃ ⁿ⁺	7.5	0.41 ± 0.03	0.0011 ± 0.0002	2.7 ± 0.8
	8.0	1.07 ± 0.06	0.0029 ± 0.0005	2.7 ± 0.6
	8.5	3.3 ± 0.2	0.0060 ± 0.0007	1.8 ± 0.3
	9.0	8.9 ± 0.4	0.016 ± 0.001	1.8 ± 0.2
	9.25	12.9 ± 0.4	0.022 ± 0.001	1.7 ± 0.2
	9.5	15.5 ± 0.4	0.033 ± 0.002	2.1 ± 0.2
[Hg(II)] _S [Zn(II)(OH ₂ /OH ⁻)] _N (TRIL9CL23H) ₃ ^{n+(d)}	7.5	1.38 ± 0.04	0.0022 ± 0.0005	1.6 ± 0.4
	8.0	3.1 ± 0.1	0.0054 ± 0.0015	1.7 ± 0.5
	8.5	6.0 ± 0.1	0.012 ± 0.004	1.9 ± 0.6
	8.75	10.8 ± 0.3	0.021 ± 0.010	2.0 ± 0.9
	9.0	17.6 ± 0.3	0.038 ± 0.010	2.1 ± 0.6
	9.5	23.3 ± 0.3	0.040 ± 0.012	1.7 ± 0.5
[Zn(II)(OH ₂ /OH ⁻)] _N [Hg(II)] _S (TRIL9HL23C) ₃ ⁿ⁺	7.5	0.6 ± 0.1	0.0005 ± 0.0001	0.9 ± 0.4
	8.0	1.2 ± 0.2	0.0009 ± 0.0002	0.7 ± 0.3
	8.5	1.9 ± 0.2	0.0027 ± 0.0007	1.4 ± 0.5
	8.75	6.1 ± 0.2	0.0062 ± 0.0003	1.0 ± 0.1
	9.0	9.7 ± 0.6	0.011 ± 0.001	1.1 ± 0.1
	9.5	15.8 ± 1.1	0.020 ± 0.002	1.2 ± 0.2
[Hg(II)] _S [Zn(II)(OH ₂ /OH ⁻)] _N (TRIL9CL19H) ₃ ⁿ⁺	7.5	0.33 ± 0.01	0.0014 ± 0.0002	4.2 ± 0.9
	8.0	0.86 ± 0.02	0.0034 ± 0.0004	3.9 ± 0.5
	8.5	2.35 ± 0.08	0.0062 ± 0.0007	2.5 ± 0.4
	9.0	4.5 ± 0.2	0.010 ± 0.001	2.3 ± 0.4
	9.3	9.5 ± 0.3	0.022 ± 0.002	2.4 ± 0.3
	9.5	12.4 ± 0.4	0.035 ± 0.004	2.8 ± 0.4
[Hg(II)] _S [Zn(II)(OH ₂ /OH ⁻)] _N (GRL2WL16CL30H) ₃ ⁿ⁺	8.0	1.0 ± 0.1	0.0034 ± 0.0008	3.5 ± 1.1
	8.5	3.0 ± 0.1	0.011 ± 0.002	3.7 ± 0.7
	8.75	6.4 ± 0.2	0.022 ± 0.002	3.5 ± 0.5
	9.0	10.8 ± 0.4	0.038 ± 0.005	3.6 ± 0.6
	9.25	14.5 ± 0.4	0.059 ± 0.007	4.0 ± 0.6
	9.5	18.5 ± 0.6	0.064 ± 0.007	3.5 ± 0.5

a. Error bars result from fitting all individual rates measured (three per concentration of substrate, without averaging) to the Michaelis-Menten equation in Prism 5 (GraphPad Software)³⁴ or from Lineweaver-Burke analysis.

b. 10-20 μM active Zn(II)-bound complex.

c. pH 7.5-8.0 measured in 50 mM HEPES, 0.1 M Na₂SO₄; pH 8.5-9.5 measured in 50 mM CHES, 0.1 M Na₂SO₄.

d. Previously reported data included for comparison.

solubility of the substrate, the pK_a and especially the extrapolated maximal k_{cat} value from the fit are not reliable (Figure 3-10). Therefore, the maximal k_{cat} was estimated by using maximal k_{cat}/K_M and the K_M . Based on this analysis, the maximal k_{cat} is $\sim 0.030 \text{ s}^{-1}$. Table 3-4 summarizes these values for this peptide, the original L23H peptides with and without Hg(II) and for the L19H and **Grand** peptides (see below).

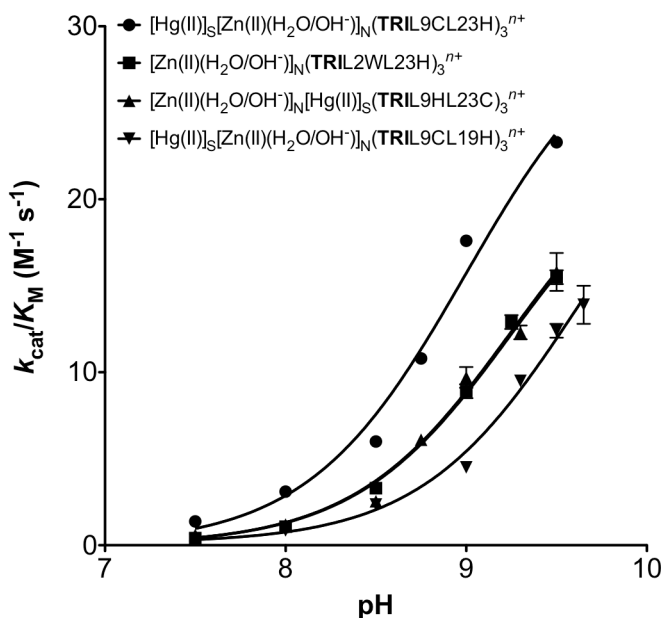


Figure 3-9. pH-dependency of the catalytic efficiency for *p*NPA hydrolysis by Zn(II)-bound TRI peptides: $[\text{Hg(II)}]_S[\text{Zn(II)(OH}_2/\text{OH}^-)]_N(\text{TRIL9CL23H})_3^{n+}$ (\bullet), $[\text{Zn(II)(OH}_2/\text{OH}^-)]_N(\text{TRIL2WL23H})_3^{n+}$ (\blacksquare), $[\text{Zn(II)(OH}_2/\text{OH}^-)]_N[\text{Hg(II)}]_S(\text{TRIL9HL23C})_3^{n+}$ (\blacktriangle), $[\text{Hg(II)}]_S[\text{Zn(II)(OH}_2/\text{OH}^-)]_N(\text{TRIL9CL19H})_3^{n+}$ (\blacktriangledown). Error bars result from fitting all individual initial rates measured (three per concentration of substrate, without averaging) to the Michaelis-Menten equation in Prism 5 (GraphPad Software).³⁴ The fitting equation used for the pH dependence (eq 1) is described in the Results section.

b) Zn(II) Site in $[\text{Hg(II)}]_S[\text{Zn(II)(OH}_2/\text{OH}^-)]_N(\text{TRIL9CL19H})_3^{n+}$. The complex $[\text{Hg(II)}]_S[\text{Zn(II)(OH}_2/\text{OH}^-)]_N(\text{TRIL9CL19H})_3^{n+}$ exhibits saturation kinetics for pH-dependent *p*NPA hydrolysis (Table 3-3). At pH 7.5, $k_{cat} = 1.4 (\pm 0.2) \times 10^{-3} \text{ s}^{-1}$ and $k_{cat}/K_M = 0.33 \pm 0.01 \text{ M}^{-1} \text{ s}^{-1}$ (25 °C, 20 μM catalyst). The kinetic parameters increase to $40 (\pm 10) \times 10^{-3} \text{ s}^{-1}$ for k_{cat} and $13.9 \pm 1.1 \text{ M}^{-1} \text{ s}^{-1}$ for k_{cat}/K_M at pH 9.65. The K_M values remain essentially constant, at $\sim 3 \text{ mM}$ over the pH range from 7.5 to 9.65. These pH trends

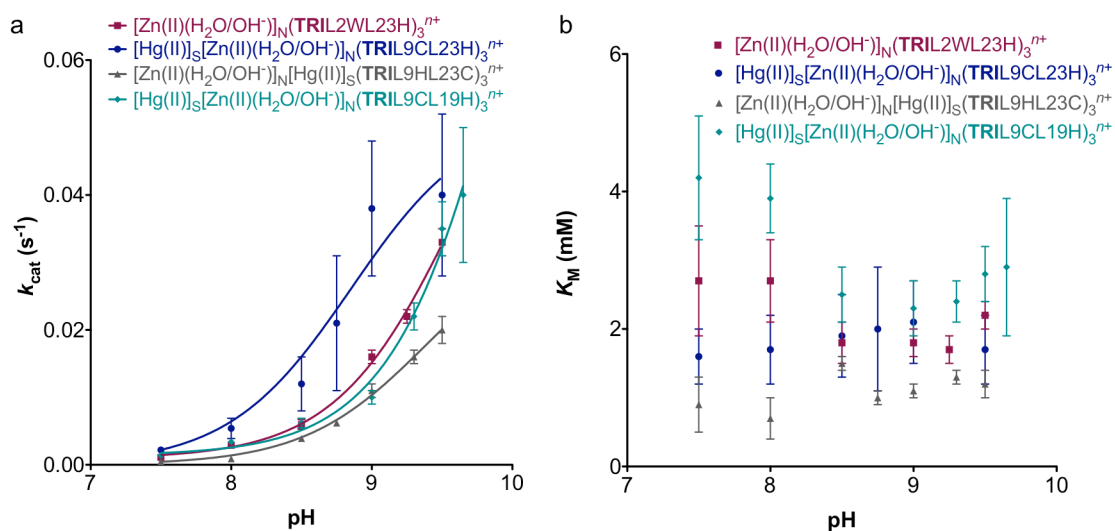


Figure 3-10. pH-dependency of a) k_{cat} and b) K_{M} parameters for *p*NPA hydrolysis by Zn(II)His₃O sites in the TRI peptides. Results are shown for [Zn(II)(OH₂/OH⁻)]_N(TRIL2WL23H)₃ⁿ⁺, [Hg(II)]_S[Zn(II)(OH₂/OH⁻)]_N(TRIL9CL23H)₃ⁿ⁺, [Zn(II)(OH₂/OH⁻)]_N[Hg(II)]_S(TRIL9HL23C)₃ⁿ⁺, and [Hg(II)]_S[Zn(II)(OH₂/OH⁻)]_N(TRIL9CL19H)₃ⁿ⁺. Error bars result from fitting all individual initial rates measured (three per concentration of substrate, without averaging) to the Michaelis-Menten equation in Prism 5 (GraphPad Software).³⁴ The fitting equation used for the pH dependence (eq 1) is described in the Results section.

Table 3-4. Kinetic $\text{p}K_{\text{a}}$, maximal efficiency, and maximal rate values for *p*NPA hydrolysis by Zn(II)-bound TRI and Grand peptides.

Peptide complex	$\text{p}K_{\text{a}}$ ^a	$k_{\text{cat}}/K_{\text{M}}^{\text{(max)}}$ [M ⁻¹ s ⁻¹] ^b	$k_{\text{cat}(\text{max})}$ [S ⁻¹] ^c
[Zn(II)(OH ₂ /OH ⁻)] _N (TRIL2WL23H) ₃ ⁿ⁺	9.2 ± 0.1	25 ± 2	~0.055
[Hg(II)] _S [Zn(II)(OH ₂ /OH ⁻)] _N (TRIL9CL23H) ₃ ⁿ⁺	9.0 ± 0.1	31 ± 4	~0.053
[Zn(II)(OH ₂ /OH ⁻)] _N [Hg(II)] _S (TRIL9HL23C) ₃ ⁿ⁺	9.2 ± 0.1	24 ± 3	~0.030
[Hg(II)] _S [Zn(II)(OH ₂ /OH ⁻)] _N (TRIL9CL19H) ₃ ⁿ⁺	9.6 ± 0.1	27 ± 5	~0.076
[Hg(II)] _S [Zn(II)(OH ₂ /OH ⁻)] _N (GRL2WL16CL30H) ₃ ⁿ⁺	9.2 ± 0.1	29 ± 3	~0.1

a. Determined by fitting individual $k_{\text{cat}}/K_{\text{M}}$ values versus pH.

b. Maximal catalytic efficiency from the fitting of $k_{\text{cat}}/K_{\text{M}}$ values versus pH (assuming that 100% active enzyme complex is present).

c. Estimated maximal rate determined as described in the text.

indicate, as for all of the TRI peptides discussed so far, that the rate-limiting step is chemical in nature. By fitting the pH-dependency profile to eq 1 for $k_{\text{cat}}/K_{\text{M}}$, a $\text{p}K_{\text{a}}$ of 9.6 ± 0.1 and a maximal efficiency of 27 ± 5 M⁻¹ s⁻¹ are obtained (Figure 3-9). The estimated

maximal k_{cat} , obtained as describe above, is $\sim 0.076 \text{ s}^{-1}$ (Table 3-4). While the highest catalytic efficiency and rate were only measured at pH 9.65, barely above the pK_a , I was unable to examine the system at even higher pH values because the salt bridge interactions stabilizing the 3SCC are interrupted.

Table 3-5. Kinetic parameters for the inhibition of *p*NPA hydrolysis by Zn(II)-bound TRI peptides at pH 8.5.^a

Peptide complex ^b & K_I (M)	[OAc ⁻] [M]	k_{cat}/K_M [M ⁻¹ s ⁻¹]	k_{cat} [s ⁻¹]	K_M [mM]
[Zn(II)(OH ₂ /OH ⁻)] _N (TRIL2WL23H) ₃ ⁿ⁺ K_I (M) = 0.34 ± 0.01	0	3.2 ± 0.1	0.0065 ± 0.0006	2.0 ± 0.3
	0.1	2.51 ± 0.05	0.0068 ± 0.0004	2.7 ± 0.2
	0.25	2.01 ± 0.07	0.0058 ± 0.0006	2.9 ± 0.4
	0.435	1.32 ± 0.07	0.0067 ± 0.0021	5.1 ± 1.9
[Hg(II)] _S [Zn(II)(OH ₂ /OH ⁻)] _N (TRIL9CL23H) ₃ ⁿ⁺ K_I (M) = 0.32 ± 0.01	0	5.4 ± 0.1	0.011 ± 0.001	2.0 ± 0.2
	0.1	4.5 ± 0.2	0.012 ± 0.001	2.6 ± 0.4
	0.2	3.6 ± 0.2	0.010 ± 0.002	2.6 ± 0.6
	0.4	2.5 ± 0.1	0.012 ± 0.003	5.0 ± 1.2
[Zn(II)(OH ₂ /OH ⁻)] _N [Hg(II)] _S (TRIL9HL23C) ₃ ⁿ⁺ K_I (M) = 0.20 ± 0.01	0	2.54 ± 0.07	0.0039 ± 0.0002	1.5 ± 0.1
	0.1	1.65 ± 0.02	0.0047 ± 0.0002	2.9 ± 0.2
	0.25	1.09 ± 0.06	0.0036 ± 0.0008	3.3 ± 0.9
	0.5	0.72 ± 0.03	0.0042 ± 0.0012	5.8 ± 1.9
[Hg(II)] _S [Zn(II)(OH ₂ /OH ⁻)] _N (TRIL9CL19H) ₃ ⁿ⁺ K_I (M) = 0.36 ± 0.01	0	2.06 ± 0.06	0.0058 ± 0.0006	2.8 ± 0.4
	0.2	1.42 ± 0.04	0.0078 ± 0.0014	5.5 ± 1.1
	0.4	0.94 ± 0.06	0.006 ± 0.003	6.5 ± 3.3
	0.6	0.73 ± 0.03	0.007 ± 0.003	9.1 ± 4.7

a. Error bars result from fitting all individual initial rates measured (three per concentration of substrate, without averaging) to the Michaelis Menten equation in Prism 5 (GraphPad Software).³⁴

b. 20-50 μM active Zn(II)-bound peptide complex.

c) Product Inhibition. The peptide complexes [Zn(II)(OH₂/OH⁻)]_N[Hg(II)]_S(**TRIL9HL23C**)₃ⁿ⁺ and [Hg(II)]_S[Zn(II)(OH₂/OH⁻)]_N(**TRIL9CL19H**)₃ⁿ⁺ were measured for the extent of product inhibition at pH 8.5. The kinetic parameters obtained at each concentration of acetate are given in Table 3-5. As for [Zn(II)(OH₂/OH⁻)]_N(**TRIL2WL23H**)₃ⁿ⁺ and [Hg(II)]_S[Zn(II)(OH₂/OH⁻)]_N(**TRIL9CL23H**)₃ⁿ⁺ described in Chapter 2, both of the peptide complexes examined in this chapter fit a competitive inhibition model, based on

non-linear competitive fits, Lineweaver-Burke analysis, and examination of the α values (Methods and Materials, Figures 3-11-3-12).

As described in chapter 2, the apo-peptides can also catalyze *p*NPA hydrolysis due to the presence of free histidine residues.⁶ Also described was the control experiment in which I attempted to inhibit this activity using 0.5 M acetate and, while some inhibition was observed (possibly because acetate may block *p*NPA from entering the 3SCC to some extent), it was less than half of that observed in the presence of Zn(II) and did not strictly fit any inhibition model. Therefore, it is concluded that the observed competitive inhibition is due to acetate competing for the ZnN₃O site.

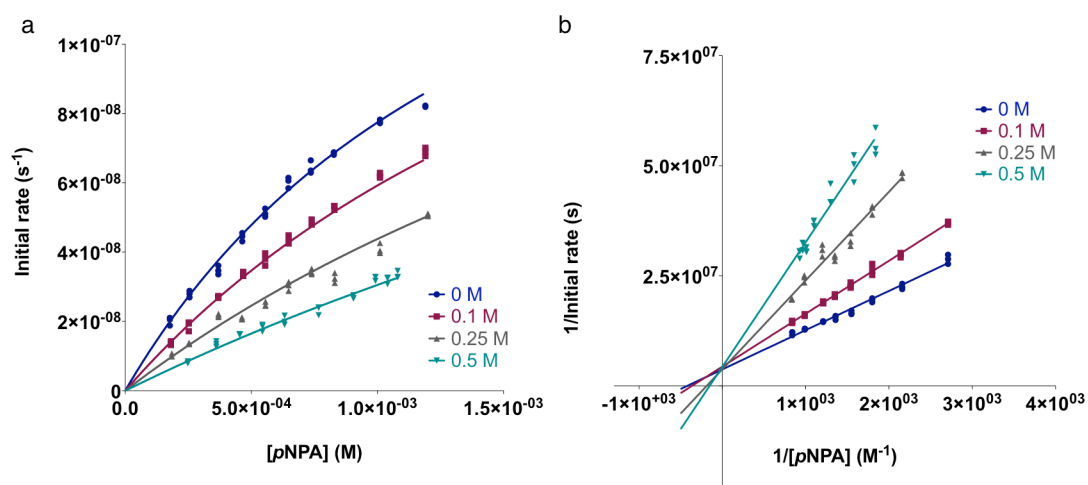


Figure 3-11. Inhibition of 50 μ M [Zn(II)(OH₂/OH⁻)]_N[Hg(II)]_S(TRIL9HL23C)₃ⁿ⁺-catalyzed *p*NPA hydrolysis by acetate at pH 8.5. a) Initial rates as a function of substrate concentration in the presence of 0, 0.1, 0.25, and 0.5 M KOAc fitted to a competitive inhibition model in Prism 5 (GraphPad Software).³⁴ The global data yields the reported K_I and corresponding error. Data shown consists of each measured individual initial rate and does not represent averages. Fitting the same data to a mixed inhibition model yielded $\alpha \approx 3 \times 10^{13}$, supporting the assignment of a competitive inhibition model.⁵⁴ b) Lineweaver-Burke (double-reciprocal) plots corresponding to the data in a). Visual inspection of the intersection of linear fits to each dataset (at the y-axis) also supports a competitive inhibition model.

d) Zn(II) Site in [Hg(II)]_S[Zn(II)(OH₂/OH⁻)]_N(GRL2WL16CL30H)₃ⁿ⁺. The complex [Hg(II)]_S[Zn(II)(OH₂/OH⁻)]_N(GRL2WL16CL30H)₃ⁿ⁺ exhibits saturation

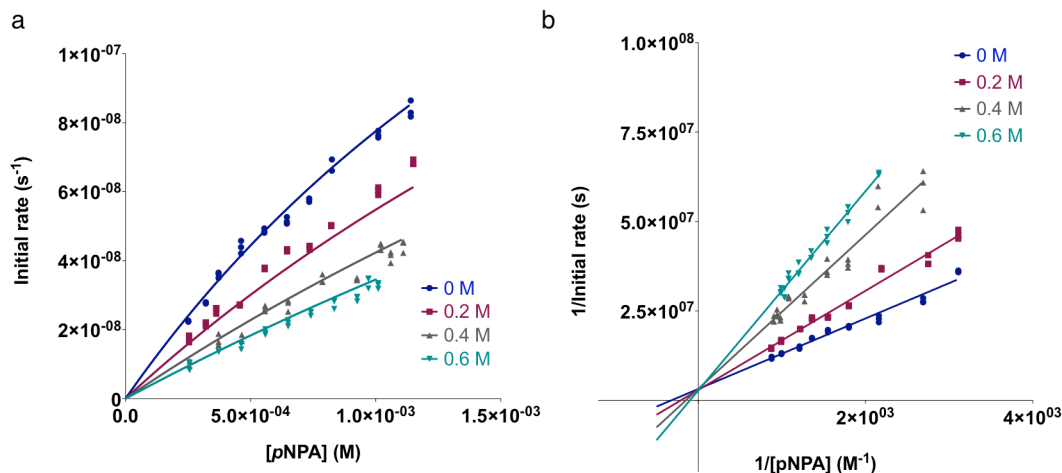


Figure 3-12. Inhibition of 50 μM $[\text{Hg(II)}]_s[\text{Zn(II)(OH}_2/\text{OH}^-)]_N(\text{TRIL9CL19H})_3^{n+}$ -catalyzed *p*NPA hydrolysis by acetate at pH 8.5. **a)** Initial rates as a function of substrate concentration in the presence of 0, 0.2, 0.4, and 0.6 M KOAc fitted to a competitive inhibition model in Prism 5 (GraphPad Software).³⁴ The global data yields the reported K_I and corresponding error. Data shown consists of each measured individual initial rate and does not represent averages. Fitting the same data to a mixed inhibition model yielded $\alpha \approx 31$ supporting the assignment of a competitive inhibition model.⁵⁴ **b)** Lineweaver-Burke (double-reciprocal) plots corresponding to the data in a). Visual inspection of the intersection of linear fits to each dataset (at the y-axis) also supports a competitive inhibition model.

kinetics for pH-dependent *p*NPA hydrolysis. The catalytic rates range from $0.0034 \pm 0.0008 \text{ s}^{-1}$ at pH 8.0 to $0.064 \pm 0.007 \text{ s}^{-1}$ at pH 9.5 and the efficiencies (k_{cat}/K_M) from $1.0 \pm 0.1 \text{ M}^{-1} \text{ s}^{-1}$ up to $18.5 \pm 0.6 \text{ M}^{-1} \text{ s}^{-1}$ (Table 3-3). The catalytic efficiencies were fitted to eq 1 to yield $\text{p}K_a = 9.2 \pm 0.1$ and maximal k_{cat}/K_M of $29 \pm 3 \text{ M}^{-1} \text{ s}^{-1}$ (Figure 3-13, Table 3-4). As observed for the **TRI** peptides, the K_M values remain essentially constant within the pH range examined ($K_M \sim 3.5\text{-}4 \text{ mM}$, Figure 3-14), although they are consistently higher, probably reflecting the increased stability of the **Grand** structure (which is one heptad repeat longer than **TRI**) relative to **TRI**. The estimated maximal k_{cat} is $\sim 0.1 \text{ s}^{-1}$, about twice as high as those determined for the L23H sites.

Discussion

The aim of the work presented in this chapter is to examine how the location of a minimal hydrolytic zinc site along the sequence of a *de novo*-designed 3SCC can affect

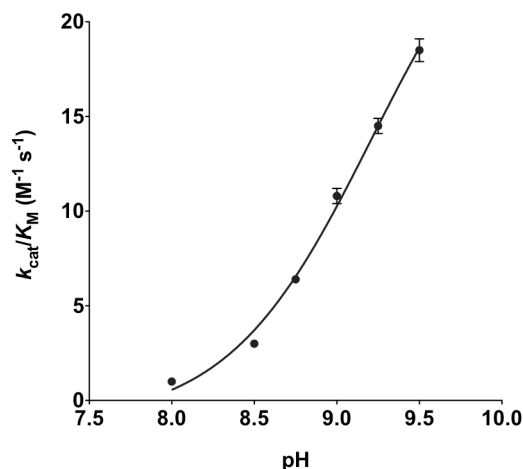


Figure 3-13. pH-dependency of k_{cat}/K_M for *p*NPA hydrolysis by $[Hg(II)]_S[Zn(II)(OH_2/OH^-)]_N(GRL2WL16CL30H)_3^{n+}$. Error bars result from fitting all individual initial rates measured (three per concentration of substrate, without averaging) to the Michaelis-Menten equation in Prism 5 (GraphPad Software).³⁴ The fitting equation used for the pH dependence (eq 1) is described in the Results section.

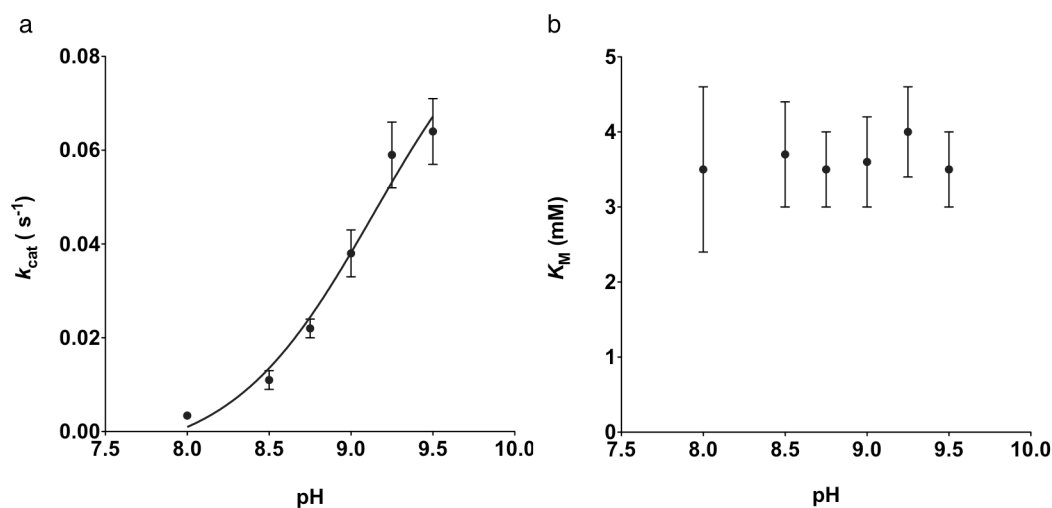


Figure 3-14. pH-dependency of a) k_{cat} and b) K_M parameters for *p*NPA hydrolysis by $[Hg(II)]_S[Zn(II)(OH_2/OH^-)]_N(GRL2WL16CL30H)_3^{n+}$. Error bars result from fitting all individual initial rates measured (three per concentration of substrate, without averaging) to the Michaelis-Menten equation in Prism 5 (GraphPad Software).³⁴ The fitting equation used for the pH dependence (eq 1) is described in the Results section.

the catalytic efficiency, rate, pK_a , solvent and substrate access, and binding affinities. Although metalloprotein design has now yielded a number of successful metal-bound and

even catalytically active constructs, the question of where to put a metal site along a linear, repetitive sequence has not been thoroughly addressed. Often there are several possibilities in a given sequence that would appear equivalent but may differ for metal affinity, substrate access, or protein dynamics. Now that I have achieved the design of a successful minimal hydrolytic zinc site (Chapter 2), I would like to begin incorporating secondary interactions that will likely involve building hydrogen-bonding networks and channels. In order to do so, however, I need to examine whether the metal site may be moved to an alternate location in the sequence (or if it can be put into a more stable but similar sequence) so as to preserve the folding when incorporating polar residues. Therefore, studying various locations of the minimal site to understand how the location may affect the active site properties is very useful towards designing increasing levels of complexity.

The first design I decided to examine was **TRIL9HL23C**, which inverts the sequence positions of the structural and catalytic sites. Provided that Zn(II) and coordinated solvent are oriented similarly toward the N-terminus of the coiled coil, as found in the structure of the previously reported⁶ $[\text{Hg(II)}]_s[\text{Zn(II)}(\text{OH}_2/\text{OH}^-)]_N(\text{CSL9PenL23H})_3^{n+}$ (Chapter 2), the bound water/hydroxide should now be more exposed to bulk solvent and the site may better accommodate the substrate (Figure 3-15). The folding of **TRIL9HL23C** is similar to that observed for both **TRIL2WL23H** and **TRIL9CL23H** (~70-80% α -helical content) and, as with $(\text{TRIL9CL23H})^{n-}$, the addition of Hg(II) to the Cys₃ site further stabilizes $(\text{TRIL9HL23C})_3^{n-}$ (Figures 3-3-3-4). Hg(II) binding was evaluated using UV-Vis spectroscopy and confirms both 1:1 binding in a trigonal geometry to the Cys₃ site in $(\text{TRIL9HL23C})_3^{n-}$, and that the peptide is associating in a trimeric structure, certainly in the presence of Hg(II).^{6,37,38} Apparent dissociation constants in the μM range indicate that Zn(II) remains bound well, although relatively weak compared to native Zn(II) enzymes (often with $K_d \sim \text{nM-pM}$).^{12,39-44} These K_d 's (Table 3-2, Figures 3-7-3-8) are an order of magnitude weaker than determined for $[\text{Hg(II)}]_s[\text{Zn(II)}(\text{OH}_2/\text{OH}^-)]_N(\text{TRIL9CL23H})_3^{n+}$ and $[\text{Zn(II)}(\text{OH}_2/\text{OH}^-)]_N(\text{TRIL2WL23H})_3^{n+}$ at pH 7.5 and a factor of four weaker at pH 9.0. Thus, while removal of Hg(II) does not alter Zn(II) affinity (Chapter 2), reorientation of the Zn(II) site between the 9 and 23 positions (two **a** sites) leads to a ten-fold weaker binding to

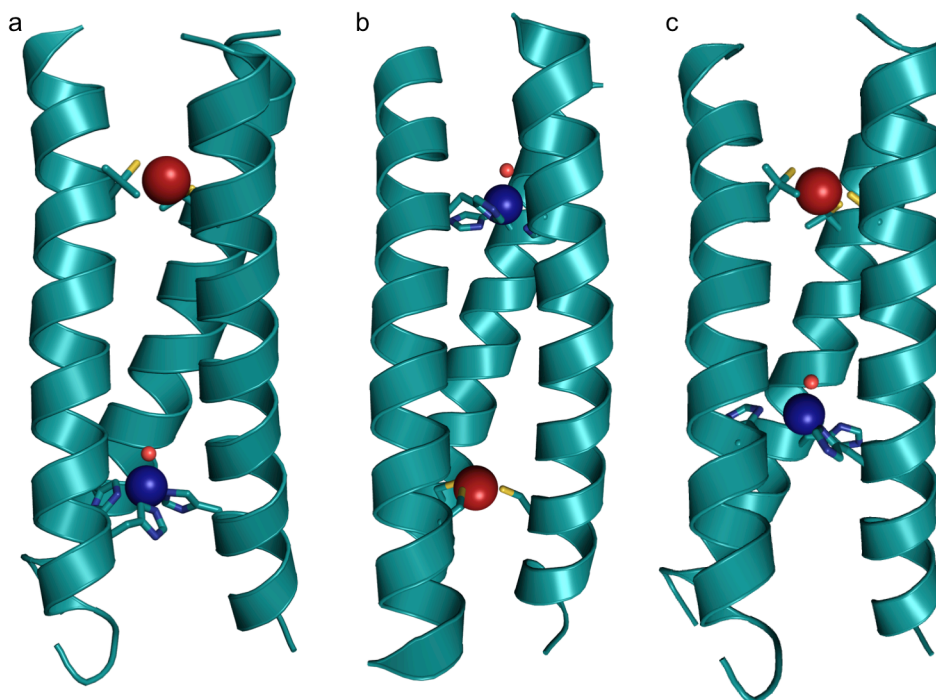


Figure 3-15. Comparison of the X-ray crystal structure of a) $[\text{Hg}(\text{II})]_{\text{S}}[\text{Zn}(\text{II})(\text{OH}_2/\text{OH}^-)]_{\text{N}}(\text{CSL9PenL23H})_3^{n+}$ (3PBJ)⁶ with PyMOL models of b) $[\text{Zn}(\text{II})(\text{OH}_2/\text{OH}^-)]_{\text{N}}[\text{Hg}(\text{II})]_{\text{S}}(\text{TRIL9HL23C})_3^{n+}$ based on the coordinates of 2JGO⁵⁵ and c) $[\text{Hg}(\text{II})]_{\text{S}}[\text{Zn}(\text{II})(\text{OH}_2/\text{OH}^-)]_{\text{N}}(\text{TRIL9CL19H})_3^{n+}$ based on the coordinates of 3PBJ. Models were prepared in PyMOL using the mutagenesis option and PyMOL's rotamer library.⁵⁶

$[\text{Hg}(\text{II})]_{\text{S}}(\text{TRIL9HL23C})_3^-$ ($K_{\text{d}} \sim 8 \mu\text{M}$) demonstrating that sequence position is important for metal affinity.

The Pecoraro group had previously shown that the $\text{p}K_{\text{a}}$ for thiolate binding to Cd(II) was critically dependent on whether cysteines were incorporated into **a** or **d** sites and subsequent X-ray crystallographic analysis indicated that the thiolate conformations were varied between the two types of positions.^{16,45} Reasoning that similar behavior might occur with Zn(II) imidazoles in **a** versus **d** sites along the sequence, I prepared **TRIL9CL19H**. Here, the structural site was held constant relative to the original model, but the catalytic site was moved one Leu layer closer to the N-terminus into a **d** site. Assessment of the stability of this complex in the presence and absence of Hg(II) revealed similar behavior to $(\text{TRIL9CL23H})_3^{n-}$ and $(\text{TRIL9HL23C})_3^{n-}$ (Figures 3-3-3-4). Zn(II) binding to $[\text{Hg}(\text{II})]_{\text{S}}(\text{TRIL9CL19H})_3^-$ is about five-fold weaker ($K_{\text{d}} = 3.7 \pm 1.3 \mu\text{M}$) than the L23H derivatives. This could be due to different orientation of the

histidines in **a** vs **d** sites or because the site is more constrained when located in the center of the coiled coil. All four peptides have stronger K_d 's (by three- to ten-fold) at pH 9.0 (Table 3-2), but follow the same trend with sequence position. All binding affinities are sufficiently strong to ensure Zn(II) is fully bound under the catalytic conditions described below. This is the first systematic evaluation of changes in binding affinities of a catalytic site as it is varied along a helical structure.

I next evaluated the catalytic activities of these two designs. Hydrolysis of *p*NPA by $[\text{Zn(II)(OH}_2\text{/OH}^-)]_N[\text{Hg(II)}]_S(\text{TRIL9HL23C})_3^{n+}$ and $[\text{Hg(II)}]_S[\text{Zn(II)(OH}_2\text{/OH}^-)]_N(\text{TRIL9CL19H})_3^{n+}$ was monitored as a function of pH. Both of these peptide complexes show diminished catalytic efficiency (none more than two-fold) relative to the original model and the model lacking the HgS₃ site at pH 9.5 (Table 3-3). According to the kinetics studies described in Chapter 2, the presence of the Hg(II) site does not have any effect on the hydrolytic activity of the Zn(II) site. The pK_a 's of $[\text{Zn(II)(OH}_2\text{/OH}^-)]_N(\text{TRIL2WL23H})_3^{n+}$, $[\text{Hg(II)}]_S[\text{Zn(II)(OH}_2\text{/OH}^-)]_N(\text{TRIL9CL23H})_3^{n+}$, and $[\text{Zn(II)(OH}_2\text{/OH}^-)]_N[\text{Hg(II)}]_S(\text{TRIL9HL23C})_3^{n+}$ are similar ($9.0\text{-}9.2 \pm 0.1$); however, that of $[\text{Hg(II)}]_S[\text{Zn(II)(OH}_2\text{/OH}^-)]_N(\text{TRIL9CL19H})_3^{n+}$ increases to 9.6 ± 0.2 (Figure 3-9, Table 3-4). This increase might be due to the location of the metal site further within the core of the 3SCC relative to the other designs or simply because it is a **d** site and the His ligands may be oriented differently. Presumably, the pK_a represents deprotonation of Zn(II)-bound water to form coordinated hydroxide, which is proposed to be the hydrolytically active species. It appears that the position of the catalytic site along the sequence of the peptide has a modest role in tuning this pK_a , with the highest value for the least solvent accessible site. The pK_a 's for the complexes remain ~ 2 units higher than that for CAII (6.8)⁴⁶. This suggests that more drastic modification to the second sphere environment and beyond (probably through incorporation of hydrogen bonding) will be required to reduce the pK_a to a more desirable value.

Regardless, since the pK_a 's for these complexes are not identical, comparing their rates at pH 9.5 may not provide a complete picture. The nature of the designed peptide does not allow for the rates to be measured at pH's much higher than 9.5 because salt bridge interactions (Glu-Lys) that stabilize the coiled coil will be interrupted. However, in addition to pK_a 's, eq 1 also yields a value for the maximal catalytic efficiency

(theoretical maximal efficiency if 100% of the Zn(II)-hydroxide complex were present). Although individual catalytic efficiencies are obviously different from one peptide to the next at pH 9.5, these extrapolated maximal values are not very different, within error (Table 3-4) suggesting that ester hydrolysis is independent of the Zn(II) position. However, significant differences are observed when the individual k_{cat} and K_M values are analyzed. For all peptides, the K_M values are generally pH-independent (Figure 3-10), but differ relative to each other. The K_M 's of $[\text{Hg(II)}]_S[\text{Zn(II)(OH}_2/\text{OH}^-)]_N(\text{TRIL9CL23H})_3^{n+}$ and $[\text{Zn(II)(OH}_2/\text{OH}^-)]_N(\text{TRIL2WL23H})_3^{n+}$ are the same (~ 2 mM) but those of $[\text{Zn(II)(OH}_2/\text{OH}^-)]_N[\text{Hg(II)}]_S(\text{TRIL9HL23C})_3^{n+}$ are ~ 1 mM. This result supports the notion that when the catalytic site is moved to the N-terminal end of the sequence, the substrate can more easily access the active site since it is expected to point towards the solvent. When the catalytic site is moved to the 19th position, there seems to be a modest increase in the K_M (2.8 ± 0.4 mM, pH 9.5). As with catalytic efficiency, one can plot k_{cat} vs pH to fit for kinetic $\text{p}K_a$'s and maximal k_{cat} values, but given the larger errors in k_{cat} due to poor solubility of the substrate, the extrapolated values obtained from these fits are not reliable (Figure 3-10). Therefore, maximal k_{cat} was estimated by using maximal k_{cat}/K_M and the K_M for that particular peptide. Based on analysis of these values (Table 3-4), it is apparent that the most solvent-exposed site in $[\text{Zn(II)(OH}^-)]_N[\text{Hg(II)}]_S(\text{TRIL9HL23C})_3^{n+}$ has the lowest rate, while that furthest in the interior of the 3SCC, $[\text{Hg(II)}]_S[\text{Zn(II)(OH}^-)]_N(\text{TRIL9CL19H})_3^{n+}$, has the highest. There is no significant difference in these values between $[\text{Hg(II)}]_S[\text{Zn(II)(OH}^-)]_N(\text{TRIL9CL23H})_3^{n+}$ and the peptide lacking the Hg(II)₃ site.

Another method was needed to validate these conclusions on substrate binding access. Therefore, I evaluated product inhibition using acetate anion (as described in Chapter 2 for $[\text{Hg(II)}]_S[\text{Zn(II)(OH}_2/\text{OH}^-)]_N(\text{TRIL9CL23H})_3^{n+}$ and $[\text{Zn(II)(OH}_2/\text{OH}^-)]_N(\text{TRIL2WL23H})_3^{n+}$), which should follow a similar dependence to substrate binding. The inhibition of hydrolytic activity by $[\text{Zn(II)(OH}_2/\text{OH}^-)]_N[\text{Hg(II)}]_S(\text{TRIL9HL23C})_3^{n+}$ and $[\text{Hg(II)}]_S[\text{Zn(II)(OH}_2/\text{OH}^-)]_N(\text{TRIL9CL19H})_3^{n+}$ was evaluated at pH 8.5 and competitive inhibition was observed in both cases (Figures 3-11-3-12). The K_I for $[\text{Hg(II)}]_S[\text{Zn(II)(OH}_2/\text{OH}^-)]_N(\text{TRIL9CL19H})_3^{n+}$ (0.36 ± 0.01 M) is in the same range as those for the L23H sites (0.32-0.34 M) (Table 3-5). On the other hand, the inhibition

constant for $[\text{Zn(II)(OH}_2/\text{OH}^-)]_N[\text{Hg(II)}]_S(\text{TRIL9HL23C})_3^{n+}$ is lower, 0.20 ± 0.01 M. Therefore, the trend for the K_I 's is analogous to what was observed for the kinetic parameter, K_M . This finding further supports the notion that moving the active site to the N-terminal end of the trimer leads to increased substrate and solvent access. This is an important finding for future design endeavors in which one may wish to control substrate access and selectivity or the level of product inhibition in a helical structure.

In addition to varying the position of the minimal site along the sequence of **TRI**, I next decided to examine the effects of placing the site into a more stable related sequence, **Grand**. **Grand** is one heptad repeat longer than **TRI** and, in general, each heptad contributes ~ 9 kcal mol⁻¹ towards stabilization.^{47,48} One may imagine that upon incorporating the polar residues required to build hydrogen-bonding channels into the hydrophobic interior of **TRI**, it may not remain well folded and a more stable sequence could be required. To design the **Grand** peptide corresponding to the original model **TRIL9CL23H**, the His₃ site position was held constant relative to the C-terminal end (this is the 30th position in **Grand**, which is 37 residues long). Then, because the 9th position for the structural site in **TRIL9CL23H** is located two heptads towards the N-terminus from the 23rd position, the structural site in **Grand** was placed two heptads towards the N-terminus, in the 16th position. The resulting sequence, **GRL2WL16CL30H**, also contains a tryptophan in the 2nd position like **TRIL2WL23H**, as a spectroscopic tag for peptide concentration determination. First, the folding of **GRL2WL16CL30H** was examined in the presence and absence of Hg(II). This peptide, as might be expected, displays a higher percent folding than the **TRI** peptides containing His substitutions ($\sim 85\%$ vs 70-80% α -helical content for **GRL2WL16CL30H** and His-substituted **TRI** peptides, respectively) and follows the same pattern of increased stabilization upon Hg(II) binding (Figure 3-5). Further, the midpoints for unfolding of $(\text{GRL2WL16CL30H})_3^{n-}$ and $[\text{Hg(II)}]_S(\text{GRL2WL16CL30H})_3^-$ are shifted to higher concentrations of denaturant by ~ 1.5 M each relative to those for $(\text{TRIL9CL23H})_3^{n-}$ and $[\text{Hg(II)}]_S(\text{TRIL9CL23H})_3^-$, respectively (Figure 3-6). The dissociation constants measured for Zn(II) binding to $[\text{Hg(II)}]_S(\text{GRL2WL16CL30H})_3^-$ fall close to the same range as for the **TRI** peptides (0.4 ± 0.1 μM at pH 7.5 and 0.11 ± 0.05 μM at pH 9.0), and are just slightly stronger than those for the L23H site (Figures 3-7-3-8, Table 3-2). As for

the other peptides, *p*NPA hydrolysis was measured and, while the catalytic efficiency is again similar to that for the other peptides, there are differences in the K_M and k_{cat} values. At pH 9.5, the k_{cat} is $0.064 \pm 0.007 \text{ s}^{-1}$ for $[\text{Hg(II)}]_S[\text{Zn(II)(OH}_2/\text{OH}^-)]_N(\text{GRL2WL16CL30H})_3^{n+}$ as compared to $\sim 0.040 \text{ s}^{-1}$ for $[\text{Hg(II)}]_S[\text{Zn(II)(OH}_2/\text{OH}^-)]_N(\text{TRIL9CL23H})_3^{n+}$ and the K_M is $\sim 3.5\text{-}4.0 \text{ mM}$ over the pH range (8.0-9.5) for $[\text{Hg(II)}]_S[\text{Zn(II)(OH}_2/\text{OH}^-)]_N(\text{GRL2WL16CL30H})_3^{n+}$ as compared to $\sim 2 \text{ mM}$ for the original model (Table 3-3). The pK_a is similar to those for both L23H sites and the L9H site (9.2 ± 0.1), as is the maximal k_{cat}/K_M ($29 \pm 3 \text{ M}^{-1} \text{ s}^{-1}$), but the maximal k_{cat} ($\sim 0.1 \text{ s}^{-1}$) is about two-fold higher than those for the L23H sites ($\sim 0.054 \text{ s}^{-1}$) (Figures 3-13-3-14). Therefore, by increasing the stability of the sequence through addition of an extra heptad (and keeping the Zn(II) site close to the C-terminus), substrate access is decreased while the catalytic rate is increased about two-fold. The two opposing effects result in a nearly identical catalytic efficiency, again illustrating that a significant amount of hydrolytic activity can be achieved simply by placing a minimal Zn(II) site into an α -helical coiled coil. Further, the kinetic analysis of $[\text{Hg(II)}]_S[\text{Zn(II)(OH}_2/\text{OH}^-)]_N(\text{GRL2WL16CL30H})_3^{n+}$ directly demonstrates the tradeoff that must occur between protein stability and catalytic activity.

Conclusion

Herein I have presented the first detailed study of systematic movement of an active site along the sequence of an α -helical coiled coil in order to examine how changes in location of a metal site affect its properties. This work, combined with that for other designs^{8,9,11,49-53}, suggests there may be a limit to the affinity that can be achieved solely with three protein ligands. Only a \sim ten-fold variation in binding affinity is observed when the active site is moved along the 3SCC and into a 3SCC one heptad repeat longer. Additionally, location of the active site at either end of a helical bundle does not appear to play a large role in tuning the Zn-OH₂ pK_a , thus allowing the desired metal site to be placed into the structure based on where it may be easiest to implement further secondary interactions to tune the pK_a and catalytic activity, such as hydrogen-bonding networks. The same pK_a is also observed in the lengthened sequence when the position of the active

site is held constant relative to the C-terminus. However, because a change in pK_a is observed upon going further into the interior of the coiled coil to a **d** site, one may exploit this to achieve effectively different catalytic efficiencies when designing models for specific pH conditions.

By moving the site from the C-terminus of the coiled coil to the N-terminus, solvent, substrate, and inhibitor accessibilities are significantly increased, whereas when the metal center is moved further into the core of the structure (and to a **d** site), access decreases modestly. As a consequence, the estimated maximal rate of the L19H site increases by a factor of 2.5 relative to the L9H site. Similarly, moving the metal center into a more stable sequence, yet retaining its position relative to the C-terminus, significantly decreases substrate access and a two-fold increase in the estimated maximal rate relative to the L23H site is observed. Nevertheless, the fact that the catalytic efficiency (k_{cat}/K_M) is retained in all of these models implies that this minimal first coordination sphere-only Zn(II) site is alone enough to confer significant hydrolytic activity. This finding means that, at least in these systems, the location of the minimal active site can be chosen to optimize stability, substrate access and metal binding and for proximity to ideal positions for secondary interactions, all while retaining catalytic efficiency. The two complexes with Zn(II)His₃ sites in the same sequence position (one with and one without the structural site) give similar results for almost all of the measured parameters. Thus, a separate stabilizing site is not detrimental to the properties of the catalytic site, demonstrating that future designs incorporating two separate metal centers with different or complementary functions can be realized.

The lack of any significant change in catalytic efficiency for the hydrolysis reactions in these coiled coils implies that future work will focus on refining the second coordination sphere environment around the metal center and defining solvent channels, but not be overly concerned about the effect of location on catalytic activity. This is contrary to the previous observation that location of an FeHis₃ site in thioredoxin plays an important role in oxygen reactivity. Certainly, with coiled coils sequence position does not account for the orders-of-magnitude differences between designed metalloproteins and native enzymes. Overall, this work provides an excellent foundation for the engineering of a hydrolytically active minimal Zn(II) site into an α -helical coiled coil.

References

- (1) Handel, T.; DeGrado, W. F. *J. Am. Chem. Soc.* **1990**, *112*, 6710–6711.
- (2) Klemba, M.; Regan, L. *Biochemistry* **1995**, *34*, 10094–10100.
- (3) Lombardi, A.; Summa, C. M.; Geremia, S.; Randaccio, L.; Pavone, V.; DeGrado, W. F. *Proc. Natl. Acad. Sci. U.S.A.* **2000**, *97*, 6298–6305.
- (4) Faiella, M.; Andreozzi, C.; de Rosales, R. T. M.; Pavone, V.; Maglio, O.; Nastri, F.; DeGrado, W. F.; Lombardi, A. *Nat. Chem. Biol.* **2009**, *5*, 882–884.
- (5) Reig, A. J.; Pires, M. M.; Snyder, R. A.; Wu, Y.; Jo, H.; Kulp, D. W.; Butch, S. E.; Calhoun, J. R.; Szyperski, T.; Szyperski, T. G.; Solomon, E. I.; DeGrado, W. F. *Nat. Chem.* **2012**, *4*, 900–906.
- (6) Zastrow, M. L.; Peacock, A. F. A.; Stuckey, J. A.; Pecoraro, V. L. *Nat. Chem.* **2012**, *4*, 118–123.
- (7) Der, B. S.; Edwards, D. R.; Kuhlman, B. *Biochemistry* **2012**, *51*, 3933–3940.
- (8) Kiyokawa, T.; Kanaori, K.; Tajima, K.; Koike, M.; Mizuno, T.; Oku, J.-I.; Tanaka, T. *J. Pept. Res.* **2004**, *63*, 347–353.
- (9) Pessi, A.; Bianchi, E.; Cramer, A.; Venturini, S.; Tramontano, A.; Sollazzo, M. *Nature* **1993**, *362*, 367–369.
- (10) Zhu, C.; Zhang, C.; Liang, H.; Lai, L. *Protein Cell* **2011**, *2*, 1006–1013.
- (11) Regan, L. *Trends Biochem. Sci.* **1995**, *20*, 280–285.
- (12) Christianson, D. W.; Fierke, C. A. *Acc. Chem. Res.* **1996**, *29*, 331–339.
- (13) Liang, Z.; Xue, Y.; Behravan, G.; Jonsson, B. H.; Lindskog, S. *Eur. J. Biochem.* **1993**, *211*, 821–827.
- (14) Krebs, J. F.; Ippolito, J. A.; Christianson, D. W.; Fierke, C. A. *J. Biol. Chem.* **1993**, *268*, 27458–27466.
- (15) Peacock, A. F. A.; Iranzo, O.; Pecoraro, V. L. *Dalton Trans.* **2009**, 9226, 2271–2280.
- (16) Matzapetakis, M.; Farrer, B. T.; Weng, T.-C.; Hemmingsen, L.; Penner-Hahn, J. E.; Pecoraro, V. L. *J. Am. Chem. Soc.* **2002**, *124*, 8042–8054.
- (17) Matzapetakis, M.; Pecoraro, V. L. *J. Am. Chem. Soc.* **2005**, *127*, 18229–18233.
- (18) Iranzo, O.; Chakraborty, S.; Hemmingsen, L.; Pecoraro, V. L. *J. Am. Chem. Soc.* **2011**, *133*, 239–251.
- (19) Benson, D. E.; Wisz, M. S.; Hellinga, H. W. *Proc. Natl. Acad. Sci. U.S.A.* **2000**, *97*, 6292–6297.
- (20) Wisz, M. S.; Garrett, C. Z.; Hellinga, H. W. *Biochemistry* **1998**, *37*, 8269–8277.
- (21) Chan, W. C.; White, P. D. *Fmoc Solid Phase Peptide Synthesis: A Practical Approach*; Chan, W. C.; White, P. D., Eds.; Oxford University Press: New York, 2000; Vol. 222.
- (22) Farrer, B. T.; Harris, N. P.; Balchus, K. E.; Pecoraro, V. L. *Biochemistry* **2001**, *40*, 14696–14705.
- (23) Habeeb, A. F. *Meth. Enzymol.* **1972**, *25*, 457–464.
- (24) Riddles, P.; Blakeley, R.; Zerner, B. *Meth. Enzymol.* **1983**, *91*, 49–60.
- (25) Mantle, M.; Stewart, G.; Zayas, G.; King, M. *Biochem. J.* **1990**, *266*, 597–604.
- (26) Dieckmann, G. R.; McRorie, D. K.; Lear, J. D.; Sharp, K. A.; DeGrado, W. F.; Pecoraro, V. L. *J. Mol. Biol.* **1998**, *280*, 897–912.
- (27) Rush, R. M.; Yoe, J. H. *Anal. Chem.* **1954**, *26*, 1345–1347.

- (28) Sadek, F. S.; Schmid, R. W.; Reilley, C. N. *Talanta* **1959**, *2*, 38–51.
- (29) Talmard, C.; Bouzan, A.; Faller, P. *Biochemistry* **2007**, *46*, 13658–13666.
- (30) Shaw, C. F.; Laib, J. E.; Savas, M. M.; Petering, D. H. *Inorg. Chem.* **1990**, *29*, 403–408.
- (31) Mekmouche, Y.; Coppel, Y.; Hochgräfe, K.; Guilloureau, L.; Talmard, C.; Mazarguil, H.; Faller, P. *ChemBioChem* **2005**, *6*, 1663–1671.
- (32) Laib, J.; Shaw, C. F.; Petering, D. H.; Eidsness, M. K.; Elder, R. C.; Garvey, J. S. *Biochemistry* **1985**, *24*, 1977–1986.
- (33) Säbel, C. E.; Neureuther, J. M.; Siemann, S. *Anal. Biochem.* **2010**, *397*, 218–226.
- (34) GraphPad Prism version 5.00 for Mac, GraphPad Software, San Diego California USA, www.graphpad.com.
- (35) Verpoorte, J. A.; Mehta, S.; Edsall, J. T. *J. Biol. Chem.* **1967**, *242*, 4221–4229.
- (36) Marangoni, A. G. *Enzyme Kinetics; reversible enzyme inhibition*; John Wiley & Sons, Inc.: Hoboken, NJ, USA, 2002; pp. 61–69.
- (37) Pecoraro, V. L.; Peacock, A. F. A.; Iranzo, O.; Luczkowski, M. *ACS Symp. Ser.* **2009**, *1012*, 183–197.
- (38) Iranzo, O.; Thulstrup, P. W.; Ryu, S.-B.; Hemmingsen, L.; Pecoraro, V. L. *Chem.--Eur. J.* **2007**, *13*, 9178–9190.
- (39) Hitomi, Y.; Outten, C. E.; O'Halloran, T. V. *J. Am. Chem. Soc.* **2001**, *123*, 8614–8615.
- (40) Fierke, C. A.; Thompson, R. B. *Biomaterials* **2001**, *14*, 205–222.
- (41) Song, H.; Wilson, D. L.; Farquhar, E. R.; Lewis, E. A.; Emerson, J. P. *Inorg. Chem.* **2012**, *51*, 11098–11105.
- (42) Kiefer, L. L.; Krebs, J. F.; Paterno, S. A.; Fierke, C. A. *Biochemistry* **1993**, *32*, 9896–9900.
- (43) McCall, K. A.; Fierke, C. A. *Biochemistry* **2004**, *43*, 3979–3986.
- (44) Maret, W. *J. Nutr.* **2003**, *133*, 1460s–1462s.
- (45) Chakraborty, S.; Touw, D. S.; Peacock, A. F. A.; Stuckey, J.; Pecoraro, V. L. *J. Am. Chem. Soc.* **2010**, *132*, 13240–13250.
- (46) Fierke, C. A.; Calderone, T. L.; Krebs, J. F. *Biochemistry* **1991**, *30*, 11054–11063.
- (47) Ghosh, D.; Lee, K.-H.; Demeler, B.; Pecoraro, V. L. *Biochemistry* **2005**, *44*, 10732–10740.
- (48) Su, J. Y.; Hodges, R. S.; Kay, C. M. *Biochemistry* **1994**, *33*, 15501–15510.
- (49) Müller, H. N.; Skerra, A. *Biochemistry* **1994**, *33*, 14126–14135.
- (50) Vita, C.; Roumestand, C.; Toma, F.; Ménez, A. *Proc. Natl. Acad. Sci. U.S.A.* **1995**, *92*, 6404–6408.
- (51) Stewart, J. D.; Roberts, V. A.; Crowder, M. W.; Getzoff, E. D.; Benkovic, S. J. *J. Am. Chem. Soc.* **1994**, *116*, 415–416.
- (52) Wade, W. S.; Koh, J. S.; Han, N.; Hoekstra, D. M.; Lerner, R. A. *J. Am. Chem. Soc.* **1993**, *115*, 4449–4456.
- (53) Handel, T. T.; Williams, S. A.; DeGrado, W. F. *Science* **1993**, *261*, 879–885.
- (54) Marangoni, A. G. *Enzyme Kinetics*; John Wiley & Sons, Inc.: Hoboken, NJ, USA, 2002; pp. 102–115.
- (55) Touw, D. S.; Nordman, C. E.; Stuckey, J. A.; Pecoraro, V. L. *Proc. Natl. Acad. Sci. U.S.A.* **2007**, *104*, 11969–11974.
- (56) The PyMOL Molecular Graphics System, Version 1.5.0.4 Schrödinger, LLC.